EFFECTS OF PRETREATMENT, HETEROPOLY ACID DOPING, HYDRATION, AND MEMBRANE CHEMISTRIES TO THE MORPHOLOGY AND TRANSPORT PROPERTIES OF PROTON EXCHANGE MEMBRANES

By

Yuan Liu

A thesis submitted to the Faculty and the Board of Trustees of the Colorado School of Mines in partial fulfillment of the requirements for the degree of Doctor of Philosophy (Chemical Engineering).

Golden, Colorado

Date _____

Signed _____

Yuan Liu

Signed _____

Dr. Andrew M. Herring

Thesis Advisor

Golden, Colorado

Date _____

Signed _____

Dr. David W.M. Marr

Professor and Head

Department of Chemical and Biological Engineering

ABSTRACT

In this thesis we studied the influence of annealing, heteropoy acid (HPA) doping, and side chain chemistry to a perfluorosulfonic acid polymer's (PFSA's) morphology and transport properties. We also investigated the effects of polymer block structure on a co-polyamide material's morphology and proton conduction properties.

We demonstrated that proton conductivity can be improved thorough annealing PFSA polymers at higher temperatures, due to the formation of larger ionic clusters: at 95%RH, the radius of gyration of the ionic domains increases from 11.9 Å to 17.1 Å, and the conductivity increases from 0.20 to 0.36 S/cm, as annealing temperature increases from 180 °C to 200 °C.

We also observed that Grotthuss hoping can be facilitated by HPA doping: the proton conductivity contributed from Grotthuss hopping increases from 0.10 to 0.15 S/cm for the undoped and 5%HPW doped films. HPAs make the hydrophilic domains more homogeneous by their bridging effect: the tortuosity at maximum humidity decreases from 1.40 to 1.08, upon 5%HPW addition.

To create larger ionic domains, bulky, highly flexible, and hydrophilic side chains, with less steric hindrance from protogenic groups are desirable: the 3M PFIA (contains multiple protogenic groups on the side chain), can form larger ionic domains than the 3M PFSA, which has a shorter side chain containing only one photogenic group; the meta bis ionomer forms larger ionic domains than the ortho bis ionomer, resulting from a larger separation distance between the sulfonic group and the imide group, hence less steric hindrance to water uptake.

Ordered ionic domains (with inter domain distance ca. 60 Å) were achieved by making a block copolymer. The block copolymer has lower conductivity and smaller water uptake than the

random polymer based on the same chemistry. The ionomer peak from the SAXS pattern of the block copolymer becomes less prominent upon hydration, indicating water reaches the polymer matrix.

ACKNOWLEDGEMENT

Foremost, I would like to express my special thanks to my advisor Prof. Andrew M. Herring for his enormous support while mentoring me as I completed my Ph.D. Without his guidance and encouragement, my research would not have been successful.

In addition to my advisor, I would like to thank my thesis committee members, Prof. Paul A. Martin, Prof. Daniel M. Knauss, Prof. Colin A. Wolden, and Prof. C. Mark Maupin for their valuable comments and suggestions pertaining to my research.

I also want to express my appreciation to various course instructors, the CBE and REMRSEC staff, and all my colleagues, for their help during my PhD study.

Finally, I would like to thank my family: my father Mr. Junfeng Liu, my mother Mrs. Lihua Yang, and my wife Ling Jin for their great support and love. I could not have overcome so many difficulties and reach this point in my life without their support.

TABLE OF CONTENTS

LIST OF FIGURES

LIST OF TABLES

LIST OF SCHEMATICS

CHAPTER 1 INTRODUCTION

1.1 An Overview of Fuel Cells

The Fuel cell is an energy conversion device, which has recently drawn a lot of attention.[1,2] Fuel cell converts the chemical energy of a fuel to electrical energy through electrochemical reactions without combustion. Fuel cells have much higher efficiencies than traditional heat engines in low temperature ranges, and are promising to meet the ever-growing energy demand of our society. Environmental pollution continues to be a major concern in people's lives. Fuel cells, which only produce water (or water and CO_2 when run on hydrocarbon fuels) at the point of use, therefore, have great environmental significance. The major types of fuel cells, named after their electrolyte, are: phosphoric acid fuel cell (PAFC), alkaline fuel cell (AFC), molten carbonate fuel cell (MCFC), solid oxide fuel cell (SOFC), and polymer electrolyte membrane fuel cell (PEMFC). Among them, the PEMFC has the highest power density, a relatively low operating temperature, and the best start-up and on-off cycling characteristics, making it most suitable for automotive and portable applications. Its ability to be easily refueled also makes it advantageous over conventional batteries for long distance transportation. The major types of fuel cells and their basic characteristics are summarized in Table 1.1 and Figure 1.1.

1.1.1 Proton Exchange Membrane Fuel Cells

The schematic of the PEM fuel cell is shown in Figure 1.2. Protons are conducted through a polymer electrolyte PEM. PEMFCs can operate at low temperature and are suitable for

Table 1.1 Basic characteristics of different types of fuel cells[3] (Summarized from ref. 3)

Fuel Cell Type	Anode Reaction	Cathode Reaction	Electrolyte	Advantage	Disadvantage	Application
SOFC	$H_2+O_2^- \rightarrow H_2O+2e^-$	$\frac{1}{2}O_2+2e^- \rightarrow O_2^-$	Ceramic	Fuel flexibility Nonprecious metal catalyst High-quality waste heat for cogeneration applications Solid electrolyte Relative high power density	Significant high-temperature materials issues Sealing issues Relatively expensive components/fabrication	Stationary energy sources Transportation Military uses
MCFC	$H_2+CO_3^{2-} \rightarrow CO_2+2H_2O+2e^-$	$\frac{1}{2}O_2+CO_2+2e^- \rightarrow CO_3^{2-}$	Molten Carbonate	Fuel flexibility Nonprecious metal catalyst High-quality waste heat for cogeneration applications	Must implement CO_2 recycling Corrosive, molten electrolyte Degradtion/lifetime issues Relative expensive materials	Stationary, continuous power applications
PAFC	$H_2 \rightarrow 2H^+ + 2e^-$	$\frac{1}{2}O_2+2H++2e- \rightarrow H2O$	Immobilized liquid H_3PO_4	Mature technology Excellent reliability/long-term performance Electrolyte is relatively low-cost	Expensive platinum catalyst Susceptible to CO and S poisoning Electrolyte is a corrosive liquid that must be replenished during operation	Transportation Military
PEMFC	H_2 as fuel: $H_2 \rightarrow 2H^+ + 2e^-$ Methanol as fuel (DMFC): $\frac{1}{3}CH_3OH+\frac{1}{3}H_2O \rightarrow \frac{1}{3}CO_2+2H^++2e^-$	$\frac{1}{2}O_2+2H^++2e^- \rightarrow H_2O$	Polymer	Highest power density Good start-stop capabilities Suitable for portable applications	Uses expensive platinum catalyst Polymer membrane and ancillary components are expensive Active water management is often required Very poor CO and S tolerance	Portable power Transportation
AFC	$2H_2+4OH^- \rightarrow 4H_2O+4e^-$	$O_2+2H_2O+4e^- \rightarrow 4OH^-$	KOH	Improved cathode performance Potential for nonprecious metal catalysts Low materials costs, extremely low-cost electrolyte	Must used pure H_2-O_2 KOH electrolyte may need occasional replenishment Must remove water from anode	Aerospace industry

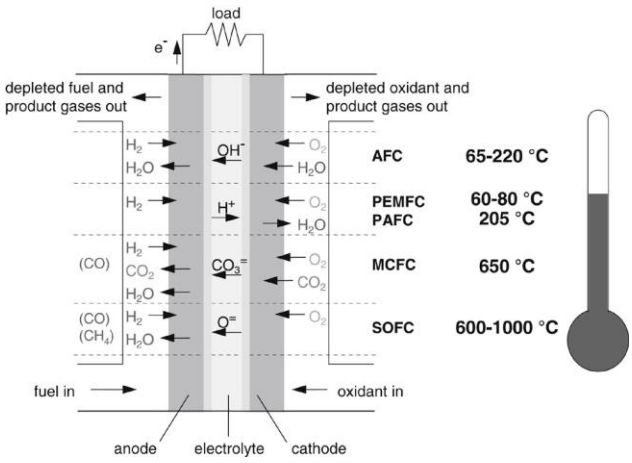

Figure 1.1 Types of fuel cells, their reactions, and operating temperatures.[4]

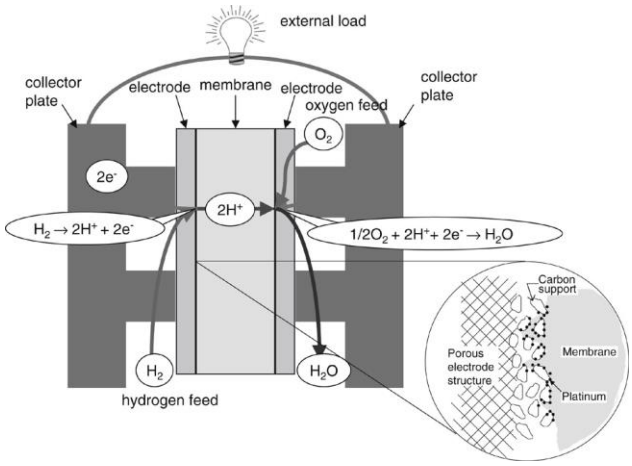

Figure 1.2 The basic principle of operation of a PEM fuel cell.[4]

automobile and portable applications. The electrochemical reactions of PEM fuel cell are shown below:

$$\text{Anode: } H_2 \rightarrow 2H^+ + 2e^-$$

$$\text{Cathode: } \frac{1}{2}O_2 + 2H^+ + 2e^- \rightarrow H_2O$$

$$\text{Overall: } H_2 + \frac{1}{2}O_2 = H_2O$$

1.2 Proton Transport

Protons are transported through the hydrophilic phase mainly via two mechanisms, the vehicle mechanism and the hopping or Grotthuss mechanism, and these mechanisms will have different contributions to the overall conduction of protons depending on temperature, pressure, counter-ion type, concentration and hydration level.[5] Under dry conditions, the transport is mostly due to the suppression of structural diffusion from the high concentration of excess protons. While under high hydrations, the hopping mechanism becomes the primary form of proton transport. The vehicle mechanism is proton transport achieved through "hitch a ride": water and proton forms hydroniums (H_3O^+ and $H_5O_2^+$, *etc*) and are transported via diffusion. [6,7] The hopping or Grotthuss mechanism is more complicated and involves steps of proton transfer (hopping), formation and breakage of hydrogen bonds, reorientation and reorganization of environment, *etc*. Protons are transferred through a hydrogen bonding network. [8,9] It is proposed that two forms of hydroniums are involved in this process: the $H_9O_4^+$ (Eigen cation) and $H_5O_2^+$ (Zundel cation), and their inter-conversion results in the displacement of the protonic defect (figure 1.3): The diffusion coefficients of water in perfluorosulfonic acid polymers (PFSAs) and other PEMs under different hydrations have been measured using PGSE-NMR.[10-16] Zawodzlnski *et al.* used the Nernst-Einstein equation to calculate the proton conductivity from the diffusion coefficient and compared the calculated values to the conductivity measured by electrochemical impedance spectroscopy (EIS). From these comparisons, the contributions of the Grotthuss mechanism and vehicle mechanism were differentiated.[16] For both proton transport mechanisms, water uptake is essential for the PEMs to achieve high proton conductivity.

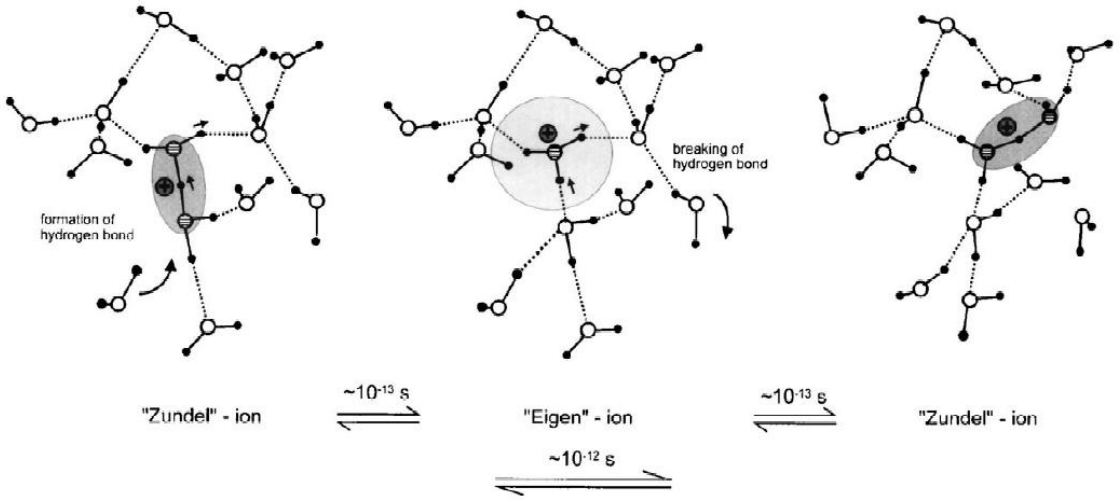

Figure 1.3 Transport mechanism of a protonic defect in water as obtained from an ab-initio MD simulation[17]

1.3 PEMs

The proton exchange membrane is the key constituent of a PEMFC, through which protons migrate from anode to cathode. It also serves as the separator for reactant gases and the insulator for electrons. The development of a highly proton conducting polymer electrolyte is essential for high performance of PEM fuel cells. Generally, PEMs should possess high proton conductivity, low electronic conductivity, low gas crossover, and high chemical and mechanical stability.[18] PEMs should be hydrophilic and achieve ideal levels of hydration upon humidification; and the material should maintain mechanical integrity, thermal and chemical stability under harsh operating conditions, and also be of low manufacturing and operating costs.

1.3.1 PFSA

Perflouro Sulfonic Acid (PFSA) membranes are one promising material, which has high proton conductivity, is thermally and chemically stable, and is capable of maintaining

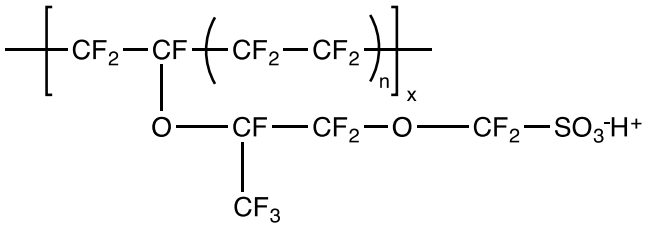

a

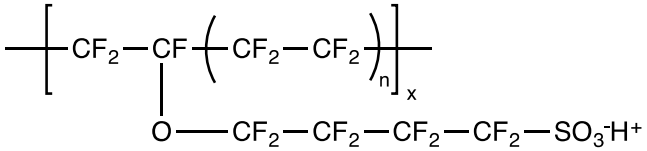

b

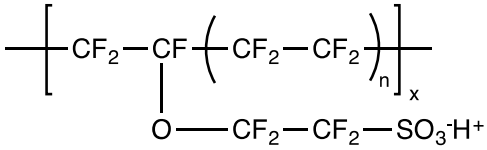

c

Scheme 1.1 Structure of Nafion™, 3M Ionomer(b) and Dow ionomer (c)

mechanical integrity under PEMFC operating conditions.[19,20] PFSAs contain a polytetrafluoroethylene (PTFE) backbone, which provides mechanical strength, and a perfluoro ether side chain, with a sulfonic acid terminal group attached at the end, which provides charge sites for proton transport. Several PFSA materials have been developed by different companies through the past decades, such as Nafion™ manufactured by Dupont, a short side chain (SSC) ionomer originally synthesized by Dow Chemical Company and now as Hyflon Ion™ manufactured by Solvay-Solexis and an intermediate side-chain material developed by the 3M company.[21,22] Their structures are shown in scheme 1.1. These ionomers all have the common structural feature of a PTFE backbone, with their perfluoro ether side chain varying in length and structure.

1.3.2 Hydrocarbon PEMs

Some stable aromatic hydrocarbon polymers can be sulfonated for use as PEM materials. Although these alternative membranes generally have lower ionic conductivity at lower temperature, and they are less stable chemically and mechanically, as compared to PFSAs, they have the following advantages: a) hydrocarbon polymers are less expensive than PFSAs, and can be made from commercially available materials; b) hydrocarbon polymers can be potentially operated at higher temperatures due to their high water uptake over wider temperature ranges; c) hydrocarbon polymers can be easily recycled hence they are environmentally friendly.[23] The most common backbone materials are polyether ketones (PEK) with varying number of ether and ketone functionalities (such as PEEK, PEKK, PEKEKK, etc.), Polyether sulfones (PESF), poly (arylene ethers), polyesters, and polyimides (PI), *etc*.[23] The sulfonation can either take place directly on the aromatic ring or on the side chain attached to the ring. Sulfonated polyaryletherketone (sPEEK) has been studied extensively.[24-28] Its structure is shown in scheme 1.2, and like a PFSA, it also contains sulfonic side groups serving as charge sites for proton transport. In order to improve the ionic conductivity and mechanical properties, block copolymers were studied, which show better phase separated morphology.[29,30]

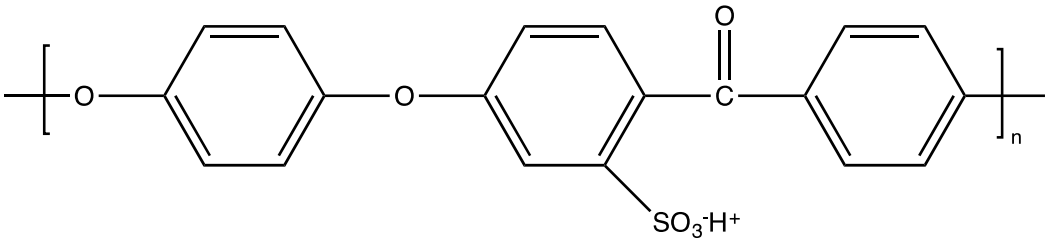

Scheme 1.2 General chemical structure of sulfonated PEEK.

1.3.3 Acid-Base Complexes

Acid-base complexes[23,31,32] are extremely suitable for high-temperature operations. Unlike PFSAs, their conductivity shows little dependence on humidity. Acid doped Polybenzimidazole (scheme 1.3), *e.g.* PBI/H_3PO_4, has been demonstrated successfully in higher temperature PEMFC applications (up to 200 °C). However, since the conductivity of acid-base complexes depends heavily on acid doping levels, challenges such as acid leaching still hinder this material's application. [33]

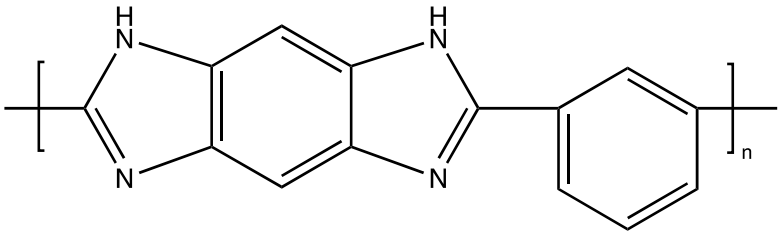

Scheme 1.3 General chemical structure of Polybenzimidazole (PBI).

1.3.4 Composite PEMs

It is beneficial to operate fuel cells at higher temperatures to simplify heat exchange systems and to prevent poisoning of the Pt catalyst from CO.[34,35] However, in hotter environments, the PEM's water retention capability becomes insufficient. The water loss results in a dramatic decrease of the ionic conductivity. One way to tackle this problem is through incorporation of inorganic components such as phosphates, heteropoly acids (HPAs), and inorganic oxides (SiO_2, TiO_2, ZrO_2, et al.) into polymer membranes to produce composite PEMs. [14,36-38] These inorganic components can interact with water and the ionomer trough hydrogen bonding and improve the water retention capability of the membrane hence enabling high proton

conductivity up to much higher temperatures (140 °C) than the traditional polymer membranes.[35,37] The mechanical and thermal stability can also be improved as a result. HPAs and zirconium phosphonates are among the most important additives, which show great improvement in proton conductivity.

Zirconium phosphonates nano-particles have been incorporated into ionomers such as Nafion™ to make nano-composite materials.[39,40] They can also be attached to the side chain or the backbone of the ionomer through vinyl and methyl methacrylate functionalities among others. Schlichting *et al.* studied the hybrid system of vinyl phosphonic acid (VPA) copolymerized with vinyl-functionalized zirconium phosphonate (VZP) and showed an improved chemical and mechanical stability as compared to VPA system. [41]

The HPAs are a subset of the larger polyoxometallate set of metal oxides. They are considered as super acids under the Bronsted definition. The HPA's structure has been studied extensive through Nuclear Magnetic Resonance (NMR), X-ray diffraction (XRD), and Infrared (IR) Spectroscopy techniques. [42-44] A wide variety of HPA structures are known, *e.g.* the Keggin structure $[X^{n+}M_{12}O_{40}]^{(8-n)-}$, the Dawson structure $[(X^{n+})_2M_{18}O_{62}]^{(16-2n)-}$ and the Anderson structure $[X^{n+}M_6O_{24}]^{(8-n)-}$. Among these, HPAs with the Keggin structure find their most important applications in catalysis and as doping components for proton exchange membranes. The Keggin structure (figure 1.4.) consists of a tetrahedral XO_4 with the central heteroatom X generally from the p-block of the periodic table (such as silicon and phosphorus). This tetrahedron is caged by 12 MO_6 oxometallate octahedral structures formed by oxygen and addenda atoms M, which are typically tungsten or molybdenum. A number of studies have been focused on the determination of HPA's protonation sites.[42,45] The edge bridging, corner bridging or terminal oxygen are potential protonation centers of HPAs. HPA can adopt a series of

hydrated states, depending on hydration conditions. In these states, HPAs such as 12-phosphotungstic acid (HPW) form a secondary structure[46] bridging the Keggin units, *e.g.,* by H^+ for dehydrated state and by Zundel $H_2O_5^+$ hydronium for HPW hexahydrate ($HPW \cdot 6H_2O$) (Figure 1.4). In such structures, the protonation centers are the terminal oxygen. When dissolved in aqueous solution, HPAs such as HPW are believed to be completely deprotonated. HPAs have very high conductivity in the solid state (up to 0.18 S cm^{-1}at room temperature for 12-phosphotungstic acid).[47] Protons are thought to transport through space between the heteropolyanions (HPANs). The geometry of the HPA clusters influences the transport phenomena of protons through HPA systems.[43] With their extremely high intrinsic proton conductivity and strong acidity, HPAs become an ideal choice for additives to enhance proton-conducting characteristics of PEMs.[43] HPAs with Keggin structures have been frequently incorporated into ionomers, and show great improvement in ionic conductivity and water retention capabilities of the resultant composite material.

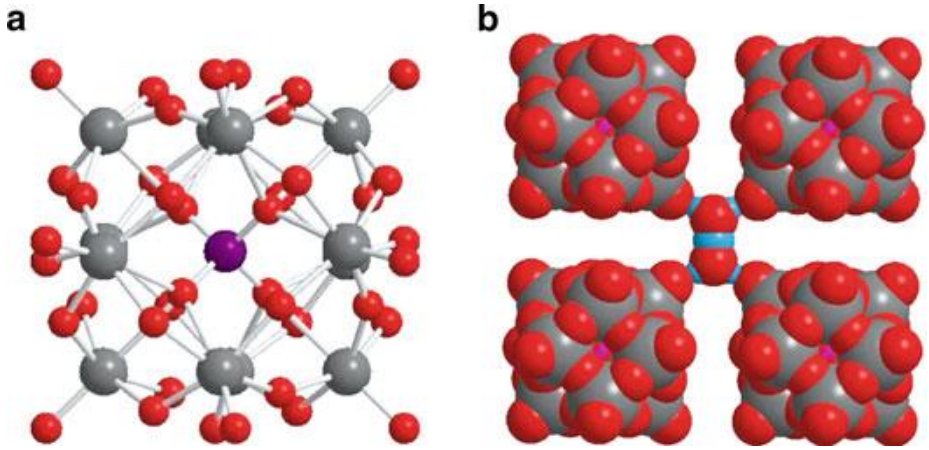

Figure 1.4 Heteropoly acid structures (a) Ball and stick model of the silicotungstic Keggin anion ($SiW_{12}O_{40}^{-4}$). (b) Space filling model of the secondary crystalline structure of Keggin HPA with base-centered cubic arranged cavities containing $H_5O_2^+$ cations (red 1⁄4 O, gray 1⁄4 W, blue 1⁄4 H, purple 1⁄4 P or Si) [46]

1.4 Morphology of PEM

Due to the hydrophobicity of the PTFE backbone, and the hydrophilic nature of the sulfonic acid group, PFSAs are generally believed to form a hydrophobic/hydrophilic phase separated morphology. However, a thorough understanding of the PFSA's morphology under different hydration conditions and with different pretreatments is needed to aid in designing new proton conductive materials with better performance. To date, there is no agreement on the detailed morphology of a PFSA. Microscopy studies using SEM and AFM have obtained some information about phase separation, particle shape, particle size, and separation distance.[48,49] These characterization methods have limitations in that they are only capable of obtaining surface or local structures, and often have difficulty in environmental control. SAXS, on the other hand, can obtain *in-situ* dynamic bulk averaged morphology with very easy control of temperature, humidity and other experimental conditions. Therefore, small angle X-ray scattering has great significance in the morphological study of PEMs, and has became the most important characterization technique in this field. Nevertheless, unlike other instruments, SAXS is an indirect technique. Because of the loss of phase information, it is very difficult to obtain the 3D holographic morphological representation without assumptions. Due to these limitations, the interpretation of scattering data requires adopting some morphological models.

For PFSAs, we generally observe an ionomer peak in the high q region, a matrix knee in the low q region, and an upturn in the ultra low q region,[50] as shown in figure 1.5. The so-called ionomer peak is believed to arise from the scattering of the hydrophilic ionic domain; it is found to increase in intensity and shift to lower q upon hydration. The matrix knee is absent in the quenched samples, and has higher intensity for larger EW samples; therefore it is attributed to interference between nano-crystalline structures within the fluorocarbon matrix. The ultra small

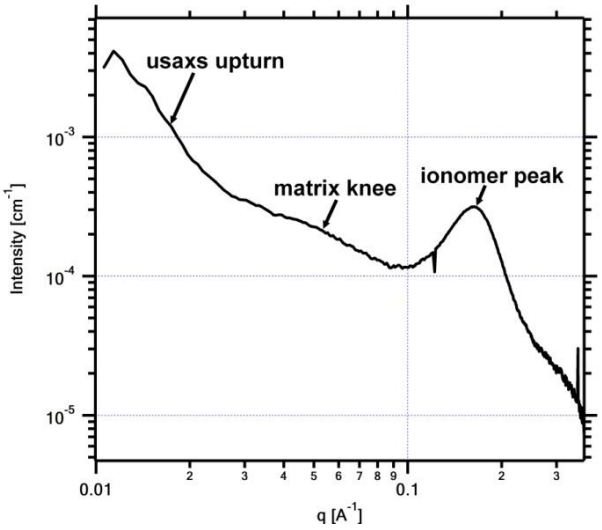

Figure 1.5 SAXS pattern of one of 3M PFSA films. Three structural levels are shown on the experimental SAXS pattern of PFSA as an ionomer peak on the high q region and a crystalline matrix knee on the low q region, and an ultra-small angle upturn in the ultra law q region.[50]

angle upturn is associated with the morphological features of long-range inhomogeneity from the ionic clusters distribution.[20]

Contrast variation experiments have been performed and reported in various studies and valuable structural information has been obtained for different PEMs.[28,51,52] For neutrons, isotopic replacement is generally performed (e.g. hydrogen for deuterium), and for X-ray studies, ion exchange with different counterions (e.g. Na^+, K^+, and Cs^+, etc.) is usually carried out. The scattering length density of one phase is varied through the contrast variation technique and the change of scattering spectra can yield additional morphological information to test the validity of morphological models.[53]

Fourier transformation of SAXS spectra is an appealing way to obtain direct representation of morphology in real space. However this technique is severely hindered by the insufficient angular range of SAXS data and the averaging effect introduced during the SAXS

data collection. Nevertheless, Elliot *et al.* and Aieta *et al.* managed to obtain a 2D visualization of the ionic structures and compared with the AFM images.[53,54,55]

A deformation study is another important way to probe the shape and arrangement of PEMs' morphological features. The behavior of SAXS profiles upon stretch also has implication to the validity of morphological models. SAXS measurements of stretched Nafion™ done by Gierke et al.[56] and Fujimura et al.[57] show the periodicity and orientation of crystalline/ionomer domains. Moore et al.[58] performed the deformation study of Nafion™ exchanged with different counterions, and found the anisotropy of SAXS patterns disappeared upon heating at temperatures corresponding to the α-relaxations of these materials.

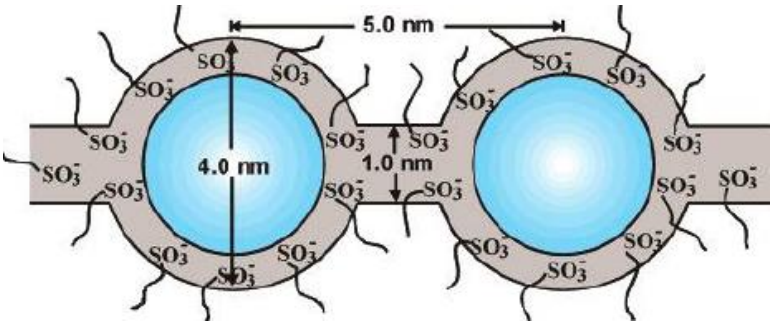

Figure 1.6 Cluster-network model for the morphology of hydrated Nafion.[20,60]

Based on the small angle scattering studies, a large number of structural models have been proposed. The cluster-network model proposed by Gierke *et al.*[59] is the most influential model, and served as a foundation for further morphological studies. In this model, inverted micelle clusters interconnected by 1 nm channels were proposed (figure 1.6). However, this model does not mean to precisely describe the morphology of PFSA films. There is no experimental proof of the existence of 1 nm channels and the spatial distribution of inverted

cluster micelle either. Further, Fujimura *et al.* proposed a core-shell model:[61] an ion rich core surrounded by an ion depleted shell formed by Teflon™ like backbones. These core-shell structures are distributed in a matrix formed by fluorocarbon chains. Unlike most structural models such as the cluster network model and the hard-sphere model (figure 1.7a), which attribute the ionomer peak to the interparticle scattering, the core-shell model (figure 1.7b) attributes the high q maxima in the SAXS pattern to the intraparticle scattering from the scatterer density inhomogeneity inside the core-shell particle, i.e. the existence of an ion rich core surrounded by a ion depleted shell.

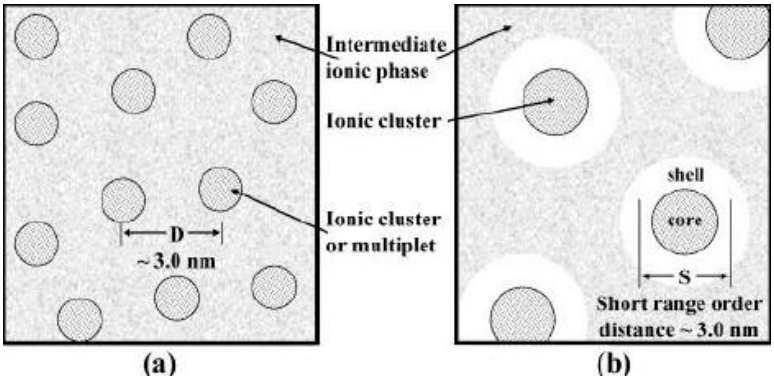

Figure 1.7 Two morphological models used to describe the origin of the ionic SAXS maximum observed for Nafion: (a) the modified hard-sphere model depicting interparticle scattering and (b) the depleted-zone core-shell model depicting intraparticle scattering.[20,61]

Dreyfus and co-workers proposed a local order model[62] using a tetrahedral as the radial distribution function and a sphere as the form factor, and find excellent agreement with the experimental SAXS data. A lamella model was proposed by Litt[63] based on the observation that D-spacing of ionomer peak varies linearly with water content. However, no parallel shift of two maxima is found, which renders this model an oversimplification of morphology of PFSA films. The lamella model also assumes no combination of clusters taking place, which again is found to

be an unlikely situation, as shown by the inverted Fourier transform of experimental SAXS curves.[54] A modified lamellar model (sandwich model) was later proposed by Haubold et al.,[64] generating an ionomer peak in good agreement with other investigations. Further, Rubatat et al. observed a q^{-4} power law region and a q^{-1} power law region in the SAXS patterns. While the q^{-4} power law decay indicates a sharp interface for the scatterers, the q^{-1} is indicative of a rod-like structure with a length of L and diameter of D, where the scattering vector at the start and the end of the q^{-1} power law region q_1 and q_2 equal to 2pi/L and 2pi/D respectively.[51] Gebel et al.[65] suggest a changing morphology of PFSA at different hydration states: the system will undergo a structure inverting at Φ_s=0.5, from a solvent in polymer to a polymer in solvent system. And the shape of the scattering object will also change according to different hydration levels (figure 1.8).

We already know that the morphology of PFSA films is very controversial. It is believed to depend heavily on chemical structures, presence of additives, thermal history, pretreatment conditions, and hydration. However, morphology to a large extent will determine the performance of PEMs, such as proton conductivity and water transport properties, etc. SAXS measurement remains the most important characterization technique to obtain meaningful morphological information on PEMs. Continuing study of the morphology of PEMs using SAXS, therefore, is essential for fundamentally understanding the transport properties and performance of PEMs. The difficulty associated with SAXS measurements is that SAXS is an indirect technique, which requires effort in using scattering theory to interpret experimental data. Using appropriate scattering theory and morphological models to fit experimental curves will still be the most important way to investigate morphology of PEMs. In this project, we adopted SAXS as a main technique in the morphology study of PEMs with various pretreatment,

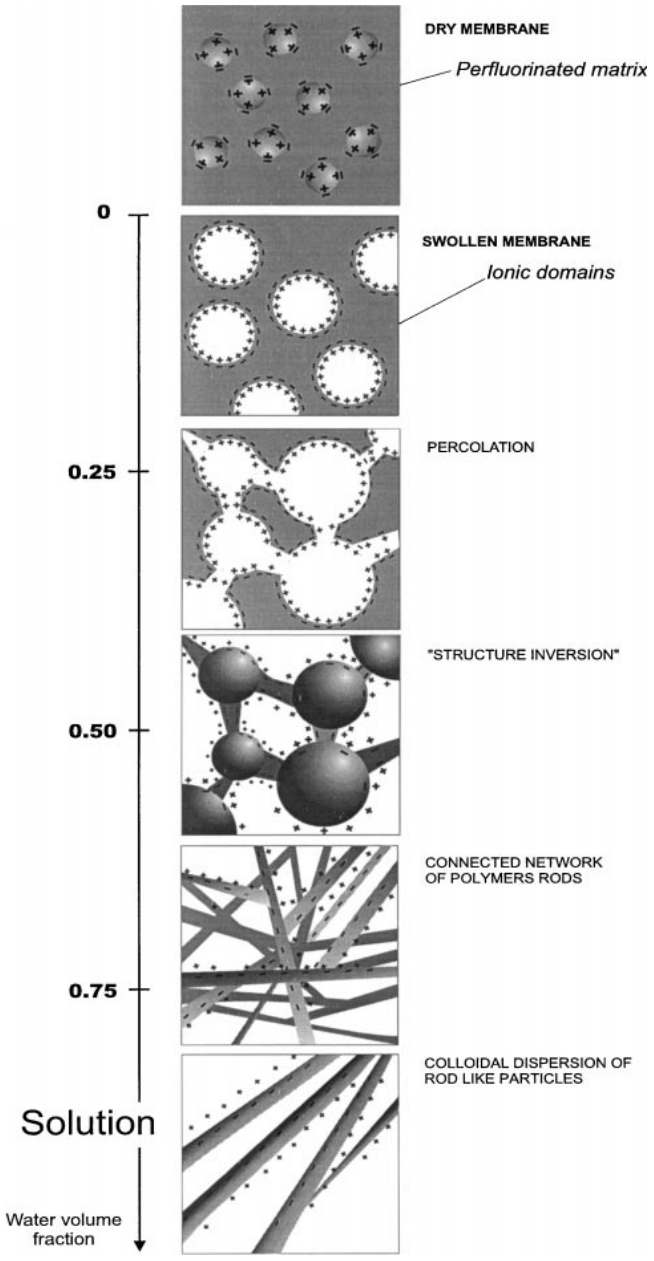

Figure 1.8 Conceptual model for the morphological reorganization and continuity of the ionic domains in Nafion™ as the dry membrane is swollen with water to the state of complete dissolution. [65]

chemistry, and inorganic additives, in an effort to reveal the morphological behavior, and their implication to membrane properties.

1.5 Thesis Statement

In this thesis, annealing conditions, heteropoly acid (HPA) doping level, and the modification of side chain chemistries are varied to investigate the resulting effect on the morphology and transport properties of the 3M PFSA ionomer. In addition to the 3M ionomer, the morphology and proton conduction of newly developed random and block co-polyamide PEMs were also studied. By addressing the following aspects in the present study, we see how the knowledge gained by this investigation leads directly to a better scientific understanding of how PEM design can improve fuel cell performance.

1.5.1 Improve PFSA Performance Through Annealing

When heated above the glass transition temperature (T_g), the polymer chains of perfluro-sulfonic acids (PFSAs) will become mobilized. The resulting reorganization of the microstructures of the polymer under these conditions is known to affect proton conductivity.[66-68] The morphology of PFSA and its influence on proton conduction has been a subject of considerable debate. Some studies show that narrow and well-connected ionic channels are favorable for proton transport, [69] while other studies postulate that wider channels will be less tortuous, and hence lead to faster proton conduction. [70-72] We hypothesize that a wider proton conductive channel can be created through annealing because the affinity of ionic domains, through a process of electrostatic attraction of ion pairs, will drive these domains to form larger clusters during reorganization. Upon cooling and hydration, a higher degree of phase separation

can be achieved. We also hypothesize that higher annealing temperatures can facilitate this process by enabling more previously restricted structures to reorganize. This allows the system to obtain even larger proton conducting channels, which will result in enhanced conductivity characteristics. It is our expectation that a change in the domain's geometry will also occur from annealing, and this will also affect proton conductivity.

In order to test the hypothesis that annealing at higher temperature will form larger ionic domains and improve conductivity, we will use *in-situ* small angle X-ray scattering (SAXS) measurements to reveal the dynamic morphological evolution of the 3M PFSA's ionic domains during the heating, cooling and hydration processes, due to its easy environmental control and ability to probe the bulk structure. Electrochemical impedance spectroscopy (EIS) will be used to measure the conductivity. The sizes of ionic domains for the films annealed at various temperatures will be obtained by SAXS measurements. A unified fit model, which is especially suitable for material with multiple structure levels, [73] will be used to obtain size information of the ionic domains, and a power law fit[74] will be adopted to investigate the geometry of the polymer domains. The 3M PFSA was chosen for our study material. The 3M PFSA has a shorter side chain than Nafion™ resulting in better mechanical strength and higher conductivity when compared to Nafion™ with same equivalent weight (EW). [19,75,76] We will select 180, 190, and 200 °C as the annealing temperatures based on the T_g of 3M ionomer (125 °C), which is 25 °C higher than Nafion™. Excessive high temperature (beyond 200 °C) will result in deterioration of the integrity of ionic clusters and desulfonation. [77-80] Industrially, these temperatures are also selected for heat treatment of 3M PFSA to enhance PEM performance, although the fundamental causes are not clear for these improvements.[81] This study is shown in Chapter 2.

1.5.2 Improve PEM Performance Through HPA Addition

Another method for improving PEM properties is to add acidic inorganic additives. The HPAs are one of the most attractive additives to improve PEM performance due to their super acidity, very high intrinsic conductivity, and water retention capabilities.[46,82] We postulate that HPA addition to a PFSA proton exchange membrane (PEM) can increase the homogeneity of the ionic domains, due to hydration shells formed around the HPA that include both water and hydronium ions. This modified solvent environment is hypothesized to increase the number and stability of bridging waters between isolated ionic domains in the PFSA.[36,83] The resulting homogeneous hydrophilic domain can ultimately promote the mobility of water and hydronium ions. It is also postulated that the use of the Grotthuss hopping mechanism will be enhanced due to the creation of a more interconnected hydrogen bonding network in the presence of HPA addition. Conversely, an increase in proton transport due to the Grotthuss mechanism will be accompanied by a reduction in the mobility of water via the vehicle mechanism of proton transport as a result of the strong hydration energy of the HPA nano-particles. Due to these duel effects, we expect a non-monotonic behavior of water diffusion upon HPA doping, while the overall conductivity, which is a combination of proton conduction through Grotthuss hopping and vehicle mechanism, will also be affected. We hypothesize that these transport properties will depend heavily on the loading levels of HPA.

To test this hypothesis, we will use pulsed gradient-spin echo nuclear magnetic resonance (PGSE-NMR) spectroscopy to probe the geometry of the ionic domain, through a fitting of the measured time dependent water diffusion coefficients to the Mitra equation.[84] PGSE-NMR and EIS will also be used to measure diffusion coefficients and conductivity, respectively, for films with various HPA loadings. We will then compare the measured conductivity from EIS with the

calculated conductivity through the use of the Nernst-Einstein equation utilizing the diffusion coefficients obtained by PGSE-NMR. The measured conductivity from EIS will include the contribution of protonic conduction from both vehicular and the Grotthuss mechanisms, while the calculated diffusion coefficients will only take into account the vehicle mechanism. Therefore, the difference between these two measurements will give us the contribution of proton transfer through the Grotthuss hopping mechanism. Phosphotungstic acid (HPW) is chosen in this study because of its high acidity and good stability compared to other HPAs with the Keggin structure. To study the effects of HPA concentration, HPA loadings of 1% and 5% were investigated, due to the fact that conductivity improvement is most effective in this range of HPW addition. Higher HPA loadings will lead to aggregation, resulting in minimal improvement to conductivity.[83] Such aggregation will also hinder our understanding of HPA nano-crystal's interaction with water, hydronium ions, and the ionomer. This study is shown in Chapter 3.

1.5.3 Improve PEM Performance Through Modifying the Side Chain Chemistry

PEM performance can also be improved through side chain modification. 3M developed a modified PFSA material-- the Per Fluoro Imide Acid Ionomer (PFIA), with multiple protogenic groups, i.e., a very acidic imide group in addition to the sulfonic group, on the side chain. Such structure is capable of achieving high IEC and conductivity, while at the same time maintaining sufficient degree of crystallinity, and hence the mechanical strength.[85] To further optimize the side chain structure, 3M also developed ionomers with different separation distance between protogenic groups, i.e., the ortho bis and the meta bis ionomer. We hypothesize that a flexible and hydrophilic side chain (*e.g.*, with multiple protogenic sites) will lead to the formation of larger ionic domains. We also hypothesize that a larger separation distance between protogenic

groups will avoid the steric hindrance observed during water uptake, resulting in the formation of larger ionic domains as well.

The formed domain sizes of 3M PFIA and 3M PFSA will be measured through SAXS to test the hypothesis that a flexible and hydrophilic side chain will facilitate the formation of larger ionic domains, and to confirm the presence of nano-crystal structures in PFIA. To investigate the hydrophilicity difference between side chains with single (3M PFSA) and multiple (3M PFIA) protogenic groups, we will measure the water uptake in these ionomers through dynamic vapor sorption (DVS). The hypothesis pertaining to steric effects will be tested through the SAXS investigation of the formed ionic domain sizes of the ortho bis and the meta bis ionomers. This study is shown in chapter 4.

1.5.4 Improve PEM Performance Through Modifying the Backbone Structure

It is easier to control the morphology of a hydrocarbon material, *e.g.*, the geometry of ionic conductive channels, than that of a PFSA. A well defined phase separated morphology can be achieved by synthesizing block copolymers.[30,86,87] We hypothesize that block copolymers will have higher dimensional stability than the random copolymers, due to their ordered ionic conductive channels that have a defined geometry. We also hypothesize that both random and block copolymers will have higher conductivity than PFSA at higher temperatures (≥80 °C), due to their better water retention capability resulting from the polar groups on the backbone.

To test this hypothesis, we will investigate a random and block copolyamide ionomer, and measure their stability in water at various temperatures. We will also measure their conductivity using EIS and the structure of the ionic channels under different hydration levels using SAXS. This study is shown in chapter 5.

1.6 References

(1) Mehta, V.; Cooper, J. S. *Journal of Power Sources* **2003**, *114*, 32.

(2) Larminie, J.; Dicks, A.; McDonald, M. S. *Fuel cell systems explained*; Wiley New York, 2003; Vol. 2.

(3) O'Hayre, R. P.; Cha, S.-W.; Colella, W.; Prinz, F. B. **2006**.

(4) Barbir, F. *PEM fuel cells: theory and practice*; Academic Press, 2013.

(5) Kreuer, K. D.; Paddison, S. J.; Spohr, E.; Schuster, M. *Chemical Reviews* **2004**, *104*, 4637.

(6) Kreuer, K. D.; Rabenau, A.; Weppner, W. *Angewandte Chemie-International Edition in English* **1982**, *21*, 208.

(7) Kreuer, K. D. *Chemistry of Materials* **1996**, *8*, 610.

(8) Glasstone, S.; Laidler, K. J.; Eyring, H.; McGraw-Hill: New York, **1941**, p 550

(9) Sagnella, D. E.; Laasonen, K.; Klein, M. L. *Biophys J* **1996**, *71*, 1172.

(10) Tsushima, S.; Teranishi, K.; Hirai, S. *Energy* **2005**, *30*, 235.

(11) Ochi, S.; Kamishima, O.; Mizusaki, J.; Kawamura, J. *Solid State Ionics* **2009**, *180*, 580.

(12) Hou, J. B.; Li, J.; Mountz, D.; Hull, M.; Madsen, L. A. *Journal of Membrane Science* **2013**, *448*, 292.

(13) Freger, V.; Korin, E.; Wisniak, J.; Korngold, E.; Ise, M.; Kreuer, K. D. *Journal of Membrane Science* **1999**, *160*, 213.

(14) Meng, F. Q.; Aieta, N. V.; Dec, S. F.; Horan, J. L.; Williamson, D.; Frey, M. H.; Pham, P.; Turner, J. A.; Yandrasits, M. A.; Hamrock, S. J.; Herring, A. M. *Electrochim Acta* **2007**, *53*, 1372.

(15) Roy, A.; Hickner, M. A.; Yu, X.; Li, Y. X.; Glass, T. E.; McGrath, J. E. *Journal of Polymer Science Part B-Polymer Physics* **2006**, *44*, 2226.

(16) Zawodzinski, T. A.; Springer, T. E.; Uribe, F.; Gottesfeld, S. *Solid State Ionics* **1993**, *60*, 199.

(17) Kreuer, K. D. *Solid State Ionics* **2000**, *136*, 149.

(18) Hickner, M. A.; Ghassemi, H.; Kim, Y. S.; Einsla, B. R.; McGrath, J. E. *Chemical Reviews* **2004**, *104*, 4587.

(19) Hamrock, S. J.; Yandrasits, M. A. *Polymer Reviews* **2006**, *46*, 219.

(20) Mauritz, K. A.; Moore, R. B. *Chemical Reviews* **2004**, *104*, 4535.

(21) Whiteley, L. D.; Martin, C. R. *Journal of Physical Chemistry* **1989**, *93*, 4650.

(22) Haugen, G. M.; Meng, F. Q.; Aieta, N. V.; Horan, J. L.; Kuo, M. C.; Frey, M. H.; Hamrock, S. J.; Herring, A. M. *Electrochemical and Solid State Letters* **2007**, *10*, B51.

(23) Rikukawa, M.; Sanui, K. *Prog Polym Sci* **2000**, *25*, 1463.

(24) Xing, P. X.; Robertson, G. P.; Guiver, M. D.; Mikhailenko, S. D.; Wang, K. P.; Kaliaguine, S. *Journal of Membrane Science* **2004**, *229*, 95.

(25) Robertson, G. P.; Mikhailenko, S. D.; Wang, K. P.; Xing, P. X.; Guiver, M. D.; Kaliaguine, S. *Journal of Membrane Science* **2003**, *219*, 113.

(26) Kaliaguine, S.; Mikhailenko, S. D.; Wang, K. P.; Xing, P.; Robertson, G.; Guiver, M. *Catal Today* **2003**, *82*, 213.

(27) Yang, B.; Manthiram, A. *Journal of Power Sources* **2006**, *153*, 29.

(28) Gebel, G. *Macromolecules* **2013**, *46*, 6057.

(29) Roy, A.; Hickner, M. A.; Yu, X.; Li, Y.; Glass, T. E.; McGrath, J. E. *Journal of Polymer Science Part B: Polymer Physics* **2006**, *44*, 2226.

(30) Elabd, Y. A.; Hickner, M. A. *Macromolecules* **2011**, *44*, 1.

(31) Tanaka, R.; Yammoto, H.; Kawamura, S.; Iwase, T. *Electrochim Acta* **1995**, *40*, 2421.

(32) Glipa, X.; Bonnet, B.; Mula, B.; Jones, D. J.; Roziere, J. *J Mater Chem* **1999**, *9*, 3045.

(33) Thampan, T. M.; Jalani, N. H.; Choi, P.; Datta, R. *Journal of the Electrochemical Society* **2005**, *152*, A316.

(34) Zhang, J. L.; Xie, Z.; Zhang, J. J.; Tanga, Y. H.; Song, C. J.; Navessin, T.; Shi, Z. Q.; Song, D. T.; Wang, H. J.; Wilkinson, D. P.; Liu, Z. S.; Holdcroft, S. *Journal of Power Sources* **2006**, *160*, 872.

(35) Yang, C.; Costamagna, P.; Srinivasan, S.; Benziger, J.; Bocarsly, A. B. *Journal of Power Sources* **2001**, *103*, 1.

(36) Ramani, V.; Kunz, H. R.; Fenton, J. M. *Journal of Membrane Science* **2004**, *232*, 31.

(37) Kim, Y. S.; Wang, F.; Hickner, M.; Zawodzinski, T. A.; McGrath, J. E. *J Membrane Sci* **2003**, *212*, 263.

(38) Vernon, D. R.; Meng, F. Q.; Dec, S. F.; Williamson, D. L.; Turner, J. A.; Herring, A. M. *Journal of Power Sources* **2005**, *139*, 141.

(39) Costamagna, P.; Yang, C.; Bocarsly, A. B.; Srinivasan, S. *Electrochim Acta* **2002**, *47*, 1023.

(40) Alberti, G.; Casciola, M.; Capitani, D.; Donnadio, A.; Narducci, R.; Pica, M.; Sganappa, M. *Electrochim Acta* **2007**, *52*, 8125.

(41) Schlichting, G. J.; Horan, J. L.; Jessop, J. D.; Nelson, S. E.; Seifert, S.; Yang, Y.; Herring, A. M. *Macromolecules* **2012**, *45*, 3874.

(42) Kozhevnikov, I. V.; Sinnema, A.; Vanbekkum, H. *Catal Lett* **1995**, *34*, 213.

(43) Chikin, A. I.; Chernyak, A. V.; Jin, Z.; Naumova, Y. S.; Ukshe, A. E.; Smirnova, N. V.; Volkov, V. I.; Dobrovolsky, Y. A. *J Solid State Electr* **2012**, *16*, 2767.

(44) Malers, J. L.; Sweikart, M. A.; Horan, J. L.; Turner, J. A.; Herring, A. M. *Journal of Power Sources* **2007**, *172*, 83.

(45) Ganapathy, S.; Fournier, M.; Paul, J. F.; Delevoye, L.; Guelton, M.; Amoureux, J. P. *J Am Chem Soc* **2002**, *124*, 7821.

(46) Sachdeva, S.; Turner, J. A.; Horan, J. L.; Herring, A. M. *Struct Bond* **2011**, *141*, 115.

(47) Nakamura, O.; Kodama, T.; Ogino, I.; Miyake, Y. *Chem Lett* **1979**, 17.

(48) Zawodzinski, T. A.; Gottesfeld, S.; Shoichet, S.; Mccarthy, T. J. *J Appl Electrochem* **1993**, *23*, 86.

(49) Fujimura, M.; Hashimoto, T.; Kawai, H. *Macromolecules* **1982**, *15*, 136.

(50) Liu, Y.; Horan, J. L.; Schlichting, G. J.; Caire, B. R.; Liberatore, M. W.; Hamrock, S. J.; Haugen, G. M.; Yandrasits, M. A.; Seifert, S.; Herring, A. M. *Macromolecules* **2012**, *45*, 7495.

(51) Rubatat, L.; Rollet, A. L.; Gebel, G.; Diat, O. *Macromolecules* **2002**, *35*, 4050.

(52) Rollet, A. L.; Diat, O.; Gebel, G. *Journal of Physical Chemistry B* **2002**, *106*, 3033.

(53) Gebel, G.; Diat, O. *Fuel Cells* **2005**, *5*, 261.

(54) Elliott, J. A.; Hanna, S.; Elliott, A. M. S.; Cooley, G. E. *Macromolecules* **2000**, *33*, 4161.

(55) Aieta, N. V.; Stanis, R. J.; Horan, J. L.; Yandrasits, M. A.; Cookson, D. J.; Ingham, B.; Toney, M. F.; Hamrock, S. J.; Herring, A. M. *Macromolecules* **2009**, *42*, 5774.

(56) Gierke, T. D.; Munn, G. E.; Wilson, F. C. *Journal of Polymer Science Part B-Polymer Physics* **1981**, *19*, 1687.

(57) Fujimura, M.; Hashimoto, T.; Kawai, H. *Macromolecules* **1981**, *14*, 1309.

(58) Page, K. A.; Landis, F. A.; Phillips, A. K.; Moore, R. B. *Macromolecules* **2006**, *39*, 3939.

(59) Gierke, T.; Hsu, W. 1982.

(60) Hsu, W. Y.; Gierke, T. D. *Journal of Membrane Science* **1983**, *13*, 307.

(61) Fujimura, M.; Hashimoto, T.; Kawai, H. *Macromolecules* **1981**, *14*, 1309.

(62) Dreyfus, B.; Gebel, G.; Aldebert, P.; Pineri, M.; Escoubes, M.; Thomas, M. *J Phys-Paris* **1990**, *51*, 1341.

(63) Litt, M. *BM Culbertson, Ed* **1997**, *38*, 80.

(64) Haubold, H. G.; Vad, T.; Jungbluth, H.; Hiller, P. *Electrochim Acta* **2001**, *46*, 1559.

(65) Gebel, G. *Polymer* **2000**, *41*, 5829.

(66) Hensley, J. E.; Way, J. D.; Dec, S. F.; Abney, K. D. *Journal of Membrane Science* **2007**, *298*, 190.

(67) Page, K. A.; Cable, K. M.; Moore, R. B. *Macromolecules* **2005**, *38*, 6472.

(68) DeLuca, N. W.; Elabd, Y. A. *Journal of Membrane Science* **2006**, *282*, 217.

(69) Fang, C. L.; Toh, X. N.; Yao, Q. F.; Julius, D.; Hong, L.; Lee, J. Y. *Journal of Power Sources* **2013**, *226*, 289.

(70) Kreuer, K. D. *Journal of Membrane Science* **2001**, *185*, 29.

(71) Peckham, T. J.; Schmeisser, J.; Rodgers, M.; Holdcroft, S. *J Mater Chem* **2007**, *17*, 3255.

(72) Peckham, T. J.; Holdcroft, S. *Adv Mater* **2010**, *22*, 4667.

(73) Beaucage, G. *Journal of Applied Crystallography* **1995**, *28*, 717.

(74) Glatter, O.; Kratky, O. *Small Angle X-ray Scattering*; Academic Press, 1982.

(75) Clark, J. K.; Paddison, S. J.; Hamrock, S. J. *Phys Chem Chem Phys* **2012**, *14*, 16349.

(76) Emery, M.; Frey, M.; Guerra, M.; Haugen, G.; Hintzer, K.; Lochhaas, K. H.; Pham, P.; Pierpont, D.; Schaberg, M.; Thaler, A. *ECS Transactions* **2007**, *11*, 3.

(77) Iijima, M.; Sasaki, Y.; Osada, T.; Miyamoto, K.; Nagai, M. *Int J Thermophys* **2006**, *27*, 1792.

(78) Mosa, J.; Duran, A.; Aparicio, M. *Journal of Membrane Science* **2010**, *361*, 135.

(79) Shin, S. J.; Balabanovich, A. I.; Kim, H.; Jeong, J.; Song, J.; Kim, H. T. *Journal of Power Sources* **2009**, *191*, 312.

(80) Swier, S.; Ramani, V.; Fenton, J. M.; Kunz, H. R.; Shaw, M. T.; Weiss, R. A. *Journal of Membrane Science* **2005**, *256*, 122.

(81) Frey, M. H.; Hamrock, S. J.; Haugen, G. M.; Lamanna, W. M.; Larson, J. M.; Pham, P. T.; Google Patents: 2009.

(82) Herring, A. M. *Polymer Reviews* **2006**, *46*, 245.

(83) Ramani, V.; Kunz, H. R.; Fenton, J. M. *Journal of Membrane Science* **2005**, *266*, 110.

(84) Mitra, P. P.; Sen, P. N.; Schwartz, L. M.; Ledoussal, P. *Phys Rev Lett* **1992**, *68*, 3555.

(85) Schaberg, M. S.; Abulu, J. E.; Haugen, G. M.; Emery, M. A.; O'Conner, S. J.; Xiong, P. N.; Hamrock, S. J. *Polymer Electrolyte Fuel Cells 10, Pts 1 and 2* **2010**, *33*, 627.

(86) Lee, M.; Park, J. K.; Lee, H. S.; Lane, O.; Moore, R. B.; McGrath, J. E.; Baird, D. G. *Polymer* **2009**, *50*, 6129.

(87) Park, C. H.; Lee, C. H.; Guiver, M. D.; Lee, Y. M. *Prog Polym Sci* **2011**, *36*, 1443.

CHAPTER 2 A SMALL-ANGLE X-RAY SCATTERING STUDY OF THE DEVELOPMENT OF MORPHOLOGY IN FILMS FORMED FROM THE 3M PERFLUORINATED SULFONIC ACID IONOMER

Reproduced from *Macromolecules* 2012, 45, 7495-7503. Copyright ACS 2012.

Yuan Liu,† James L. Horan,† Gregory J. Schlichting,† Benjamin R. Caire,† Matthew W. Liberatore,† Steven J. Hamrock,‡ Gregory M. Haugen,‡ Michael A. Yandrasits,‡ Sönke Seifert,§ and Andrew M. Herring*,†

2.1 Abstract

An extensive SAXS investigation of the 3M perfluorinated sulfonic acid ionomer was performed to investigate the morphological changes that occur during and after annealing at temperatures above the T_α. The effect of film thickness in the range studied, 11−45 μm, was found to be negligible. These properties were studied as a function of equivalent weight from 700 to 1100 and correlated with the water uptake as measured by dynamic vapor sorption. Isoscattering points were observed in dynamic annealing experiments of the unboiled annealed films at q = 0.023, 0.096 $Å^{-1}$. On initial water uptake these films also showed isoscattering points at q = 0.024, 0.220 $Å^{-1}$; q = 0.029, 0.223 $Å^{-1}$; and q = 0.030, 0.211 $Å^{-1}$ at 50, 80, or 95 °C, respectively, indicating a decrease in the symmetry of the scattering objects in these size

†Department of Chemical and Biological Engineering, Colorado School of Mines, Golden, Colorado 80401, United States

‡3M Fuel Cell Components Program, 3M Company, St. Paul, Minnesota 55144, United States

§X-ray Science Division, Argonne National Laboratory, Argonne, Illinois 60439, United States

*Corresponding Author

regimes. Isoscattering points were absent in similar water uptake experiment for the films after boiling. Annealing at elevated temperature results in morphology change and improves proton conductivity.

2.2 Introduction

Proton exchange membrane (PEM) fuel cells have advantages over other fuel cells in terms of their high power density and lower temperature of operation. However, there is much interest in operating these devices at hotter and drier conditions to enable system simplification and to minimize the presence of liquid water and the need for system humidification.[1,2] In order to produce PEM fuel cells, which meet both the cost and performance requirements, it is desirable to generate new materials that have higher proton conductivities and better durability in an operating fuel cell. As a starting point it is necessary to understand the properties of the incumbent materials that work well under conditions of water saturation. Perfluorosulfonic acid (PFSA) membranes are currently widely used in PEM fuel cells because of their high proton conductivity, good thermal and chemical stability, and their ability to maintain their mechanical integrity under harsh operating conditions.[3,4] The Nafion Membrane (Scheme 2.1 top) was developed in the late 1960s by Walther Grot at DuPont and still serves as a benchmark PEM PFSA material. Several other PFSA membranes have subsequently been introduced by other companies such as the 3M Company (Scheme 2.1 bottom),[5] Solvey-Solexis,[6] and Dow.[7,8] These PFSA-based membranes all have similar structures: a hydrophobic polytetrafluoroethylene (PTFE)-like backbone and hydrophilic side chains, which contain a $SO^{3-}X^{+}$ end group, where X can be a proton or another cation. In contact with water, the side chain becomes hydrated and the sulfonic acid dissociates providing a proton. During fuel cell operation, the proton is thought to

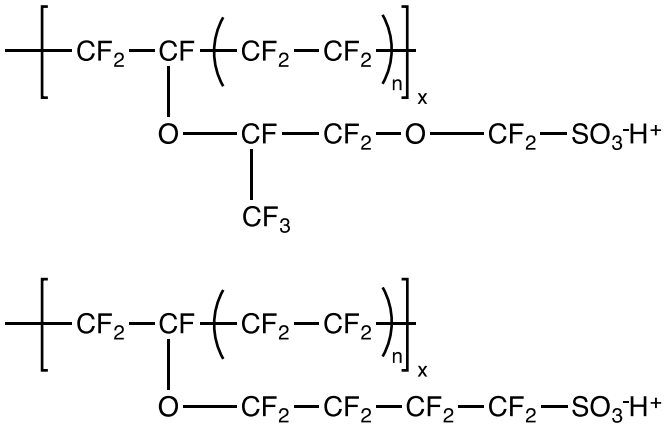

Scheme 2.1 Structure of Nafion™ Membrane (top) and 3M PFSA Ionomer (bottom).

be transported through the PEM via a combination of the vehicle[9,10] and Grotthus mechanisms.[11] The observation is that practical levels of proton conduction occur under conditions of water saturation in PFSA PEMs. Structurally, the physical and chemical properties of PFSA membranes depend largely on the equivalent weight (EW), which is defined as the number of grams of dry ionomer per mole of sulfonic acid groups when the material is in the acid form, and the length and structure of the side chain. These properties are also affected by different thermal treatments, such as annealing (i.e., the thermal treatment conditions above the T_{α}, the onset temperature of long-range mobility of the ionomer main chains and side chains via a thermally activated destabilization of the electrostatic interactions, which yields a dynamic network involving significant ion-hopping processes). For reference, β-relaxation was found to be due to principally main-chain (backbone) motions within the framework of a static physically cross-linked electrostatic) network,[12] necessary to form mechanically robust films, can also greatly change the properties and performance of a PFSA membrane. Other factors that influence film forming such as casting from different solvents and film thickness may affect membrane properties and performances as well. Although the morphology of PFSA membranes has been

investigated extensively using small-angle X-ray scattering (SAXS) and other characterization techniques since the 1970s,[4] the exact morphology is still highly debated. Part of the reason for this is that the membranes pretreatment conditions has a significant effect on its properties, and the films used in these studies have not been pretreated in exactly the same manner. Through the history of the study of PFSA ionomers, various morphological models have been proposed based on different observations and assumptions, including the cluster network model,[13] the core−shell model,[14] the lamella model,[15] and the parallel cylindrical channel model.[16]

Generally, it is thought that the morphology changes with different water sorption states, as suggested by Gebel et al. In addition, a structural inversion may take place at a 50% solvent content, i.e., the system undergoes a transformation from polymer in solvent to solvent in polymer or vice versa, and that the shape of different structural levels will also vary accordingly.[17] Small perturbations in the conditions under which these films are studied, such as stretching, have been shown to dramatically change their morphology and proton conductivity.[18-20] We suggest in this paper that the conditions under which films are prepared for SAXS by various experimenters are not always equivalent and that the PFSAs studied may not be in their equilibrium structure.

In order to obtain in-depth morphological information on PFSA membranes under environmental conditions, SAXS (using synchrotron radiation) is one of the most useful characterization techniques, capable of giving dynamic information during thermal treatments or hydration events. Typical SAXS images are shown in our previous work[21] and in Figure 2.1 for a sample of the 3M PFSA. Typically there are three structural features (peaks or upturns) observed in the SAXS patterns due to the short-range and long-range differences in electron density between structures of different types and their backgrounds. The interpretations of the origin of

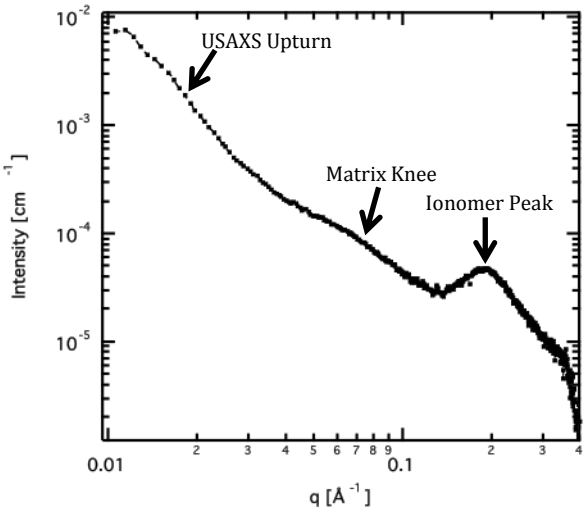

Figure 2.1 A typical SAXS pattern of 3M PFSA membranes.[4]

these peaks/ upturns are still being debated based on which structural model is being invoked. The peak in the high-q region is usually attributed to the so-called ionomer peak, which originates from the constructive scattering of the ionic clusters.[4] This peak will vary with different cations and different water uptake levels. The cluster network model proposed by Gierke et al. attributes the ionomer peak to interparticle scattering between ionomer clusters, which are distributed in an organic paracrystalline matrix of a similar structure to liquid water. The core-shell model, on the other hand, suggests the ionomer peak originates from intraparticle scattering of short-range order inside the core−shell structure, which is also distributed in the para-crystalline region. The core−shell model matches the experimental observations well, for it can better explain the fact that microswelling dominates over macroswelling; however, its poor fitting to the data over a wide range of length scales made it somewhat neglected until recently.[16] The upturn in the q = 0.04−0.08 $Å^{-1}$ region is named the matrix knee and arises from the scattering by the crystalline region.[22] If completely amorphous structures were made, e.g., by quenching, this knee pattern would no longer be observable. The upturn of intensity in the very

low-q region is the ultrasmall angle upturn, which is caused the long-range order of larger structures.[22-25]

In this paper we present a study of the evolution of morphology in a PFSA ionomer from casting, annealing, initial hydration, and boiling. SAXS is used to investigate the 3M PFSA ionomer (Scheme 2.1 bottom), complemented by water uptake measurements. In previous work we presented the static wet and dry SAXS data for a series of EWs of this film annealed at 160 °C.[21] The data were analyzed by a numerical model, the unified fit, and a graphical method, the clipped random wave model. The results from the two models were in good agreement with each other and with the dissipative particle dynamic model of the ionomer.[26] Although this modeling provided useful information on the size of the scattering objects, it did not provide any conclusive information on the morphology of the polymer. Here we first study the water equilibration of an unannealed film. This is followed by the effect of water uptake on the swelling of films with various pretreatments. Next we present an investigation of the dynamic morphological changes that occur during or after annealing at temperatures above the T_α or from the effect of film thickness as a function of RH, temperature, and EW. Finally, we show the initial hydration of annealed films varies by their thermal history. We show that isoscattering points are observed in the dynamic annealing experiments of the unannealed films for measurement performed at 50, 80, and 95 °C, indicating a possible change in the symmetry of the scattering objects in these size regimes. We discuss this data in terms of the changes to the morphology that occur when these PFSA films are formed and hydrated.

2.3 Experimental Section

Detailed description of the experimental materials and experimental methods about

SAXS, DVS and conductivity measurement are presented in this section.

2.3.1 Materials

PFSA films were cast from an ionomer to provide membranes thicknesses of either 20 or 50 μm. The membranes were then dried at 110 °C. The films were then annealed at either 180, 190, or 200 °C for 20 min. The annealed films were boiled in deionized (DI) water, 3% H_2O_2, 0.5 M H_2SO_4, and DI water for 1 h each, to remove organic and ionic contaminants and to ensure all of the ionomer film is in the acid form. A piece of unannealed 825 EW film, a piece of the same film annealed at 190 °C for 5 min, and a piece of annealed film boiled by the process described above were used in the water uptake measurement.

2.3.2 SAXS Measurement

SAXS data were obtained using beamline 12ID C-D at the Advanced Photon Source (APS) at Argonne National Laboratory, Argonne, IL, using X-rays of 18 keV. The experimental setup is shown in Figure 2.2. A custom-made, humidity- controlled oven oven with four sample slots covered with Kapton windows was used. During each experiment, three samples were loaded in to the oven, and one slot was used for a Kapton blank. Humidity was achieved by mixing dry and humidified N_2. Gas flow was controlled with mass flow controllers (MKS Mass-Flo RS-485 controller). Wet N_2 was bubbled through deionized water in a humidifying bottle (Fuel Cell Technologies, Inc.) with dry N_2 entering downstream. Dew points were monitored by a Visala HMT337 humidity sensor allowing the RH to be calculated. The oven temperature was controlled by a Watlow PID temperature controller. Dynamic annealing was carried out on an

unannealed 825 EW PFSA film. The 50 μm films were put into the oven for 20 min at 200 °C, and multiple SAXS patterns were recorded using a 0 s delay and a 3 s exposure time. In addition, a full dynamic experiment was performed on the same films as follows: the film was annealed at 200 °C for 5 min and then cooled to 80 °C, and immediately after, a dynamic humidification was performed from 25% to 95% RH. Multiple SAXS patterns were again recorded during this process. Both dynamic and steady-state SAXS measurements of humidification experiment at 80 °C as well as 25%, 50%, 75%, and 95% RH were performed on the films with different thicknesses, equivalent weights, and casting dispersions.

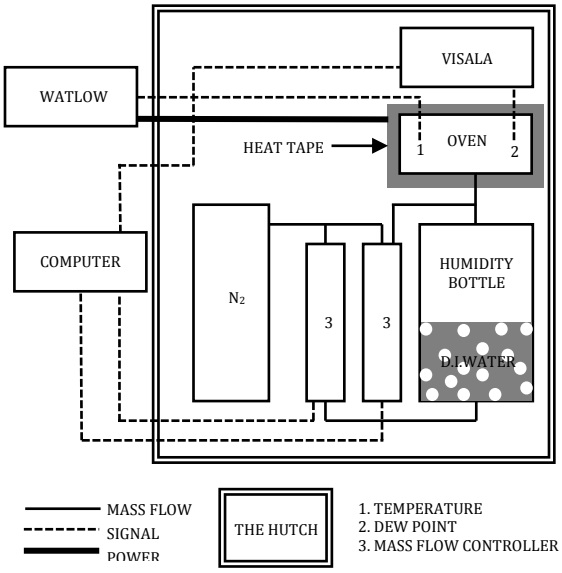

Figure 2.2 Experimental setup of the environmentally controlled sample SAXS measurement.

For the ex-situ annealing experiments, the conditions were as follows: The oven was set to 25% RH, and three SAXS patterns were recorded for each film and one pattern was recorded for the Kapton background; then the oven was set to 50% RH, where 45 SAXS shots were taken while the films equilibrated for about 20 min. Then, three patterns were recorded on the films

and on the Kapton blank. The same steps were performed up to 95% RH. For the long-term water equilibration study, the sample was taken out of the water and loaded very quickly into the RH chamber, and SAXS images were recorded at 100% RH. During the SAXS measurements, the q range was adjusted for different samples by adjusting the camera length.

2.3.3 DVS Measurement

Dynamic vapor sorption (DVS Advantage, SMS Inc.) measurements were performed on the 825 EW PFSA unannealed film, annealed film, and boiled annealed film. Water sorption experiments were carried out at similar conditions to the SAXS experiments in order to obtain accurate values of water sorption under the different RHs studied. The membrane was put into a humidity chamber, which is set to a constant temperature. The RH of the chamber was programmed to stay at 0% RH for 20 min and then increased in the order of 25%, 50%, 75%, and 95% RH in a step-by- step manner corresponding to the SAXS experiments, with a 20 min equilibrating time for each step. The mass change of the membrane with time and RH was recorded. With the dry weight of the membrane measured, the λ values which are defined as number of water molecule attached per $-SO_3H$ group were calculated: $\lambda = wEW/18$, where $w = (m_{wet} - m_{dry})/m_{dry}$. Water sorption isotherms were obtained for various 3M ionomer films. No condensation was observed by the in-situ camera during the water sorption range we studied.

2.3.4 Conductivity Measurement

Proton conductivity was measured for films annealed at 3 different temperatures. Electrochemical impedance spectroscopy (EIS) with a Bio-Logic VMP3 potentiostat was

adopted to obtain the impedance profiles over a wide range of frequency (from 100 000 to 0.7 Hz). A four-electrode in-plane setup was used in these measurements.[27] Specific conductivity was calculated from $\sigma = d/Rlh$, where σ is specific ionic conductivity, d is the distance between two inner electrodes, R is the measured resistance, l is the membrane width, and h is the membrane thickness.

2.4 Data Processing

In this work, we used the Irena macros package for Igor Pro for the unified fit model[28] to analyze the SAXS data. A representative fit is shown in our previous work.[21] Through these fits, quantitative information such as radius of gyration (R_g) was obtained for the different structural levels observed. The unified fit is applicable to a variety of systems such as filled polymers, foams, polymer blends, colloids, and composites, etc.[29] In addition, values of R_g were also obtained through a one-level local fit;[30] the Porod factors were obtained using a Porod fit.[28] Full details of the mathematics involved in the unified fit are shown below:

For a dilute and isotropic system with $q<<1/R_g$,[31] we have the well known Guinier's law for the scattering intensity: [28]

$$I(q) = I_e N_p \rho_e^2 \exp(-R_g^2 q^2/3)$$

N_p is the particle density in the scattering volume; I_e is the scattering factor for a single electron; ρ_e is the electron density in a particle; R_g is the radius of gyration; and q is the scattering vector.

For the "structurally limited" Porod scattering, which assumes a curved Porod region[28], with the motion of the particle is considered, the Porod's law expression for the form factor becomes:[28]

$$\overline{F^2(q)} \cong 2\pi\rho_e^2 S\left\{\left[\mathrm{erf}\left(qR_g/6^{1/2}\right)\right]^3/q\right\}^p$$

S is the surface area of the particle, and p is the porod factor.

The combination of Guinier component and structurally limited Porod component is found to be capable of modeling a wide variety of systems, which is called unified fit model:[28]

$$I(q) = G\exp\left(-q^2R_g^2/3\right) + B\{\left[\mathrm{erf}\left(qR_g/6^{1/2}\right)\right]^3/q\}^p$$

Where $G=n^2N_pI_e$ and $B=2\pi N_p\rho_e{}^2S_pI_e$.

For structures with multiple structural levels, with the smaller structures superimposed on the larger structure, the following expression is used:[28]

$$I(q) \cong \sum_1^n \left(G_i\exp\left(-q^2R_{gi}^2/3\right) + B_i\exp\left(-q^2R_{g(i+1)}^2/3\right) \times \left\{\left[\mathrm{erf}\left(qR_{gi}/6^{1/2}\right)\right]^3/q\right\}^{pi}\right)$$

For a densely packed system which shows correlation between particles, a structure factor S(q) is used to modify the intensity with $AF(q)^2$ being the intensity of independent scattering, the express for the intensity becomes:[29]

$$\overline{I(q)} = AF(q)^2S(q)$$

2.5 Results and Discussion

The high energy (18 keV) of the APS X-rays allows us to collect SAXS images in <1 s. This enables the study of dynamic morphological changes in polymer structures in situ not accessible via conventional laboratory X-ray sources. To ensure that we were not observing artifacts due to the variation of the film thickness, a SAXS study on a series of 825 EW films as a function of thickness was first performed, which will be discussed in the later section. No

significant variation in the SAXS data was seen with thickness from 11 to 45 μm. The data reported in the remainder of this paper are for the 45 μm film.

2.5.1 Water Equilibration Study

We were interested to see how a sample of unannealed as-cast 825 EW PFSA exposed to liquid water at ambient temperature would change with time: if it would eventually have the same SAXS features as the boiled state, and how long that would take, or if it would eventually just swell to dissolution or some other form. From the SAXS patterns (Figure 2.3), we see a shift of the ionomer peak from q = 0.165 $Å^{-1}$ in the as-cast 825 EW film to q = 0.145 $Å^{-1}$ in the materials equilibrated in water for 33 h with a large increase of intensity as the unannealed film takes up water. This trend continues as the membrane was equilibrated in liquid water over time, giving q = 0.124 $Å^{-1}$ after water equilibration at ambient temperatures after 26 days. One-half of the swelling observed after almost 1 month was obtained in the first day. Unsurprisingly, PFSA ionomers swell in water and form lager structures as the ionomer swells.[32] The data obtained from the unified fit for R_g and the calculated D-spacing are shown in figure 2.4. The process to reach true equilibrium is clearly very slow for the PFSA membrane in the water sorption process.[33,34]

The change of the shape of the SAXS patterns is also observed. The slopes of the lines below q = 0.1 $Å^{-1}$ which obey a power law continue to decrease, indicating the changing of particle shape of both ionic and crystalline domains upon water uptake and relaxation of the polymer structure.[28] We notice that the crystalline matrix knee is hardly discernible in the SAXS patterns of the unannealed film and the 33 h water equilibrated film and appears more noticeably, with an increase in intensity, at q = 0.8 $Å^{-1}$ for the 26 day equilibrated film, similar to the boiled

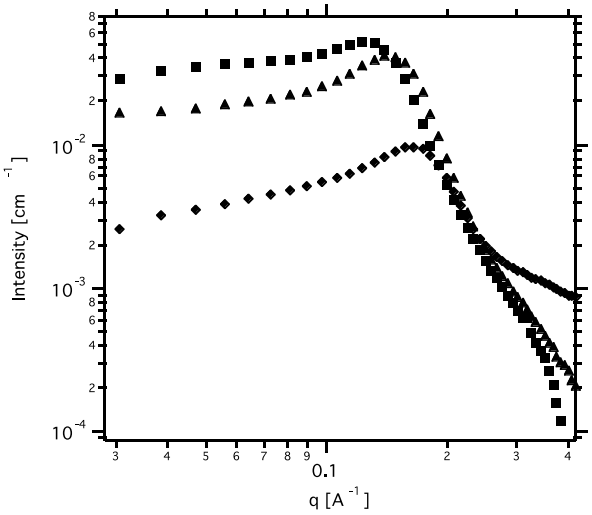

Figure 2.3 SAXS patterns of the long-term water equilibration experiment on 825 EW 3M PFSA films: (⧫) unannealed; (▲) 33 h in DI water; (■) 26 days in DI water.

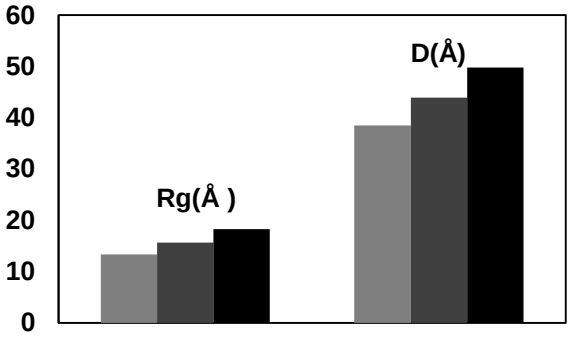

Figure 2.4 Unified fit R_g and calculated D-spacing of 3M PFSA films with different water equilibrating time: (light gray) unannealed; (dark gray) 33 h in DI water; (black) 26 days in DI water.

film, where the change takes place much more rapidly. In fact, WAXS measurements, not shown, confirm that the 825 EW material has a very low crystallinity index of 0.09. This suggests that uptake of water could plasticize the polymer chain, making morphological changes

from amorphous to orderly structures or crystallization possible.[35-37] However, we should note again that the morphological changes of the PFSA membranes at room temperature take place very slowly.

2.5.2 Water Sorption Study

A piece of unannealed 825 EW film, a piece of such film annealed for 190 °C for 5 min, and a piece of such annealed film which is also boiled in deionized (DI) water, 3% H_2O_2, 0.5 M H_2SO_4, and DI water for 1 h each were used in the water uptake measurement. In order to explain the morphological information for the membranes at different water contents, it is necessary to obtain the number of water molecule per sulfonic acid site, i.e., the λ value, under the corresponding conditions of the SAXS measurement. This information is conveniently obtained using a dynamic vapor sorption instrument set to the same RH for the same time periods as the SAXS measurements. For the 825 EW film dried at 110 °C, or subsequently annealed or annealed and boiled using the SAXS data, presented and discussed below, we were able to calculate the D-spacing of the ionomer peak. The D-spacing is defined as $2\pi/q$ from the position of the SAXS ionomer peak. Combining the SAXS and DVS results, we obtain the relationship between the D-spacing of the ionomer clusters and λ of the film (Figure 2.5). From this figure, we see that the D-spacing for the films increases with amount of water taken up by the film as a result of swelling. Using simple geometric arguments, the D-spacing would have a linear dependence on λ, if the swelling corresponded to a swelling lamellar structure, or a $\lambda^{1/2}$ or $\lambda^{1/3}$ dependence which would correspond to a cylindrical or spherical structure, respectively.[38]

We first consider the swelling of the unannealed dried film of the 825 EW ionomer (Figure 2.5). This film shows a swelling relationship with D of $\lambda^{1/6}$; the dependence change at

different water contents cannot be attributed to the swelling of any one simple geometrical object. However, this behavior is that predicted for a self-repelling polymer chain.[39] This is explained as these membranes are not expected to have any crystallinity in their hydrophobic backbones as they have not been annealed by heating above their T_α. These results are supported by our dynamic SAXS experiments of hydration discussed in the following section, which also suggest a changing morphology upon different water uptake levels as these dried only films are swelled. It should be noted that the study by Gebel et al. also shows a changing morphology of the PFSA Nafion™ membrane upon water uptake.[17,40]

A comparison of the domain spacing−water content relationship for films with different treatment conditions, i.e., unannealed, annealed for 5 min at 190 °C, and annealed and boiled films for 1 h, is also shown in Figure 2.5. For the annealed film we see that the D-spacing becomes smaller at the same amount of water sorption the as-cast film. The D-spacing relationship to λ is almost but not quite linear, which may be indicative of crystallite lamella in the form of ribbons in the structure. The intercept of both the as-cast and annealed films seem to converge at ca. 26 Å at a λ value of 1, which would represent as dry as an ionomer film could achieve under the conditions to which it was exposed here. Annealing does not destroy the ionomer domains, but the heating has changed the morphology with the new swelling behavior consistent with increased chain entanglement. The annealed film does not swell as much as the unannealed film. Boiling an ionomer film rapidly equilibrates a membrane to its fully hydrated state, making a variety of tests more consistent than the same tests performed at a transient state of hydration. The boiled film may represent the state of the film after break-in, in a fuel cell. Here we see that the ionomer peak after boiling is much larger; extrapolation would suggest ca. 42 Å at a λ value of 1. The swelling of this peak is not as dramatic as for the unboiled films and

shows no trend in D versus λ that can be easily attributed to the swelling of one geometric object. Although different swelling behavior may indicate different geometry of the swelling structure, still more data points are needed to conclude the exact morphology which led to corresponding swelling behavior.

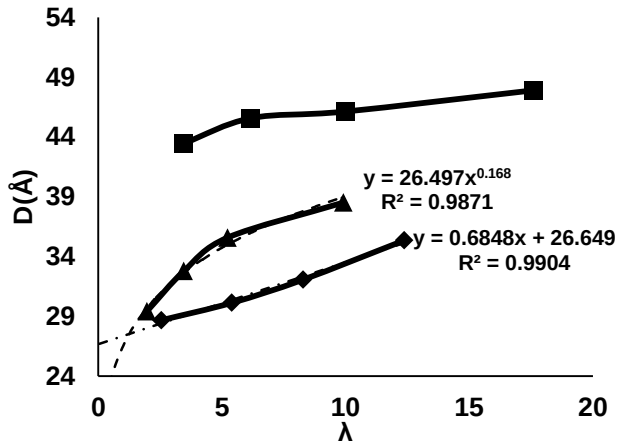

Figure 2.5 D-spacing calculated from ionomer peak positions of SAXS patterns of the 3M 825 EW membrane with different pretreatment conditions at different water uptake: (▲) unannealed; (⧫) annealed at 190 °C for 5 min; (■) annealed and boiled for 1 h.

2.5.3 Annealing Study

PFSA films are typically annealed above their T_α to facilitate chain entanglement and to induce crystallinity in the polymer backbone, giving the material intrinsic strength and added stability toward long-term dissolution in hot water. The T_α of the 3M ionomer has been determined to occur at 100 °C.[41] The decomposition temperature of PFSAs is widely accepted to be as high as 280 °C.[42,43]

2.5.3a Ex-Situ Annealing

For the films annealed at three different temperatures (180, 190, and 200 °C) and then boiled in deionized (DI) water, 3% H_2O_2, 0.5 M H_2SO_4, and DI water for 1 h each, the SAXS patterns are shown in Figure 2.6 (top). From the unified fit results shown in Figure 2.6 (bottom), we can see that generally sizes of both the crystalline and ionomer cluster regions increase as the annealing temperature increases from 180 to 190 °C. This is due to the polymer chains having larger mobility close to or above the T_α gives rise to the development of crystallinity on cooling[44] and the electrostatic affinity of ionic domains drives them to form larger clusters. This agrees with the study by Hensley et al. for thin membranes (ca. 20 μm).[45] The increase of domain sizes becomes less obvious for the ionic domain as the annealing temperature increases to 200 °C, especially at low RH. While for the crystalline domain, the films annealed at 200 °C show a larger crystalline size feature at 95% RH compared to the same film at 25% RH; this suggests some morphological changes have taken place in the higher temperature annealing, making water a better plasticizer[35-37] for the PFSA backbone to form larger crystalline regions upon water uptake. The morphological changes resulting from annealing have substantial effect on the proton conductivity, as we can see from figure 2.7: at 80 °C and 95%RH, the proton conductivity increases from 0.20 to 0.25 S/cm as annealing temperature increases from 180 to 190 °C. This is due to the ionic conductive channel, which becomes wider (from 11.9 to 15.5 Å) as annealing temperature increases from 180 to 190 °C, as mentioned above. Interestingly, the conductivity increases substantially (from 0.25 to 0.36 S/cm) as annealing temperature increases from 190 to 200 °C, despite the minimal increase of domain sizes. We then investigated the power law slope

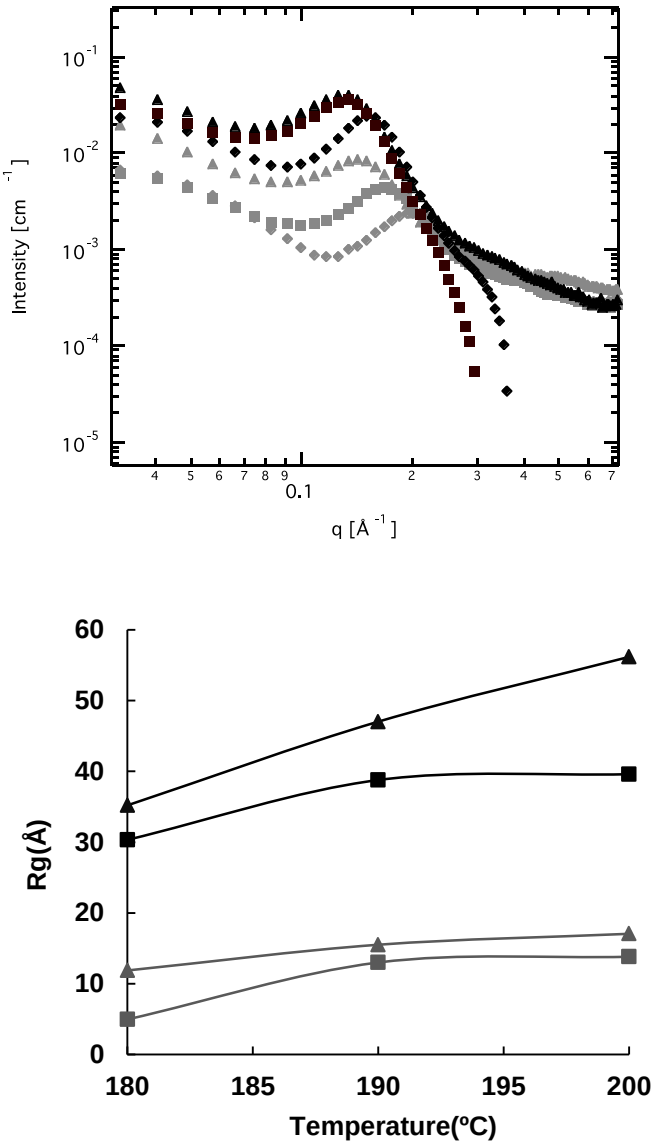

Figure 2.6 SAXS patterns and unified fit results for an annealing study of the 3M PFSA membranes. SAXS patterns of ex-situ annealing of 3M 825 EW PFSA films at different temperatures (top): (gray diamond) 25% RH and 180 °C; (gray triangle) 25% RH and 190 °C; (gray square) 25% RH and 200 °C; (black diamond) 95% RH and 180 °C; (black triangle) 95% RH and 190 °C; (black square) 95% RH and 200 °C. Unified fit results of ex- situ annealing of 3M 825 EW PFSA films at different temperatures (bottom): (gray square) 25% RH level 1; (gray triangle) 95% RH level 1; (black square) 25% RH level 2; (black triangle) 95% RH level 2.

of the low q range of the SAXS pattern and found out that the inverse power law slope shows no significant change (from 1.5 to 1.4), when annealing temperature increases from 180 to 190 °C, while it decreases to 1.1 as annealing temperature reaches 200 °C, indicating the formation of lower dimension and more elongated crystal structures. Therefore, the increase of conductivity from 190 to 200 °C annealing temperatures is primary caused by a geometrical change of polymer domains.

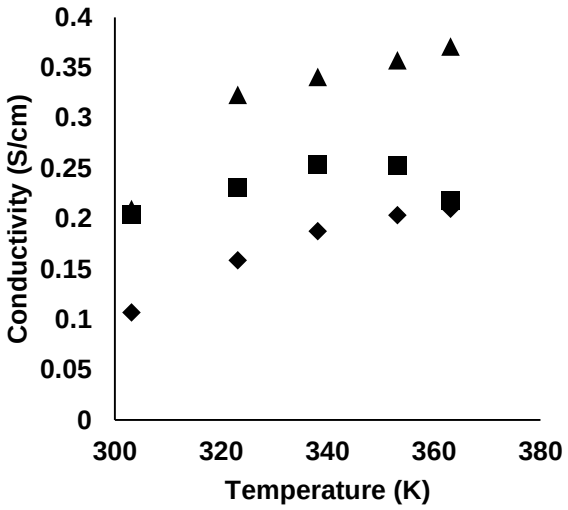

Figure 2.7 Conductivity at 95%RH of films annealed at (◆) 180 °C, (■) 190 °C, and (▲) 200 °C

2.5.3b In-Situ Annealing

For the in-situ dynamic annealing experiments on the 50 μm 825 EW film (Figure 2.8), we can see from the dynamic SAXS patterns shown in Figure 2.8 (top): as the annealing proceeds, the scattering intensity of the crystalline level of q range between 0.027 and 0.085 $Å^{-1}$ decreases, which shows that the crystalline structures were disrupted as the backbone chains gain thermal energy and become very mobile, i.e., the polymer melted. While for the ionic cluster

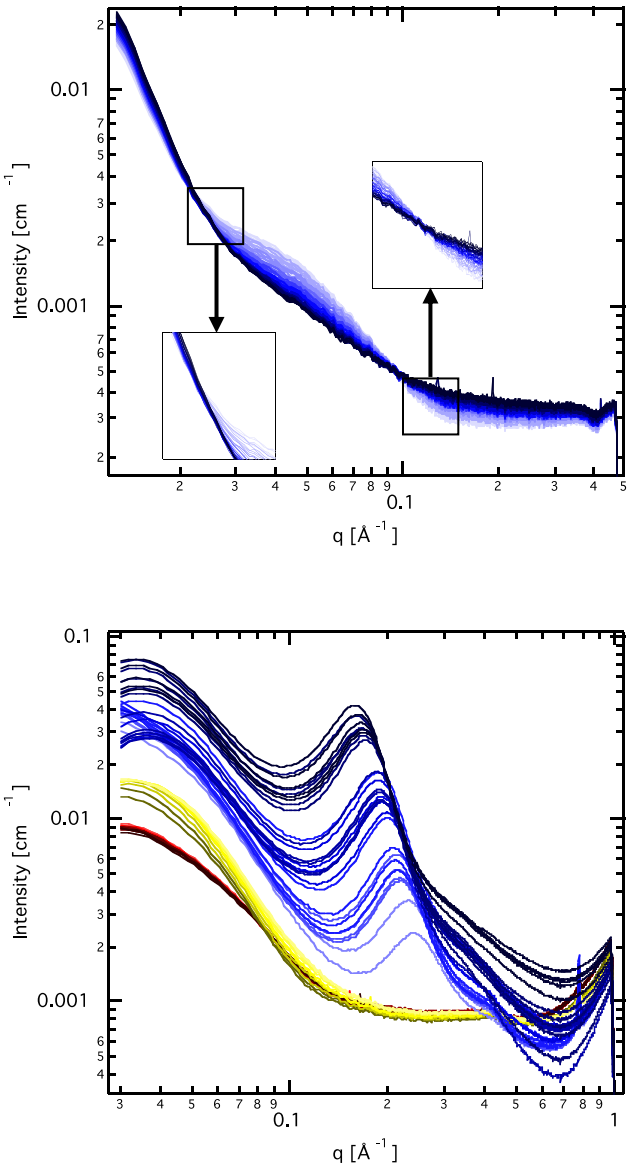

Figure 2.8 SAXS patterns of in-situ dynamic annealing of 20 min at 200 °C on 3M 825 EW PFSA films (top): annealing time increases from the light to dark colors. SAXS patterns of the full dynamic experiment on 3M 825 EW PFSA membranes (bottom): patterns from light to dark red: film annealed at 200 °C for 5 min; from dark yellow to light yellow: film cooled from 200 to 80 °C; from light blue to dark blue: film humidified from 25% RH to 95% RH.

region of q = 0.148−0.332 $Å^{-1}$, although the scattering intensity increases, there is no ionic peak due to the very dry conditions, 0% RH, giving no contrast and so no scattering. Two isoscattering points are observed at q = 0.0228 and 0.0989 $Å^{-1}$. This is an indication of the polymer melting and the lack of any water in the hydrophilic domains of the polymer[46] as well as the decrease of particle number density[47] taking place in the annealing process.

In Figure 2.8 (bottom), we show SAXS data for film annealing under practical conditions where the film is held at 200 °C for 5 min followed by quenching as fast as the oven would allow to 80 °C for 5 min, followed by its initial hydration. The first 5 min of annealing shows a similar result to the longer dynamic annealing experiment as shown in Figure 2.8 (top). During the cooling process the crystalline hydrophobic region forms low q. Further studies will be required to determine the effect of rate of cooling on this process. We speculate that if the sample had been cooled very fast, most of the structure would have remained amorphous, resulting in less crystallinity after annealing. For this experiment, we see general results of higher crystallinity after annealing, from the increase of intensity of the crystalline peak at the q range of 0.032−0.143 $Å^{-1}$. The humidification immediately after the cooling shows a continuing increase of the crystalline level; we suspect it is due to the plasticization of water on the PFSA ionomer. We also observe the evolution of the ionomer peak in the q range between 0.158 and 0.240 $Å^{-1}$. This SAXS profile agrees well with other studies of other PFSAs.[45]

2.5.4 SAXS Study on the Effect of Hydration

The effect of hydration on the film's morphology were investigated through in situ SAXS measurement at different RHs and temperatures for both unboiled and boiled films, as shown in figure 2.9.

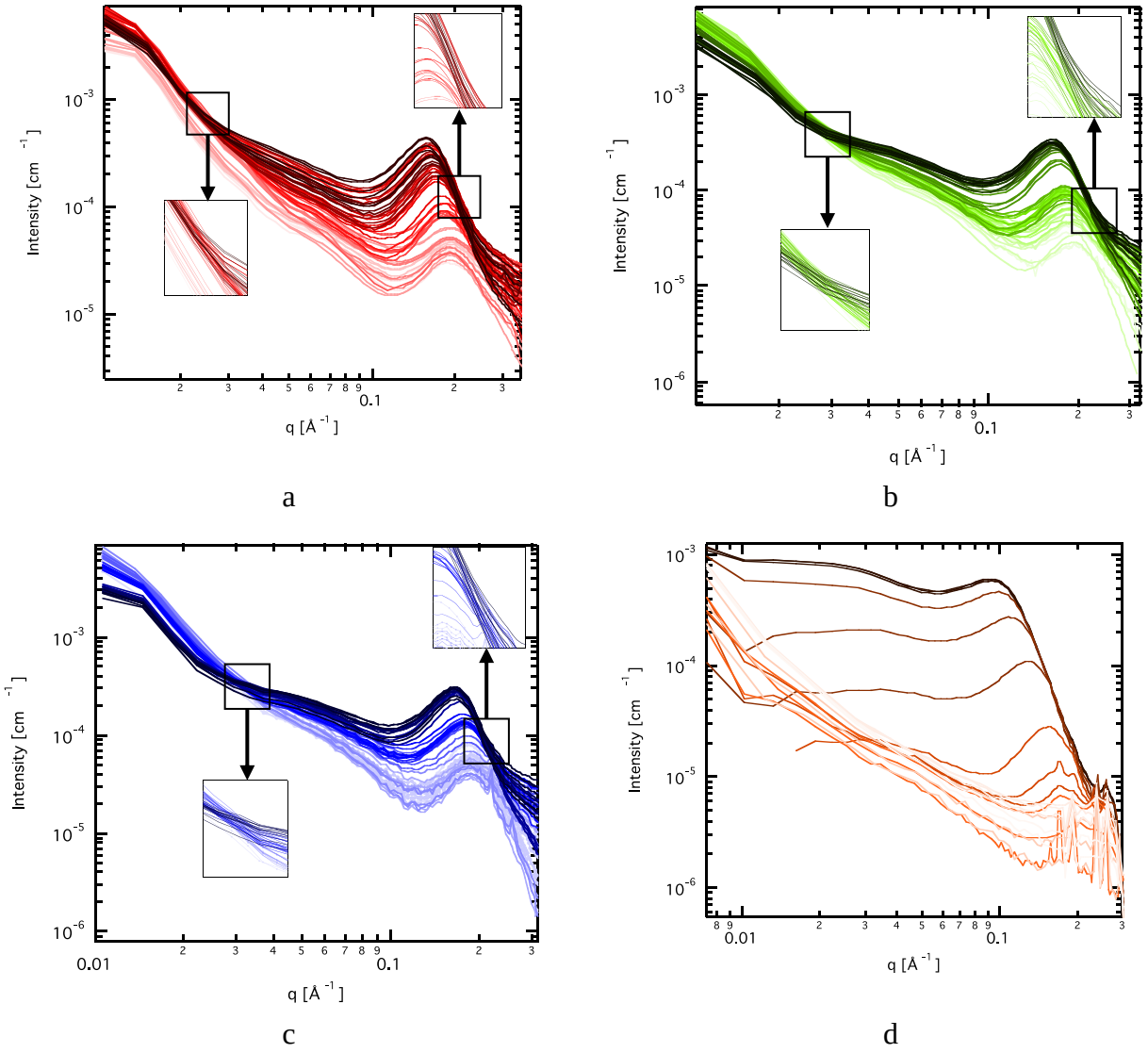

Figure 2.9 SAXS patterns of dynamic humidification of unannealed PFSA membranes from 25% to 95% RH at (a) 50, (b) 80, and (c) 95 °C, and (d) boiled PFSA film at 80 °C. Light colors are dry, and dark colors are wet.

2.5.4a Unboiled Films

From the dynamic SAXS patterns of the unboiled films, which are annealed at 200 °C for 10 min (Figure 2.9a−c), the hydrophilic ionomer peaks, resulting from interparticle interference, can be seen in the q range between 0.158 and 0.205 $Å^{-1}$, 0.162 and 0.191 $Å^{-1}$, and 0.164 and 0.186 $Å^{-1}$ at 50, 80, and 95 °C, respectively. The second structural level, i.e., of the crystalline backbone on the other hand, results in a less obvious pattern in the scattering profile. The feature observed resembles the crystalline knee often cited for as supplied Nafion^{TM} membrane due to the fact that the crystalline structures are a weaker correlated system than the ionic structures. Generally both hydrophilic and hydrophobic peaks/ knees shift to a lower q range as relative humidity increases, which indicates an increase of particle domain spacing as the effect of swelling.

We observed isoscattering points for the SAXS patterns of the swelling of the unannealed, PFSA films, at q = 0.024, 0.220 $Å^{-1}$; q = 0.029, 0.223 $Å^{-1}$; and q = 0.030, 0.211 $Å^{-1}$ for measurements performed at 50, 80, and 95 °C, respectively. The isoscattering points are caused by scattering from systems undergoing a phase transition as the scattering objects change their symmetry on swelling. In this study, we observed two isoscattering points at different values of q, for unboiled films at three different temperatures, indicating changes in the symmetry of the scattering objects taking place at two different length scales, i.e., phase transition within the hydrophilic ionic domain and hydrophobic crystalline domains, induced by the effect of heating and hydration,[46,48] and possibly the decrease of particle number density.[47] Since the scattering intensity is the linear combination of scattering from two different scattering structures, $I = FI_1 + (1 - F)I_2$,[49,50] where F is the fractional composition of each. The scatterers at each level are composed of two phases, starting with a total composition of unity. As a result, all

scattering curves will pass the points where $I = I_1 = I_2$, independent of F, i.e., the composition of these two phases. Therefore, the change of composition between two phases induced by the humidification process makes a series of changing SAXS patterns, which pass the isoscattering points. From the SAXS patterns, we clearly see the changing of the under lying slope that can be fit to a power law of both structural levels at different water uptake (Figure 2.9a−c), indicating a changing morphology of the films upon hydration, contrary to results suggested for annealed films[51] which claims an invariable particle shape independent of water content with only the change of particle size.

Table 2.1 Parameters from Numerical Fitting and Calculation for an 825 EW 3M PFSA Ionomer (Fits Agree with Experimental Data to ≤5%)

		Unified Fit Results		Local Fit Results		Calculated D-spacing	Porod Fit Results	Calculated Rod-like Structure Dimensions	
Membrane Type	SAXS Experiment Conditions	Level#1 R_g (Å)	Level#2 R_g (Å)	Level#1 R_g (Å)	Level#2 R_g (Å)	Level#1 D (Å)	Level#2 P Factor	D* (Å)	L* (Å)
un-annealed	50℃/25%RH	4.6	24.6	6.3	21.7	31.4	1.5	N/A	N/A
un-annealed	50℃/95%RH	12.5	38.4	11.0	30.8	40.1	1.1	75.4	218.2
un-annealed	80℃/25%RH	7.0	28.8	7.4	23.5	32.1	2.4	N/A	N/A
un-annealed	80℃/95%RH	11.7	34.4	10.4	27.0	38.7	1.1	71.5	197.4
un-annealed	95℃/25%RH	9.1	27.1	9.3	24.8	33.4	2.6	N/A	N/A
un-annealed	95℃/95%RH	13.6	32.9	10.5	N/A	38.4	1.2	69.7	212.6
boiled	80℃/25%RH	N/A	N/A	N/A	N/A	N/A	1.3	N/A	N/A
boiled	80℃/95%RH	22.9	71.1	19.2	N/A	66.9	0.7	N/A	N/A

Numerical fittings were performed on the SAXS patterns of the annealed 825 EW films at the start (25% RH) and the end (95% RH) of the dynamic swelling experiments. Values of the Porod factor "P" and radius of gyration, R_g, at different RHs are shown in Table 2.1. Different values of the Porod P factor correspond to different particle symmetries. From Table 2.1, we notice that for the hydrophobic crystalline structure, when the RH reaches 95%, the P factor

becomes about 1, indicating a randomly distributed rod-like structure[29,52] which also fits the cylinder model recently proposed for Nafion™.[16] This shows the particle shape changes with different hydration states.[17] The rod-like structure is of length $L^* = 2\pi/q_1$ and diameter $D^* = 2\pi/q_2$, where q_1 and q_2 are the q values at the start (low q) and the end (high q) of the region of slope = −1 on the log−log SAXS patterns.[22] The calculated L* and D* are shown in Table 2.1, showing a D* of ca. 72 Å and a L* of ca. 209 Å. The R_g obtained from the unified fits is in good agreement with the values obtained by our previous SAXS studies in PFSA membranes[21] and shows an increase of particle size upon water uptake. The radiuses of gyration of unboiled films are in the range of 4.6−13.6 Å for the ionic clusters and 24.6−32.9 Å for the crystalline structures, depending on RH. For the boiled films, this becomes 22.9 Å for the ionic clusters and 71.2 Å for the crystalline structure.

The results of a local fit to one structural level are also shown in Table 2.1. From both the unified fit and the local fit, we observe an hydrophilic ionic structure, at low RH, i.e. 25% RH, which appears to be larger at higher temperatures (increase from 4.6 Å at 50 °C to 9.1 Å at 95 °C for the unified fit; from 6.3 Å at 50 °C to 10.5 Å at 95 °C for the local fit), while at higher RH, i.e., 95% RH, this temperature dependence is not observed, resulting in less swelling of this feature at higher temperatures. For the hydrophobic crystalline structure, no such dependence is observed. The calculated D-spacing of the hydrophilic ionomer level (range from 31.4 to 40.1 Å depending on RH and temperature) also reflects the swelling of the films, which is in good agreement with the results of the size changes we obtained from numerical fitting. We noted that the values of D-spacing are generally bigger than the values of the diameter (defined as diameter $= 2((5/3)^{0.5})R_g$ for a spherical object); this is because we clearly see the effect of dense packing from the ionomer peak on the SAXS pattern and use a correlated system which accounts for the

interparticle interference to fit our experimental SAXS data, rather than use an intraparticle scattering mechanism, as suggested by many studies, such as the core−shell model.[38]

2.5.4b Boiled Films

Upon boiling in DI water for 1 h, films show more equilibrated properties, in which dynamic changes are much less obvious, often allowing more steady-state data to be obtained. For the water-boiled 825 EW annealed film (Figure 2.9d), similar peak/knee shifts as the unboiled films are observed. The peaks/knees of both structural levels are at much lower q and have a higher intensity compared to those of the unboiled films, indicating an increase in size and abundance of ionic conductive channels caused by larger amount of water uptake. Interestingly, at the start of the experiment at 25% RH, the boiled film shows almost no ionomer peak. A comparison of R_g for the unboiled films and the boiled films at 95% RH shows an increase in swelling as an effect of water sorption upon boiling from an R_g of ca. 12−22 Å.[21] Isoscattering points are absent on the SAXS patterns of preboiled samples due to the fact that the reorientation of the polymer to a randomly distributed rod like structure, P ca. 1, observed upon initial hydration of the films was completed during the boiling prior to the humidification process.

2.5.5 Equivalent Weight Study

In Figure 2.10, we show the results of the unified fit analysis on the SAXS data for a series of PFSAs of differing EW (SAXS not shown). These materials were all annealed at 200 °C for 10 min. Depending on EW and RH, the R_g of the first structural level, i.e., the ionic clusters

ranges from 7.4 to 14.7 Å, and that of the second structural level, which is formed by backbones, ranges from 24.9 to 34.3 Å. At the lowest EW studied, 700, there is no crystalline structure formed by the backbone observed. We can see that as the as EW increases above 825, the R_g of the second structural level increase approximately linearly. This is because polymers of larger EW have higher portion of the hydrophobic backbone; hence, they form larger crystalline structures as they have a higher fraction of tetrafluoroethylene.

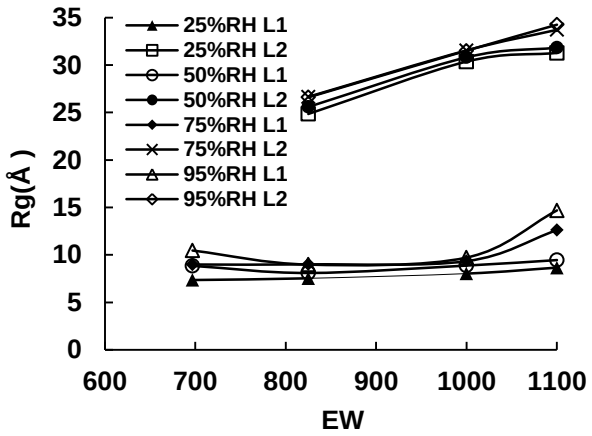

Figure 2.10 Unified fit results of 3M PFSA films with different equivalent weights.

For the first level, the sizes of ionic clusters remain mostly constant, increasing at an EW of 1100. This observation agrees with our previous work.[21] The ionic clusters for the 825 EW film were ca. 1/2 the size of those observed for the less severe annealing condition of 190 °C for 5 min. We also notice that the sizes for both structural levels are smaller than these for the materials we studied in our previous work.[21] This is due to the fact that the materials for this study are not boiled prior to the measurements, accounting for smaller domains. All of the ionic clusters swelled upon hydration. The reason for the larger ionic cluster at 1100 EW is curious;

one possible reason is that the energy required for the polymer coil to deform is less for the polymer with less side chains, i.e., of higher EW, and it is easier to form larger ionic clusters under the same conditions than for ionomers with lower EW.

A study from molecular dynamics simulations suggests that polymers with longer separation distances between side chains form larger domain spacing, which is in good agreement with our observations.[21] This is possibly because the ionic clusters are at a relatively stable energy state compared to those at low EW films.[26] It is observed that the 700 EW films do not have a crystalline region, as there is not enough TFE to from one. This low equivalent weight film also has shows more swelling than the 825 and 1000 EW films ionic cluster domains due to its gel-like behavior.

2.5.6 Solvent Study

The solvents from which an ionomer is cast could have a big effect on the properties of the membrane. We can see significant differences in the SAXS patterns of the cast films from two different solvents, water and aqueous methanol (Figure 2.11.). Membranes cast from H_2O do not show a crystalline hydrophobic region as shown by the absence of the crystalline knee in the middle q range between 0.135 to 0.293 $Å^{-1}$.[44] While the membranes cast from aqueous MeOH still maintain their crystalline structure, and have larger hydrophilic ionomer clusters from the presence of obvious ionomer peaks at q=0.183 $Å^{-1}$ and 0.229 $Å^{-1}$. Also, we notice that the structures of the membranes cast from MeOH take up more water upon the humidification process. The interaction between the polymer and solvent in the casting process, and the residual solvent remaining in the as-cast membrane play an important role in the morphology of the membrane. Therefore, the solubility parameters of the solvents and the 3M ionomer, and the rate

of evaporation of both solvents will be important parameters. These parameters are tabulated in table 2.2. The PFSA shows dual solubility parameters due to the presence of the backbone region and the side chain groups, and they are calculated using the group contribution method.[53] The ionomer shows different solubility behavior in different solvents, and gives rise to the different morphologies of the cast membranes. From table 2.2, we notice that the solubility parameter of MeOH is very close to that of the SO_3H group, therefore, the cast film will form very large ionic clusters, as we see from the ionomer peaks at q=0.183 $Å^{-1}$ and 0.229 $Å^{-1}$in the SAXS patterns, Figure 2.11. For the same reason, since H_2O has a solubility parameter twice that of the SO_3H group, and the ionomer peak in this case, q=0.402 $Å^{-1}$, is almost absent from the SAXS pattern. We also notice that the crystalline region is absent from the H_2O cast films, while we can observe crystalline peaks in the SAXS patterns of MeOH cast films at q=0.035 and 0.039 $Å^{-1}$. This is also due to the fact that MeOH has a solubility parameter, which is closer to that of the 3M ionomer backbone. Another reason for the formation of the larger ionomer clusters upon hydration for MeOH cast films is the lower boiling point of MeOH, and its higher volatility. This means MeOH will evaporate faster than water under the same temperature and pressure. A more porous structure will form as a result of the rapid evaporation of the solvent,[54] and this structure makes the film form larger water conductive channel domains upon humidification, which is consistent with the SAXS profile, Figure 2.11. However, we found from the water sorption isotherm shown in Figure 2.12, that overall the aqueous MeOH cast film is more hydrophobic than the H_2O cast film. This is due to the fact that the aqueous MeOH cast films form a larger portion of crystalline domains than the H_2O cast films, as mentioned above.

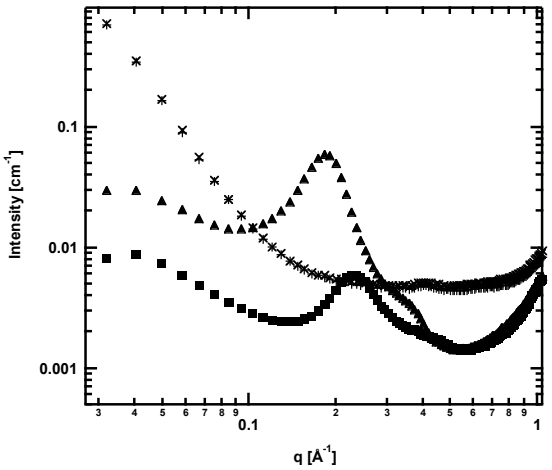

Figure 2.11 SAXS patterns of 3M PFSA films at different RHs and cast from different solvents: (■) at 25%RH for films cast from MeOH; (▲) at 95%RH for films cast from MeOH; (+) at 25%RH for films cast from H_2O; (×) at 95%RH for films cast from H_2O.

Table 2.2 Solubility Parameter and Boiling Point of Solvents and Ionomer

Solvent	Solubility Parameter ($J^{1/2}$ $cm^{-3/2}$)	Boiling Point at 1 bar (°C)
MeOH	29.7	65
H_2O	47.9	100
3M PFSA Backbone	14.5	N/A
SO_3H Group	26.2	N/A

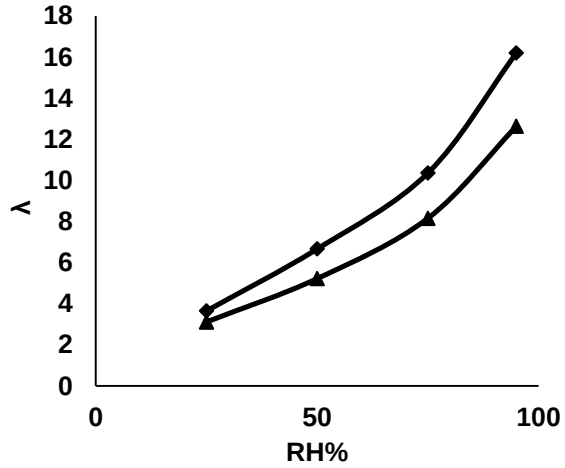

Figure 2.12 Water sorption isotherm of 3M PFSA films cast from different solvents. (▲) Cast from MeOH; (◆) Cast from H_2O.

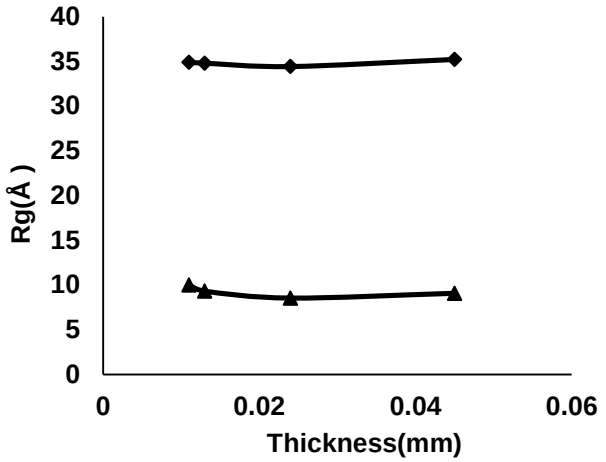

Figure 2.13 Unified fit results of 3M PFSA films of different thicknesses. (▲) Hydrophilic ionic cluster level at 80% RH; (◆) hydrophobic crystalline level at 80% RH.

2.5.7 Thickness Study

From figure 2.13, we notice the R_g of the ionic clusters range from 8.5 to 10.0Å and that of crystalline structures range from 34.4 to 35.2 Å, with little effect of the thickness on the size of both structural levels observed. This is simply due to the fact that the difference in thickness is not significant in the thickness range studied (0.011mm to 0.045mm), and the mass transfer is governed by interfacial transport of water, with a constant solvent concentration boundary condition at the surface of the film.[55] Water is transported from both sides of the membrane and a pseudo steady state is rapidly achieved. An approximately flat water-concentration profile is established very rapidly. As the SAXS images were recorded, the structures in the films had already reached a pseudo steady state structure. Therefore, the films with different thicknesses will reach the same degree of micro swelling of the structure levels within a very short time scale. The effect of membrane thickness on water uptake will be more obvious for thicker membranes with larger thickness differences, because of the effect of mass and heat transfer, and subsequently will affect the morphology of the membranes.[56]

2.6 Conclusion

In this paper we showed changes in the microswelling of the 3M PFSA that occur between the unannealed, annealed, and boiled films. We showed that the swelling behavior of the ionic domains in the 3M PFSA differed between the unannealed film, showing no polymer chain entanglement, to the almost laminar morphology of the annealed film, to the more random behavior of the boiled material. The observation of isoscattering points observed during dynamic annealing or dynamic hydration experiments on unboiled annealed films shows that the symmetry of certain domain sizes in the polymer clearly changes during these events. Using the unified fit model for the 825 EW PFSA annealed films show the size of ionic clusters is in the range of R_g = 4.6−13.6 Å and the crystalline backbone structures in the range of 24.6−34.4 Å, while values for the boiled films are much larger, 22.9−71.1 Å. We obtained a P factor of hydrophobic level of about 1 for 825 EW films at 95% RH, suggesting a rod-like structure for the polymer backbone. The backbone PTFE-like structural level is found to increase with EW (range between 700 and 1100) 25−35 Å. For hydrophilic domains the size increases with RH, showing larger increases at both the lowest and highest EW studied. From long-term water equilibrating experiment, we see a large increase of the size and abundance for both structural levels and also the very long time scale required for PFSA to achieve equilibrium. Annealing at higher temperatures leads to the formation of larger ionic domains and the change of film's domain geometry and results in the increase of proton conductivity. Films casted from MeOH shows defined ionic and crystal features, while these casted from H_2O are amorphous. Membrane thickness exerts no effect to domain sizes for the thickness range we studied.

2.7 Acknowledgement

This research was supported by the U.S. Department of Energy (DOE), EERE Cooperative Agreement No. DE-FG36- 07G017006, and in part by the Renewable Energy MRSEC funded by the NSF under Grant DMR-0820518. Use of the Advanced Photon Source, an Office of Science User Facility, operated for the DOE Office of Science by Argonne National Laboratory, was supported by the DOE under Contract No. DE-AC02-06CH11357. DOE support does not constitute an endorsement by DOE of the views expressed here. We also thank Ashley M. Maes, Melissa A. Vandiver, and Himanshu N. Sarode for their help with the SAXS experiments.

2.8 References

(1) Zhang, J. L.; Xie, Z.; Zhang, J. J.; Tanga, Y. H.; Song, C. J.; Navessin, T.; Shi, Z. Q.; Song, D. T.; Wang, H. J.; Wilkinson, D. P.; Liu, Z. S.; Holdcroft, S. *Journal of Power Sources* **2006**, *160*, 872.

(2) Shao, Y. Y.; Yin, G. P.; Wang, Z. B.; Gao, Y. Z. *Journal of Power Sources* **2007**, *167*, 235.

(3) Hamrock, S. J.; Yandrasits, M. A. *Polymer Reviews* **2006**, *46*, 219.

(4) Mauritz, K. A.; Moore, R. B. *Chemical Reviews* **2004**, *104*, 4535.

(5) Haugen, G. M.; Meng, F. Q.; Aieta, N. V.; Horan, J. L.; Kuo, M. C.; Frey, M. H.; Hamrock, S. J.; Herring, A. M. *Electrochemical and Solid State Letters* **2007**, *10*, B51.

(6) Stassi, A.; Gatto, I.; Passalacqua, E.; Antonucci, V.; Arico, A. S.; Merlo, L.; Oldani, C.; Pagano, E. *Journal of Power Sources* **2011**, *196*, 8925.

(7) Tant, M. R.; Darst, K. P.; Lee, K. D.; Martin, C. W. *Acs Symposium Series* **1989**, *395*, 370.

(8) Whiteley, L. D.; Martin, C. R. *Journal of Physical Chemistry* **1989**, *93*, 4650.

(9) Kreuer, K. D. *Chemistry of Materials* **1996**, *8*, 610.

(10) Kreuer, K. D.; Rabenau, A.; Weppner, W. *Angewandte Chemie-International Edition in English* **1982**, *21*, 208.

(11) Glasstone, S.; Laidler, K. J.; Eyring, H. *The theory of rate processes: the kinetics of chemical reactions, viscosity, diffusion and electrochemical phenomena*; McGraw-Hill Book Company, Incorporated, 1941.

(12) Osborn, S. J.; Hassan, M. K.; Divoux, G. M.; Rhoades, D. W.; Mauritz, K. A.; Moore, R. B. *Macromolecules* **2007**, *40*, 3886.

(13) Hsu, W. Y.; Gierke, T. D. *Journal of Membrane Science* **1983**, *13*, 307.

(14) Fujimura, M.; Hashimoto, T.; Kawai, H. *Macromolecules* **1981**, *14*, 1309.

(15) Litt, M. H.; *Polym. Prepr.*: **1997**; Vol. 38, p 80.

(16) Schmidt-Rohr, K.; Chen, Q. *Nature Materials* **2008**, *7*, 75.

(17) Gebel, G. *Polymer* **2000**, *41*, 5829.

(18) Park, J. K.; Li, J.; Divoux, G. M.; Madsen, L. A.; Moore, R. B. *Macromolecules* **2011**, *44*, 5701.

(19) Li, J.; Park, J. K.; Moore, R. B.; Madsen, L. A. *Nature Materials* **2011**, *10*, 507.

(20) Page, K. A.; Landis, F. A.; Phillips, A. K.; Moore, R. B. *Macromolecules* **2006**, *39*, 3939.

(21) Aieta, N. V.; Stanis, R. J.; Horan, J. L.; Yandrasits, M. A.; Cookson, D. J.; Ingham, B.; Toney, M. F.; Hamrock, S. J.; Herring, A. M. *Macromolecules* **2009**, *42*, 5774.

(22) Rubatat, L.; Rollet, A. L.; Gebel, G.; Diat, O. *Macromolecules* **2002**, *35*, 4050.

(23) Eikerling, M.; Kornyshev, A. A.; Spohr, E. *Fuel Cells I* **2008**, *215*, 15.

(24) Li, Y. J.; Peiffer, D. G.; Chu, B. *Macromolecules* **1993**, *26*, 4006.

(25) Rubatat, L.; Gebel, G.; Diat, O. *Macromolecules* **2004**, *37*, 7772.

(26) Paddison, S. J.; Elliott, J. A. *Journal of Physical Chemistry A* **2005**, *109*, 7583.

(27) Janarthanan, R.; Horan, J. L.; Caire, B. R.; Ziegler, Z. C.; Yang, Y.; Zuo, X.; Liberatore, M. W.; Hibbs, M. R.; Herring, A. M. *Journal of Polymer Science Part B: Polymer Physics* **2012**.

(28) Beaucage, G. *Journal of Applied Crystallography* **1995**, *28*, 717.

(29) Beaucage, G.; Schaefer, D. W. *Journal of Non-Crystalline Solids* **1994**, *172*, 797.

(30) Guinier, A.; Paris.

(31) Roe, R. J. *Methods of X-ray and neutron scattering in polymer science*; Oxford Univ. Press: New York, 2000.

(32) Sugiyama, M.; Mitsui, T.; Sato, T.; Akai, Y.; Soejima, Y.; Orihara, H.; Na, Y. H.; Itoh, K.; Mori, K.; Fukunaga, T. *Journal of Physical Chemistry B* **2007**, *111*, 8663.

(33) Bass, M.; Freger, V. *Polymer* **2008**, *49*, 497.

(34) Satterfield, M. B.; Benziger, J. B. *Journal of Physical Chemistry B* **2008**, *112*, 3693.

(35) Bauer, F.; Denneler, S.; Willert-Porada, M. *Journal of Polymer Science Part B-Polymer Physics* **2005**, *43*, 786.

(36) Corti, H. R.; Nores-Pondal, F.; Buera, M. P. *Journal of Power Sources* **2006**, *161*, 799.

(37) Onishi, L. M.; Prausnitz, J. M.; Newman, J. *Journal of Physical Chemistry B* **2007**, *111*, 10166.

(38) James, P. J.; Elliott, J. A.; McMaster, T. J.; Newton, J. M.; Elliott, A. M. S.; Hanna, S.; Miles, M. J. *Journal of Materials Science* **2000**, *35*, 5111.

(39) Witten, T. A. *Journal of Chemical Physics* **1982**, *76*, 3300.

(40) Kusoglu, A.; Santare, M. H.; Karlsson, A. M. *Polymer* **2009**, *50*, 2481.

(41) Schaberg, M. S.; Abulu, J. E.; Haugen, G. M.; Emery, M. A.; O'Conner, S. J.; Xiong, P. N.; Hamrock, S. J. *Polymer Electrolyte Fuel Cells 10, Pts 1 and 2* **2010**, *33*, 627.

(42) Samms, S. R.; Wasmus, S.; Savinell, R. F. *Journal of the Electrochemical Society* **1996**, *143*, 1498.

(43) Wilkie, C. A.; Thomsen, J. R.; Mittleman, M. L. *J Appl Polym Sci* **1991**, *42*, 901.

(44) Moore, R. B.; Martin, C. R. *Macromolecules* **1988**, *21*, 1334.

(45) Hensley, J. E.; Way, J. D.; Dec, S. F.; Abney, K. D. *Journal of Membrane Science* **2007**, *298*, 190.

(46) Chalal, M.; Ehrburger-Dolle, F.; Morfin, I.; Bley, F.; de Armas, M. R. A.; Donaire, M. L. L.; San Roman, J.; Bolgen, N.; Piskin, E.; Ziane, O.; Casalegno, R. *Macromolecules* **2010**, *43*, 2009.

(47) Caremans, T. P.; Loppinet, B.; Follens, L. R. A.; van Erp, T. S.; Vermant, J.; Goderis, B.; Kirschhock, C. E. A.; Martens, J. A.; Aerts, A. *Chemistry of Materials* **2010**, *22*, 3619.

(48) Chalal, M.; Ehrburger-Dolle, F.; Morfin, I.; de Armas, M. R. A.; Lopez, M. L.; Bley, F. In *14th International Conference on Small-Angle Scattering (SAS09)* Oxford, ENGLAND, 2009; Vol. 247.

(49) Nicolai, T.; Pouzot, M.; Durand, D.; Weijers, M.; Visschers, R. W. *Europhysics Letters* **2006**, *73*, 299.

(50) Panda, D.; Datta, A. *Applied Spectroscopy* **2008**, *62*, 341.

(51) Kim, M. H.; Glinka, C. J.; Grot, S. A.; Grot, W. G. *Macromolecules* **2006**, *39*, 4775.

(52) Roe, R.; New York: Oxford University Press.

(53) Ravindra, R.; Krovvidi, K. R.; Khan, A. A. *Carbohydrate Polymers* **1998**, *36*, 121.

(54) Shao, L.; Chung, T. S.; Wensley, G.; Goh, S. H.; Pramoda, K. P. *Journal of Membrane Science* **2004**, *244*, 77.

(55) Silverman, T. J.; Meyers, J. P.; Beaman, J. J. *Journal of the Electrochemical Society* **2010**, *157*, B1376.

(56) Dimitrova, P.; Friedrich, K. A.; Vogt, B.; Stimming, U. *Journal of Electroanalytical Chemistry* **2002**, *532*, 75.

CHAPTER 3 A COMBINED THEORETICAL AND EXPERIMENTAL INVESTIGATION OF THE TRANSPORT PROPERTIES OF WATER IN A PERFLUSOROSULFONIC ACID PROTON EXCHANGE MEMBRANE DOPED WITH THE HETEROPOLY ACIDS, $H_3PW_{12}O_{40}$ OR $H_4SiW_{12}O_{40}$

Reproduced from *J. Phys. Chem. C* 2014, 118, 854-863. Copyright ACS 2014.

Yuan Liu,[†,§] Somisetti V. Sambasivarao,[†,§] James L. Horan,[†] Yuan Yang,[‡] C. Mark Maupin,[*,†] and Andrew M. Herring[*,†]

3.1 Abstract

The 3M 825EW perfluorosulfonic acid (PFSA) ionomer was doped with the heteropoly acids (HPAs), $H_3PW_{12}O_{40}$ (HPW) and $H_4SiW_{12}O_{40}$ (HSiW). Dynamic vapor sorption measurements at 95% RH showed a decrease in water content as a result of HPA doping from $\lambda = 8.05$ for the undoped 825EW 3M ionmer to $\lambda = 4.40$ for a 5% HSiW doped film. FTIR measurement revealed strong interactions between the HPAs, ionomer, and H_2O. Irrespective of hydration level, it was found that the PFSA films showed tortuous proton diffusion behavior. At maximum hydration and 25 °C, the self-diffusion coefficient of water was found to decrease upon addition of HPA from 4.97 to 2.19 ($\times 10^{-6}$ cm^2/s) for the undoped 825EW 3M ionomer and 1% HPW, respectively, in excellent agreement with computation. The model at low HPA

[†]Department of Chemical and Biological Engineering, Colorado School of Mines, Golden, Colorado 80401, United States

[‡] Department of Chemistry and Geochemistry, Colorado School of Mines, Golden, Colorado 80401, United States

[*]Corresponding Authors

[§]These authors contributed equally.

loadings revealed the decreased diffusion coefficient was due to the water preferentially residing near the HPA as opposed to the SO_3^- groups. The addition of HPA generally improved overall conductivity due to additional formation of hydrogen-bonding networks between the HPA particles. At high RH, it was observed that the proton conductivity increased while the water diffusion coefficient decreased as HPA was incorporated. In addition, a mismatch between the conductivity values and those calculated from the Nernst−Einstein equation using the self-diffusion coefficient of water in the system indicated an enhancement in Grotthuss hopping mechanism upon addition of HPA.

3.2 Introduction

Perfluorinated proton exchange membranes (PEMs) have been shown to provide favorable properties such as high power densities, dynamic operation, and system versatility for their use in polymer electrolyte fuel cells.[1] Over the years, several PEM materials have been developed, such as Nafion by the Dupont Co., an ionomer by the 3M Co.,[2,3] and a short side-chain ionomer, Aquivion, currently produced by Solvay Solexis.[4,5] The morphology of these films is highly debated and believed to change under different thermal and hydration levels.[6] However, it is generally accepted that they will form a hydrophilic/ hydrophobic phase separated morphology, due to their chemical structures, that is, a hydrophobic polytetrafluoroethylene (PTFE) backbone and a hydrophilic side-chain.[7,8] In these systems, practical proton conductivity is achieved at adequate water saturation. Only under very wet conditions do ion conductive channels form that are capable of transporting protons through a combination of vehicular diffusion[9,10] and the Grotthuss mechanisms.[11,12] Therefore, the water retention capability and proton conductivity of the PEM will be greatly reduced at elevated temperatures and lower RH

with the current incumbent materials. However, excessive water uptake and swelling will decrease the mechanical strength and result in bad contact between the PEM and the electrode, which is found to be especially severe for low equivalent weight films. It is also beneficial for fuel cells to operate at lower water inlet RH to reduce system complexity and improve overall system volumetric power density. The ability to operate at higher temperatures can also simplify the heat exchange system.[13] Because of the competitive adsorption of CO and H_2, higher operating temperatures are desirable because they shift the adsorption equilibrium toward a lower CO and higher H coverage of the catalyst sites.[14]

One solution to this problem is achieved through the addition of inorganic solid oxide materials such as heteropoly acids (HPAs).[15-18] HPAs are proton conducting super acids and a subset of the polyoxometallates, which contain a central heteroatom, addenda atoms, oxygen atoms, and acidic hydrogen atoms. The structures and ion conductive properties of HPAs have been studied extensively.[19-21] The best-known structure of the HPAs is the Keggin, $H_nXM_{12}O_{40}$, structure (Figure 3.1). In the crystal structure, the anions of the HPAs are thought to be interconnected either by hydronium ions or by solvated protons residing in an extended hydrogen-bonding network of waters to form a secondary structure, depending on the hydration conditions.[19] It has been shown that HPAs have very high proton conductivity in the solid state and are therefore ideal additives to enhance proton conducting characteristics.[20] Because of the HPAs' strong interactions with the sulfonic acid groups of the ionomers,[16] morphological and chemical changes may occur in the hydrophilic ionic clusters. Upon doping, alteration of performances and properties of the PFSAs under drier conditions should improve.

In this work, we investigated the water sorption, proton conduction, and transport properties, as a result of HPA addition to the PFSA ionomer experimentally and through

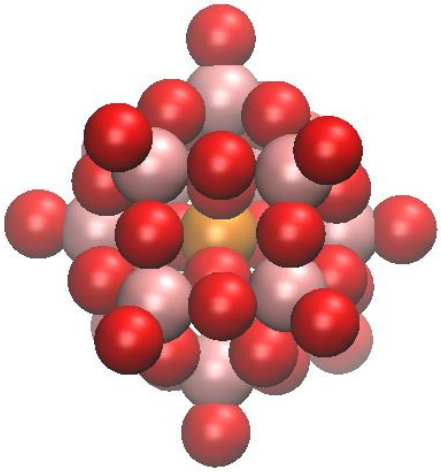

Figure 3.1 Keggin structure of a heteropoly acid. The P (orange), W (pink), and O (red) are depicted by Van der Waals spheres generated using the Visual Molecular Dynamics visualization software. [22]

molecular dynamics simulations. For this study, the commercially available 12-phosphotungstic acid, $H_3PW_{12}O_{40}$ (HPW), and 12-silicotungstic acid, $H_4SiW_{12}O_{40}$ (HSiW), which have the Keggin structure (Figure 2.1),[17,18] were added to the 825EW PFSA ionomer from 3M.

A significant amount of experimental research has been conducted on the effect of HPA addition to the performance and properties of PFSAs.[1,15,17,18,21,23-26] Malhotra et al. conducted the first study on Nafion™ membrane impregnated with HPA and found a dramatic improvement in power density at elevated temperatures for HPA impregnated films as compared to traditional ionomer films.[24] Fenton et al. measured in situ the resistance and conductivity of phosphotungstic acid (PTA)/ Nafion™ composite film and concluded that improvement in the proton conductivity of the composite membrane was mainly caused by lowering the barrier for proton hopping.[25] They also investigated the size effect of HPA particles on the conductivity of HPA doped Nafion™ films and found that only nanosize particle improved proton conductivity

by bridging the water clusters in Nafion™.[26] Savadogo et al. studied the ionic conductivity and hydration of various HPA doped Nafion™ films in fuel cells and concluded that the silicotungstic acid (STA)/Nafion™ composite film had the highest ionic conductivity and that the water uptake of HPA doped film was greater than for the undoped Nafion™ 117 membranes.[23] Our early work[17] revealed the strong interaction of HPAs with the ionomer and a shifting of the IR bands for HPA to lower energy. Morphology alteration was also observed from small-angle X-ray scattering (SAXS) measurement upon addition of HPA and for various hydration levels. Diffusion coefficients were found to increase at the minimum hydration level as a result of HPA addition, while the opposite trend was observed under maximum hydration. Proton conductivity generally increased in HPA doped films as opposed to undoped films. It was speculated that the Grotthuss mechanism dominating over the vehicle mechanism at this maximum hydration level, but no definitive proof was available.

In addition to the vast experimental literature, molecular dynamics simulations have been used to elucidate the molecular level interactions of PEMs.[27-34] In Nafion™, a perfluoronated hydrocarbon similar to 3M, it has been determined that the waters available to the system primarily reside near the charged sulfonic acid groups.[27] The diffusion of the hydrated excess proton, which is typically delocalized over several waters, was found to strongly depend on the local environment's charge distribution, hydration levels, and the pendant side-chain motion. These findings strongly indicate a highly coupled system with properties vastly different from bulk water proton transport.[28,29] One significant difference from bulk water systems is that the transport of water and protons is highly dependent on interactions with the sulfonic functional groups in the hydrophilic pockets.[30,31] Overall, the proton transport is believed to occurs through the Grotthuss shuttling mechanism as opposed to vehicular transport.[29]

In our recent study on Nafion™ and the 3M ionomer with different water models using MS-EVB and molecular dynamics simulations,[35] it was found that the self-diffusion coefficient of the excess proton was higher for the 3M ionomer than for Nafion™ at 300 K and for high hydration levels. This line of work also continues from our preliminary work,[17] which showed an improvement in proton conductivity of the 3M ionomer by doping with HPAs, but offered little explanation of how this worked. In this article, we present, for the first time, the simulated transport properties of water in the 3M ionomer doped with HPAs. We present an improved comparison between experimental and theory of the doped film to the transport properties of the pure 3M ionomer at different hydration levels. A consideration of morphological behavior from the investigation of tortuous transport phenomena of water and our molecular dynamic simulated PEM morphology also provides new insights into the ion transport behavior of the hybrid PEM materials.

3.3 Methods

Experimental materials and procedures of DVS, ATR FTIR, EIS and PGSE-NMR measurements are described below. Details of the computational simulation method are also provided in this section.

3.3.1 Materials

HSiW and HPW were obtained from Aldrich and dried at 110 °C in an oven for 12 h prior to use. The 825EW 3M ionomer casting dispersion in a solvent of mixed n-propanol and water was provided by 3M and was used as control. An appropriate amount (corresponding to

the desired doping level) of the dried HPA was dissolved in the casting dispersion. The casting dispersion with dopant was cast on a Kapton^{TM} sheet and then dried in oven under 50 °C for 20 min to a uniform dried thickness of 40 μm, using a multigap applicator. The dried films were then annealed at 180 °C for 10 min. The following films doped with weight percentage (wt %) of HPA or HSiW were made: 0% HPA (undoped), 1% HPW, 5% HPW, 1% HSiW, and 5% HSiW.

3.3.2 DVS Measurement

The water uptake of films under different relative humidity (RH) was measured by dynamic vapor sorption (DVS Advantage, SMS Inc.). The membrane was put into a humidity chamber, which was set to a constant temperature, and the dynamic weight change of the membrane with respect to time and RH was recorded. All samples were dried in a vacuum oven overnight before DVS measurements. The λ values[36-38] defined as the number of water molecules per charge were calculated from $\lambda = w*EW/18$, where $w = (m_{wet} - m_{dry})/m_{dry}$, with dry weight taken as the weight after the initial 4 h in the DVS oven at 0% RH. Water sorption isotherms were obtained for all films doped with different loadings of HPW or HSiW.

3.3.3 ATR FTIR Measurement

A Thermo Nicolet Nexus 470 FTIR spectrometer with a Specac GS11000 ATR unit was used to perform attenuated total reflectance (ATR) infrared measurements at 80 °C under dry and wet conditions. For the dry condition, samples were predried in a vacuum oven overnight. Dry N_2 was set to a flow rate of 100 SCCM during the measurement to preserve the samples RH levels. N_2 either flowed directly to the environmental chamber to achieve dry condition or passed

through DI water to maintain wet condition.

3.3.4 Proton Conductivity Measurements with EIS

Impedance profiles over a wide range of frequency (from 100 000 to 0.7 Hz) were obtained through electrical impedance spectroscopy (EIS) measurements with a Bio-Logic VMP3 potentiostat. A four-electrode in-plane setup was adopted in these measurements.[39] Model fits were then performed on the impedance profiles using an equivalent circuit shown in Figure 3.2, to obtain the resistance values. Specific conductivity was calculated from $\sigma = d/Rlh$, where σ is specific ionic conductivity, d is the distance between two inner electrodes, R is the measured resistance, l is the membrane width, and h is the membrane thickness. Different temperature and humidity were achieved through a Testequity H1000 oven.

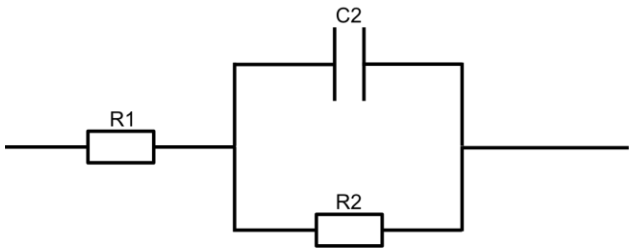

Figure 3.2 The equivalent circuit used in the analysis of the Electrical Impedance Spectroscopy to determine the conductivity.

3.3.5 Proton Diffusion Measurement with PGSE (Pulsed Gradient Spin−Echo) NMR

Pulsed gradient spin−echo (PGSE) NMR proton diffusion measurements were carried out on a Bruker AVANCEIII NMR spectrometer operating at 400 MHz using a 5 mm Bruker single-axis DIFF60L Z-diffusion probe, and a nine-interval stimulated-echo pulse sequence.[39,40] For

each measurement, 32 scans were performed with the gradient, g, being set to a suitable range for each sample. Values of the spin echo attenuation, E, at different g were obtained and then fit to the "Stejskal and Tanner" equation to obtain the diffusion coefficient:[40]

$$E(g,\Delta) = E(g,2\tau) = \frac{S(g,2\tau)}{S(0,2\tau)} = \exp\left(-\gamma^2 g^2 D\delta^2\left(\Delta - \frac{\delta}{3}\right)\right)$$

where g is the gradient, γ is the gyromagnetic ratio, and D is the apparent diffusion coefficient. Samples were put in an NMR tube and flushed with dry N_2 gas, and then sealed to achieve minimum hydration, or a drop of DI water was added to the bottom of the tube using a syringe, and then sealed to reach 100% RH. All samples were prepared at least 72 h prior to the measurements to achieve equilibrium.

3.3.6 Computational Simulations

The DRIEDING force field potential[41] was used to describe the 825EW 3M ionomer membrane, as it has previously been successfully used to study polymers.[35,41] The force field for HPW was taken from the density functional calculations of Brodbeck et al.,[42] while the flexible 3-centered (F3C)[43] force field was used to model the waters and the classical hydronium ions. The 3M polymeric systems were created using a previously developed code[44] resulting in an entangled polymer system at the experimentally determined density. The resulting system contained 64 polymers with each polymer made of 10 monomers. Equivalent numbers of hydroniums to sulfonate groups were added to make the system neutral, and then the systems were doped with 0%, 1%, or 5% HPW nanoparticles. Three hydration levels corresponding to λ = 5, 9, 14 were then created for the pure and doped 3M ionomer systems.

The nine systems outlined above were subjected to all atomistic molecular dynamics

simulations using the LAMMPS code.[45] The systems were initially heated to 400 K and simulated for 5 ns in the iso-thermal iso-baric ensemble (NPT) to achieve mixing of the entangled polymer strands, water, hydroniums, and HPW when present. The initial NPT simulation was then followed by 5 ns of simulation in NPT at 300 K and 1 atm to cool the systems and to calculate the density. The above heat−cool cycle was repeated until the measured density was within 5% of the experimentally determined density. The resulting systems were then subjected to 20 ns of equilibration in the canonical ensemble (NVT) at 300 K followed by 20 ns production simulations conducted in the microcanonical ensemble (NVE).

The mobility (i.e., diffusion constants) of water was evaluated by the mean squared displacement (MSD):

$$D = \lim_{x \to \infty} \frac{1}{6t} \left\langle \left| r(t) - r(0) \right|^2 \right\rangle$$

where D is the diffusion coefficient, t is time, and r is the coordinates for the particle of interest.

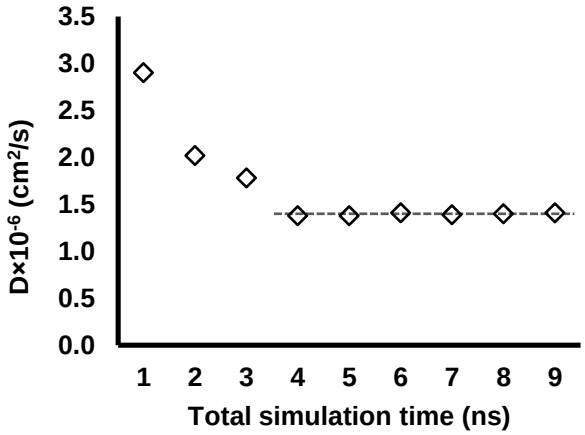

Figure 3.3 Diffusion coefficient as a function of time. This is generated using the water MSD data from 0%HPW-5λ.

A plot depicting the convergence of the diffusion coefficient for various simulation lengths is shown in Figure 3.3.

3.4 Result and Discussion

As the thermal history of ionomer treatment is known to affect the properties of the film, including morphology and proton transport, it should be noted that comparisons between this work and our previous study[17] may not be possible. Importantly, the films in this study were annealed at 180 °C, whereas in the previous study they were not.

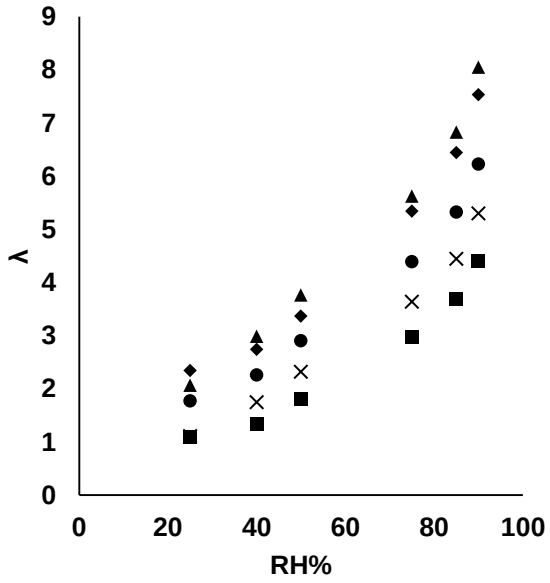

Figure 3.4 Water content at different RHs for (▲) undoped, (◆) 1% HPW, (×) 5% HPW, (●) 1% HSiW, and (■) 5% HSiW doped 825EW 3M ionomer

3.4.1 Water Uptake

The λ values measured for each film at six different RHs are shown in Figure 3.4. It is

found that λ increases to 8.05 at 90% RH for the undoped 825EW 3M ionomer and 7.54, 5.30, 6.23, and 4.40 for the 1% HPW, 5% HPW, 1% HSiW, and 5% HSiW doped films, respectively. It is found that the films swell with increasing RH and that the addition of HPAs at various levels makes the films less hydrophilic,[16] with the highest loadings of HSiW being the least hydrophilic. This observation can be attributed to the HPA particles competing with the sulfonic acid groups for the available water sites. Also, there is a strong hydrogen-bonding interaction between the sulfonic acid and the HPA particles.[16] This competition is most apparent at high hydration levels. Another possible cause could be due to morphological changes in the polymer brought on by the presence of HPAs; that is, the micro water conductive structures in the films are altered as a result of HPAs' interaction with the ionomer. The result of these interactions changes the electrostatic environment and therefore the solvent properties. It is noted that under dry conditions it was observed that the HPAs exist in the form of aggregates, as shown in the TEM images (Figure 3.5), which implies there are also more HPAs on the surface than in the bulk. From the DVS water sorption isotherms (Figure 3.6), we observed a phase change for the HPA doped films, as indicated by the reduction of mass upon the dissolution of HPA at 25% and 40% RH for 1% and 5% HPA doped films, respectively. This observation has implications for the observed diffusive properties of the system as it represents an inhomogeneous system and significantly different mass transport limitation than systems without mass reorganization. The phase change takes place at higher RH for lower doping level, which could also be a reflection of the size and abundance of the aggregates. We note that the water numbers we obtained through DVS could be an underestimation due to the well-known difficulty of making the samples completely dehydrated to obtain the dry weight of the films. Also, the DVS equilibration time is relatively short as compared to longer term studies over saturated salt solutions.[46]

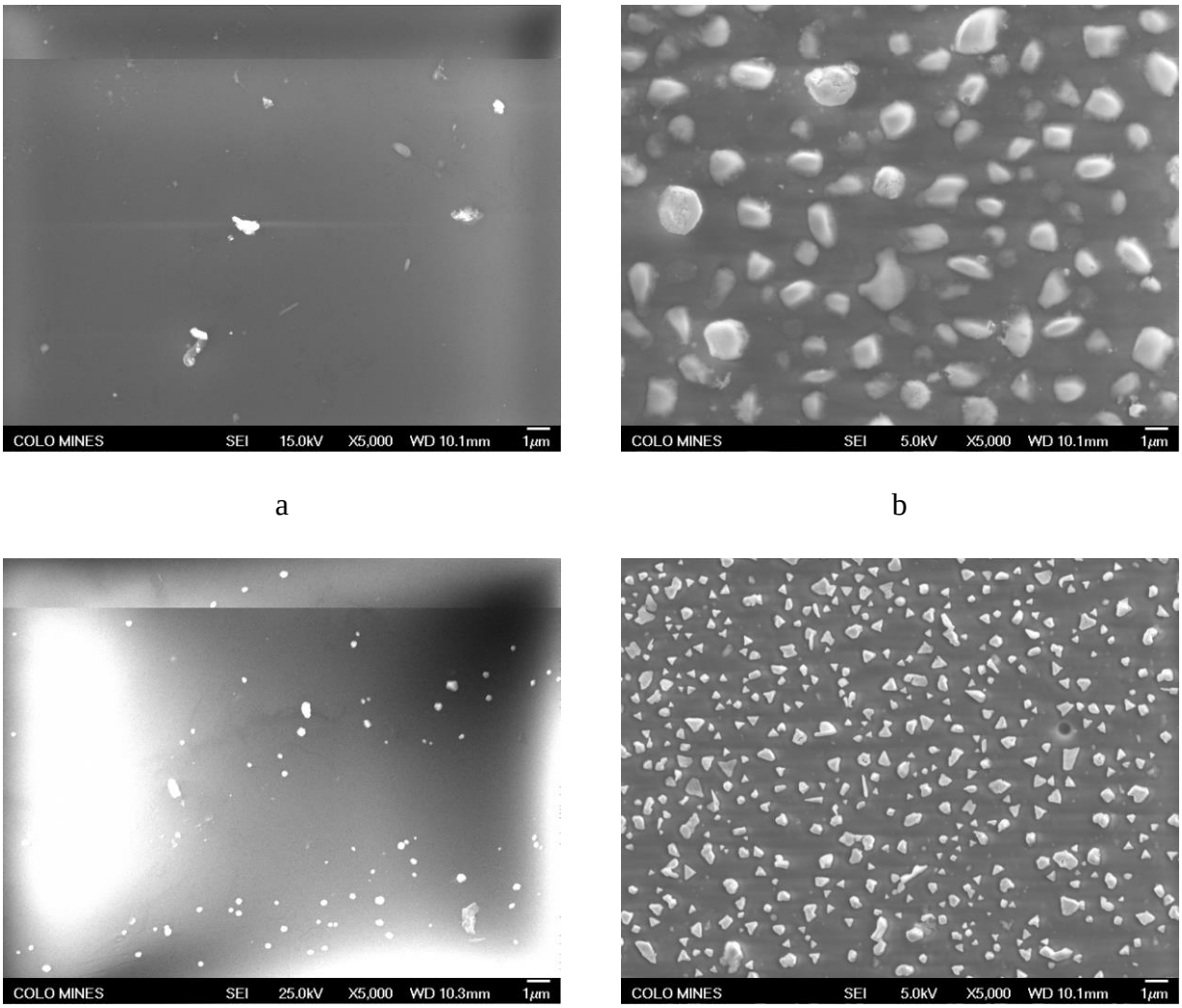

Figure 3.5 TEM image of doped films: a. 1%HSiW; b. 5%HSiW; c. 1%HPW; d. 5%HPW doped 825EW 3M ionomer.

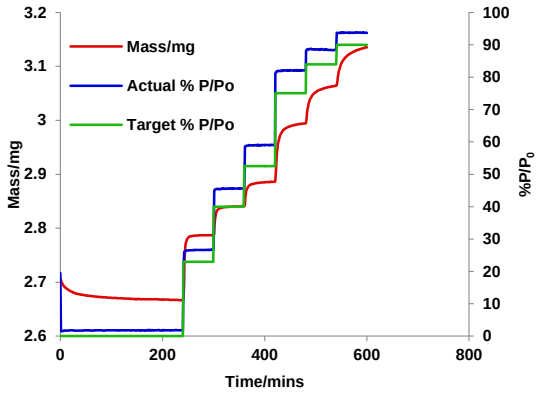

a

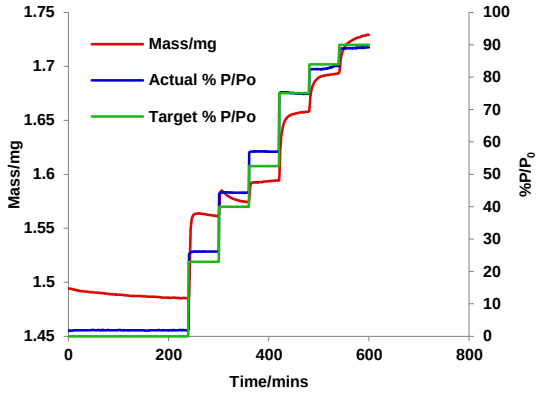

b

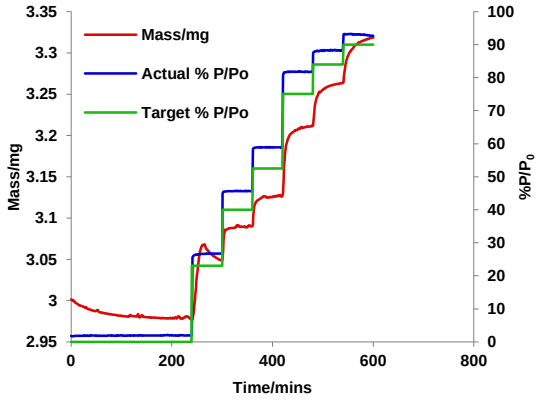

c

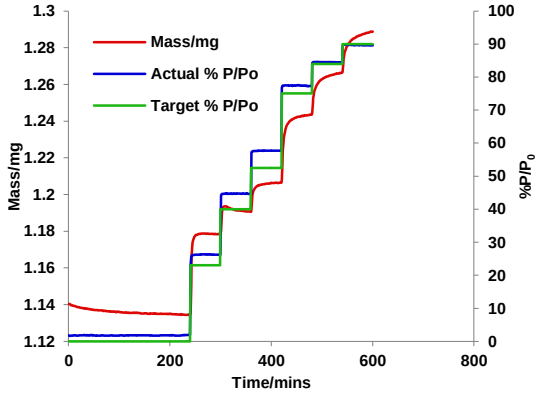

d

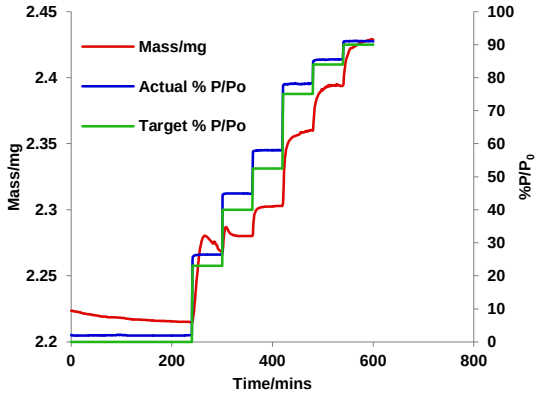

e

Figure 3.6 Water sorption isotherm at 300K: a. undoped, b. 1%HPW, c. 5%HPW, d. 1%HSiW, and e. 5%HSiW doped 825EW 3M ionomer.

3.4.2 ATR-FTIR

The IR spectra for both dry and hydrated films are presented in Figure 3.7. Four characteristic peaks[47] are obtained when the spectrum of pure ionomer film was subtracted from the 5% HPW doped film: heteroatom−oxygen, υ(P−O), at 1080 cm^{-1}, tungsten−terminal oxygen, υ(W=O), at 983 cm^{-1}, tungsten−corner shared oxygen, υ(W−Oc), at 889 cm^{-1}, and tungsten−edge shared oxygen, υ(W−Oe), at 810 cm^{-1} for the dried films, and 1075, 976, 887, and 809 cm^{-1}, respectively, for hydrated films. The υ(P−O) and υ(W=O) peaks shift to lower wavenumber as the films hydrate, reflecting the interaction between HPA, ionomer, and water, while the υ(W−Oc) and the υ(W−Oe) peaks show no significant shift. Because of the involvement of the ionomer, this interaction is different from the interaction observed between water and the pure HPA, as investigated by Zecchina et al., where the υ(P−O) shifts to higher frequency, and the υ(W=O) and υ(W−Oe) shift to lower frequency on hydration.[48] The peaks at dry conditions agree better with the characteristic peaks of HPW at solid states,[47] which is due to HPA aggregates at dry conditions and has less interaction with water and ionomer environment. Upon hydration, the HPA dissolves and disperses in the ionomer, causing further deviation from the solid states. For HSiW doped films, similar peaks are observed, but at lower wave numbers, indicating a stronger interaction between HPA, water, and acid group of ionomer (SO_3^-). The bands between 1550 and 1800 are associated with the bending OH mode. For the 5% HPW doped film, we observed a peak at 1688 cm^{-1}, which is the δ(OH) of neutral water and Eigen ions, and a peak at 1773 cm^{-1}, which is attributed to the δ(OH) of the Zundel cation ($H_5O_2^+$).[49] We observed these two peaks for all hydrated films. It was observed that doping of HPA shifted these peaks to lower wavenumbers. Interestingly, for the dry films, the Zundel ion δ(OH) band is absent in the spectrum of the undoped 825EW 3M ionmer. This could be due to small residual

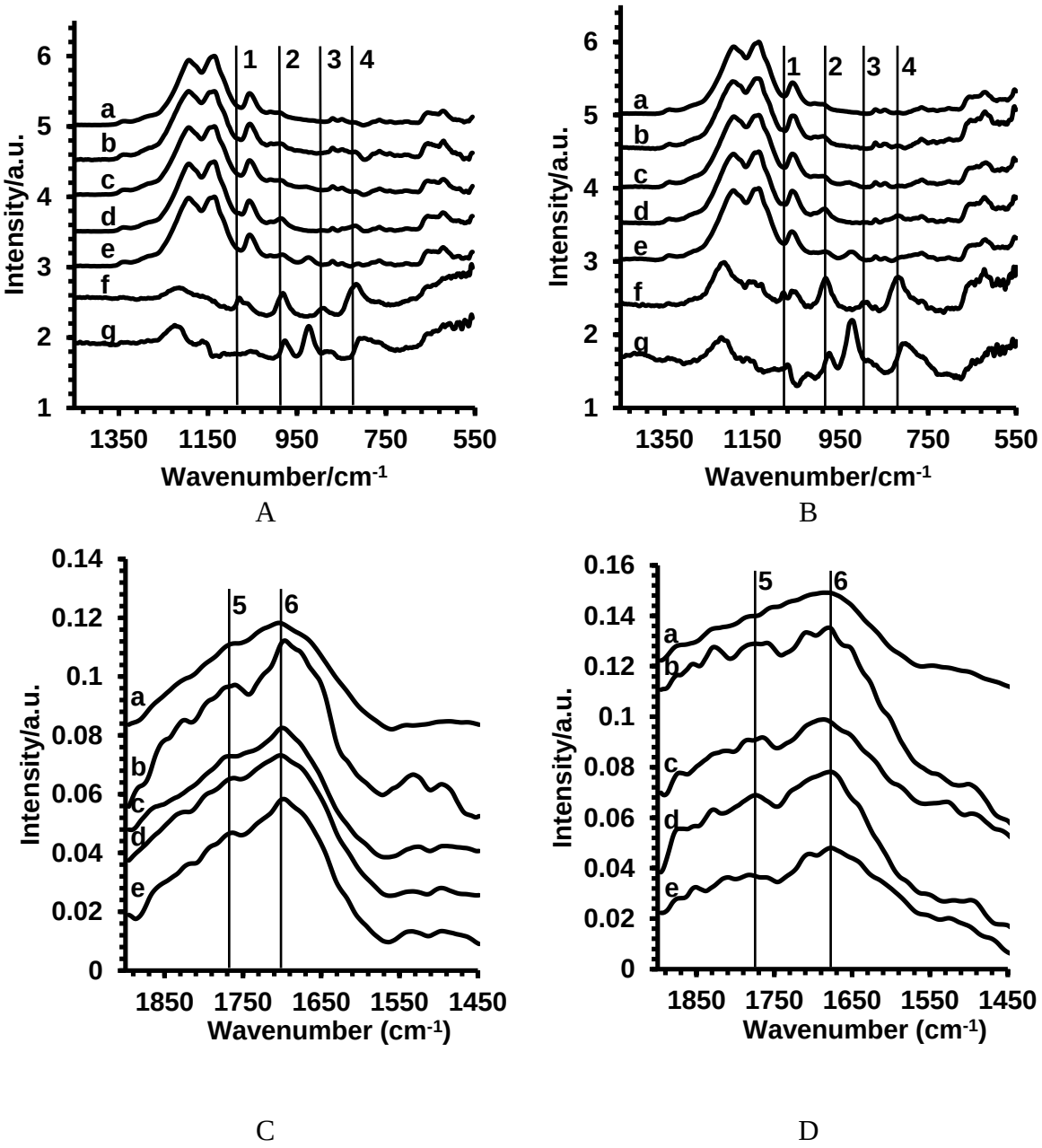

Figure 3.7 IR spectra for (a) undoped, (b) 1% HPW, (c) 1% HSiW, (d) 5% HPW, and (e) 5% HSiW doped 825EW 3M ionomer, (f) is the subtracted spectra (d−a) of 5% HPW doped 825EW 3M ionomer, and (g) is the subtracted spectra (e−a) of 5% HSiW doped 825EW 3M ionomer. Peak 1 is υ(X− O), 2 is υ(W=O), 3 is υ(W−Oc), 4 is υ(W−Oe), 5 is δ(OH), and 6 is υ(OH). (A) and (C) represent the maximum hydration, while (B) and (D) represent the minimum hydration.

amounts of water that remain after drying due to the hydrophilicity of the ionic domains. The residual water would enable the formation of $H_5O_2^+$, from the interaction with HPAs, and serve as a connection between HPA Keggin units through hydrogen bonding, while it is not the case for the pure ionomer films. Upon hydration, Zundel ions are likely to be formed in the hydrophilic domains of the ionomer. The presence of HPA could induce changes in morphology and the electrostatic environment, which could facilitate the formation and retention of Zundel ions under drier conditions. Zecchina et al. observed the δ(OH) of neutral water and Eigen ions at 1620 cm^{-1} and δ(OH) of the Zundel cation ($H_5O_2^+$) at 1720 cm^{-1} on the spectra of fully hydrated HPW solid. The peak at 1620 cm^{-1} disappears after short degassing at room temperature, indicating a loss of free water, and both peaks became no longer visible upon drying at elevated temperature.[48] We observed that the peaks around 1688 cm^{-1}, which is attributed to δ(OH) of neutral water and Eigen ions for all films, did not disappear, but became less apparent under dry conditions than under wet conditions. This observation could be attributed to the involvement of ionomer in the interaction and, again, the hydrophilicity of ionic domains in the ionomer.

3.4.3 Water Diffusion

The self-diffusion coefficient of water was measured by PGSE-NMR spectroscopy. The presence of HPAs in the ionomer is hypothesized to destabilize the morphological arrangement of the ionomeric system causing alterations to the mobility of water. From Figure 3.8, it is found that for all temperatures at the minimum humidity, HPA doped films have higher diffusion coefficients than the undoped 825EW 3M ionmer, and that the differences become larger as the temperature increases. However, at the maximum humidity, the diffusion coefficients generally

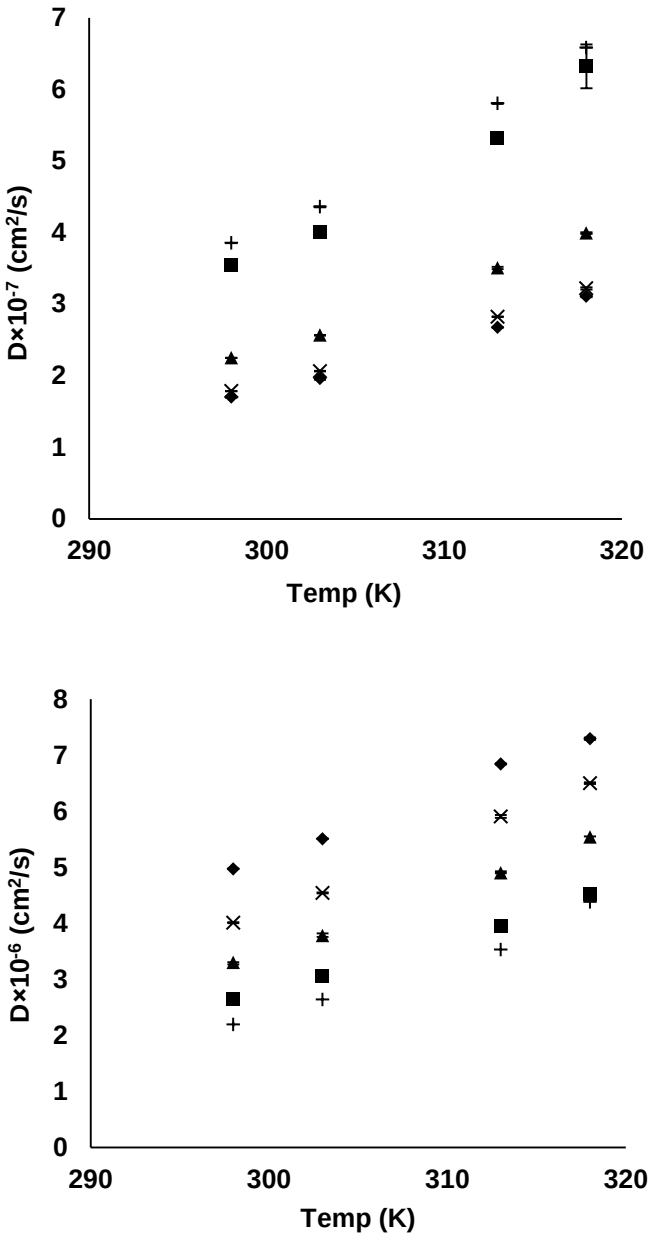

Figure 3.8 Water diffusion coefficient as measured by PGSE-NMR at different temperatures for (◆) undoped, (+) 1% HPW, (■) 5% HPW, (×) 1% HSiW, and (▲) 5% HSiW doped 825EW 3M ionomer. Minimum hydration (top) and maximum hydration (bottom).

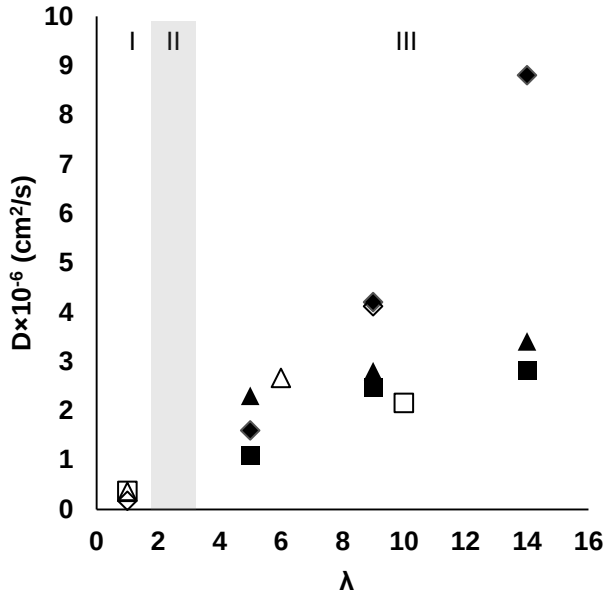

Figure 3.9 Water diffusion coefficient at different hydration levels for simulated values, (◆) undoped, (■) 1% HPW, and (▲) 5% HPW doped 825EW 3M ionomer; experimental values, (◇) undoped, (□) 1% HPW, and (△) 5% HPW doped 825EW 3M ionomer. HPA exists in aggregates in region I and dissolved state in region II. All of the λ for experimental data are obtained from extrapolation of the water sorption plot (Figure 3.3) to 100% RH (maximum hydration). λ is 1 for the minimum hydration.

decrease with doping of HPA (except for 1% HSiW). The HPA through favorable charge interactions stabilizes the hydroniums and retains water, thereby slowing the diffusion of water. A comparison of computed and experimental diffusion coefficient (standard errors are within10%) is shown in Figure 3.9 and is in excellent agreement at high hydration levels (corresponding to 100% RH). However, the simulation may only be suitable for the dispersed system, because HPAs exists in aggregates at low hydration levels (Figure 3.9, region I). Upon hydration, HPA will start to dissolve in the ionomer (Figure 3.9, region II), yielding good agreement between the simulation model and the actual experiment system. Because of the discrepancy between the model and experimental system at low hydration levels, we have only obtained the simulated diffusion coefficient for $\lambda \geq 5$.

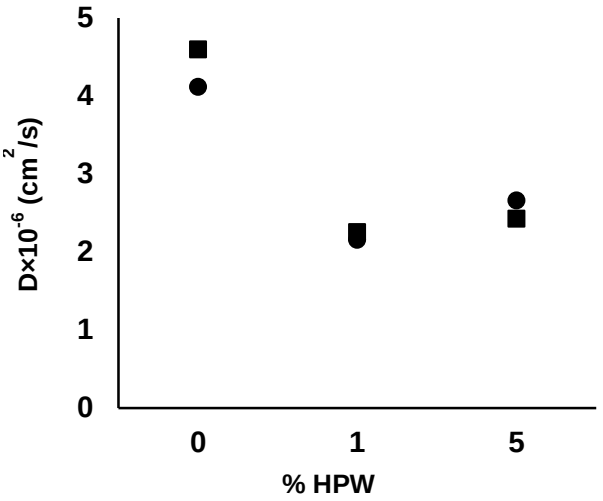

Figure 3.10 Diffusion coefficients of water at maximum humidity for 0%, 1%, and 5% HPW doped 825EW 3M ionomer: (●) experimental, (■) simulated.

The impact of HPW loading on the mobility of water is shown in Figure 3.10. It is found that from 0 to 1% HPW the diffusion decreases, a phenomenon observed in both experiment and simulation. It is hypothesized that for the 1% HPW system, the available hydroniums previously near the SO_3^- functional groups move toward the highly charged HPW nanoparticles (data not shown). This favorable charge−charge interaction results in a decrease in the diffusion coefficient upon addition of HPW to the 3M ionomer. However, increasing the amount of HPW from 1% to 5%, it is observed that the diffusion coefficients increase. The increase in diffusions from low to high amounts of HPW is due to the relatively high mobility of water in the adjacent solvation shell of HPW, while at low doping levels the HPWs are isolated from one another and therefore the diffusion restricted to that of the HPW in the ionomer, which is not the case at higher doping levels. Upon adding additional HPW, the solvation shells around the HPWs have a higher probability of merging, thereby creating an interconnected pathway through which the hydrated protons may travel. This in effect creates pathways for the proton and water to move along and results in the observed increase in the diffusion coefficients.

The self-diffusion coefficient of water was also recorded at different diffusion times at 25 °C, as shown in Figure 3.11. Films with different HPA loadings show the same extent of tortuous diffusion behavior under both maximum and minimum hydration, as we see from the diffusion time (Δ) dependence of the water diffusion coefficient. This indicates that water diffuses in a heterogeneous space and is affected by morphology and different water networks. This is expected, as it is already shown that PFSA or other types of ion exchange films form hydrophilic/hydrophobic phase separated morphology from numerous scattering and microscopy studies, with the size of the hydrophilic domains range from nanometer to micrometer meter levels, depending on hydration level and technique adopted.[6,50] This size discrepancy may result from the PFSA's hierarchical structure; that is, multiple structure levels may exist, with the smaller structures, when combined, forming the larger structures and the long-range order between these substructures. Generally, at short diffusion time, the diffusion coefficients decrease rapidly and then level off at a steady state. The steady state represents the condition where the waters are constricted by the ionomer environment and therefore feel all geometrical restrictions for the corresponding size range. Similar observations were made for PFSA films under both high and low hydration levels.[51,52] We observed that all films experience a larger restriction under minimum hydration than maximum hydration for the size scale concerned. The doping of HPAs also has some effect on the decay of diffusion coefficient, with the undoped 825EW 3M ionomer membrane exhibiting larger Δ dependence than the doped films, especially under maximum hydration, which indicates different pore structures for these films, as discussed below in more detail.

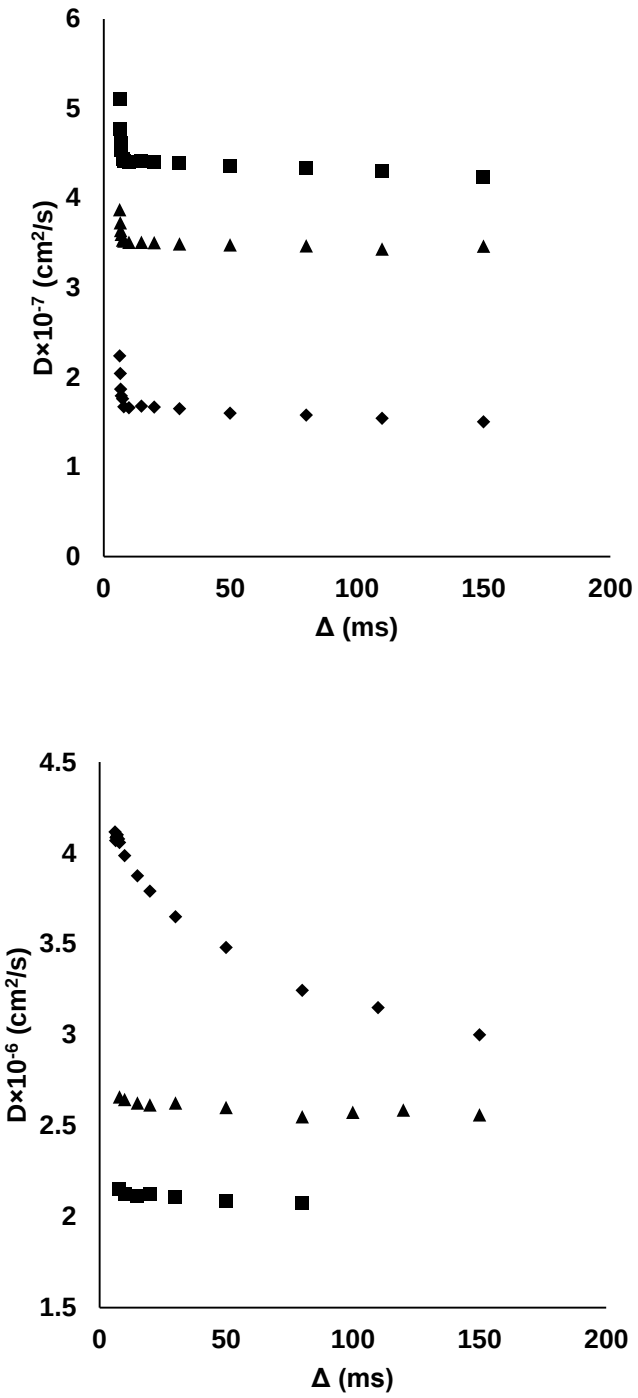

Figure 3.11 Diffusion coefficient at 25 °C and different diffusion times for (◆) undoped, (■) 1% HPW, and (▲) 5% HPW doped 825EW 3M ionomer. Minimum hydration (top) and maximum hydration (bottom).

Mitra et al.[53-56] have developed a theory to describe the transport behavior in porous medium: at short diffusion time Δ, the volume fraction of spins that feel the pore wall is given by $S/V(2D_0t)^{1/2}$. The following expression was obtained for short time diffusion:[53]

$$D(\Delta) = D_0\left[1 - \frac{4}{9\sqrt{\pi}}\frac{S}{V}\sqrt{D_0\Delta}\right]$$

where D_0 is the self-diffusion at time zero.

At very long diffusion intervals Δ, the spins feel the full geometrical restriction and only the tortuosity affects the diffusion. They obtained the following expression for the large Δ limit:[53]

$$D(\Delta) = D_0\alpha^{-1}$$

where α is the tortuosity.

From fitting our diffusion data at short time interval to $D(\Delta)-\Delta^{0.5}$ plots (figure 3.12), we obtained the S/V values (from the slope) for films with different HPA loadings and at both minimum and maximum hydration states, Table 3.1. The S/V value is an indication of the dimension of the domains in which the proton is able to move.[56] A larger S/V indicates a less homogeneous distributed domain. This is better presented as its reciprocal property R_c, which is the structure length scale. We noticed that the increase of hydration greatly improved the homogeneity of the hydrophilic domain (from a structure length of a few hundred nanometers to a few micrometers), due to the increased connectivity between cavities in this porous structure. Interestingly, the addition of HPW achieved the same effect under both hydrations, due to the HPW particle's strong interaction with the ionomer. The increased hydration also greatly decreased the tortuosity α, which is an indication of the connectivity between the hydrophilic water conductive channels. The addition of HPAs also decreases the tortuosity, except for 1%

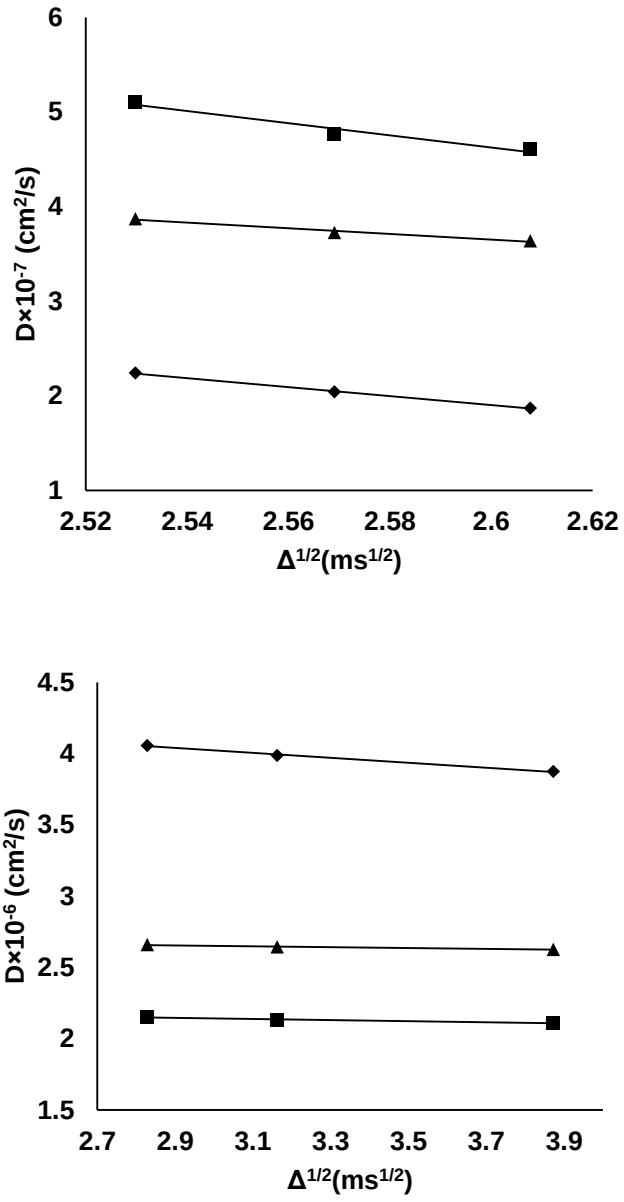

Figure 3.12 Fitting of diffusion coefficient to $D(\Delta)$-$\Delta^{0.5}$ plots: (♦) undoped, (■) 1%HPW, and (▲) 5%HPW doped 825EW 3M ionomer. Minimum hydration (Top) and Maximum hydration (Bottom).

HPW under minimum hydration. This could be due to the HPAs bridging the ionic clusters and making a more interconnected water wire; hence the HPA doped films generally show a less Δ dependence of water diffusion coefficient than do the undoped 825EW 3M ionomer films.

Table 3.1 Surface to volumes ratio (S/V) and R_c (V/S) for samples with different HPA loadings at different hydration conditions

SAMPLE	HYDRATION	S/V (μm^{-1})	R_c=V/S (μm)	Tortuosity α
Undoped	Minimum	3.52	0.28	9.07
1%HPW	Minimum	2.60	0.38	13.55
5%HPW	Minimum	3.09	0.32	3.32
Undoped	Maximum	0.23	4.43	1.40
1%HPW	Maximum	0.14	7.17	1.08
5%HPW	Maximum	0.09	11.70	1.08

3.4.4 Conductivity

From Figure 3.13, we can see that addition of HPA can yield higher conductivity except for 5% HPW at 80% RH and 1% wt HPW at 95% RH. The doping of 1% HPA decreases the diffusion coefficient of water at maximum RH (except for the 5% HPW), which is consistent with the reduced conductivity. This could be caused by the high intrinsic conductivity of HPA and the ability of HPA to increase the solvent acidity (i.e., decrease the pH) and accelerate the dissociation of protons.[57,58] In addition, it is believed that HPA doping increases the number of hydrogen-bonding networks and the proposed Grotthuss hopping, which are critical for efficient proton transport. This hypothesis is supported by a comparison (at 95% RH and 50 °C) of measured conductivity, σ_m, from EIS and calculated proton conductivity, σ_d, from the Nernst−Einstein equation:[59,60]

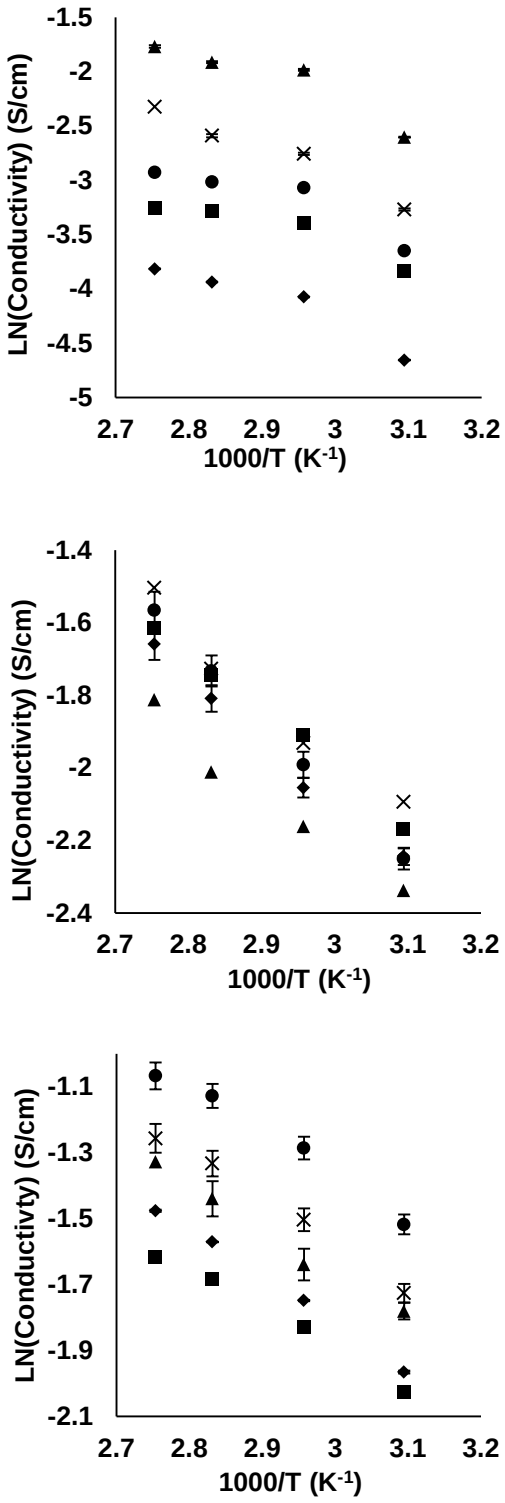

Figure 3.13 Arrhenius plots of proton conductivity versus temperature for (◆) undoped, (■) 1% HPW, (▲) 5% HPW, (×) 1% HSiW, and (●) 5% HSiW doped 825EW 3M ionomer. (top) 50% RH, (middle) 80% RH, and (bottom) 95% RH.

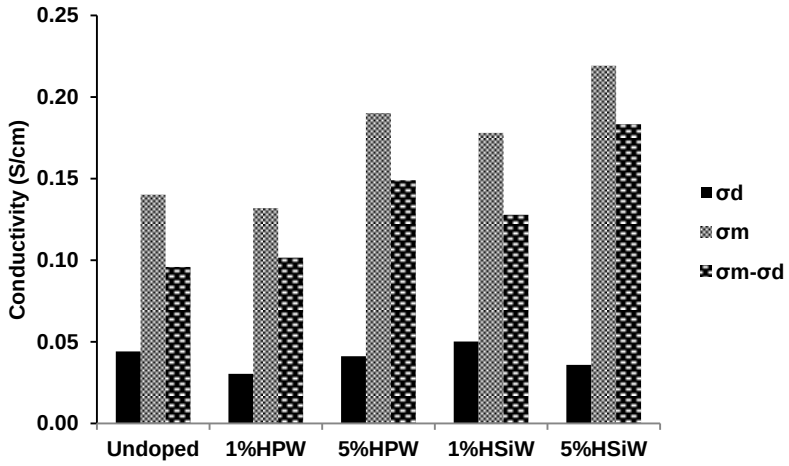

Figure 3.14 Conductivity at 95% RH and 50 °C: measured and calculated from Nernst−Einstein equation.

$$\sigma_d = \frac{e^2 n D}{k_B T}$$

where σ is the conductivity, e is the elementary electric charge, n is the number density of the charge carrier, D is the diffusion coefficient of charge carrier, k_B is the Boltzmann constant, and T is the absolute temperature. The number density of charge carrier n is obtained through the method described by Kawamura et al.[59] By assuming that hydroniums diffuse at the same rate as water, we used the diffusion coefficient of water measured through PGSE-NMR under maximum humidity to obtain σ_d.[59] The discrepancy ($\sigma_m - \sigma_d$) indicates the effect of proton transport through other mechanisms such as Grotthuss hopping. From Figure 3.14, σ_m is found to be generally higher than the σ_d. This discrepancy increases as the HPA doping level increases, with the 5% HSiW doped film generating the largest difference (σ_m-σ_d) of 0.18 S/cm. This shows us (i) the real transport process of the excess proton takes place much faster than water diffusion (i.e., facilitated by Grotthuss mechanism), especially under higher hydration states;[17,61] (ii) the addition of HPA can enhance proton hopping by facilitating the formation of hydrogen-bonding

network; and (iii) HPA particles are mobile at high hydration level, which could also contribute to the higher rate of proton transfer.

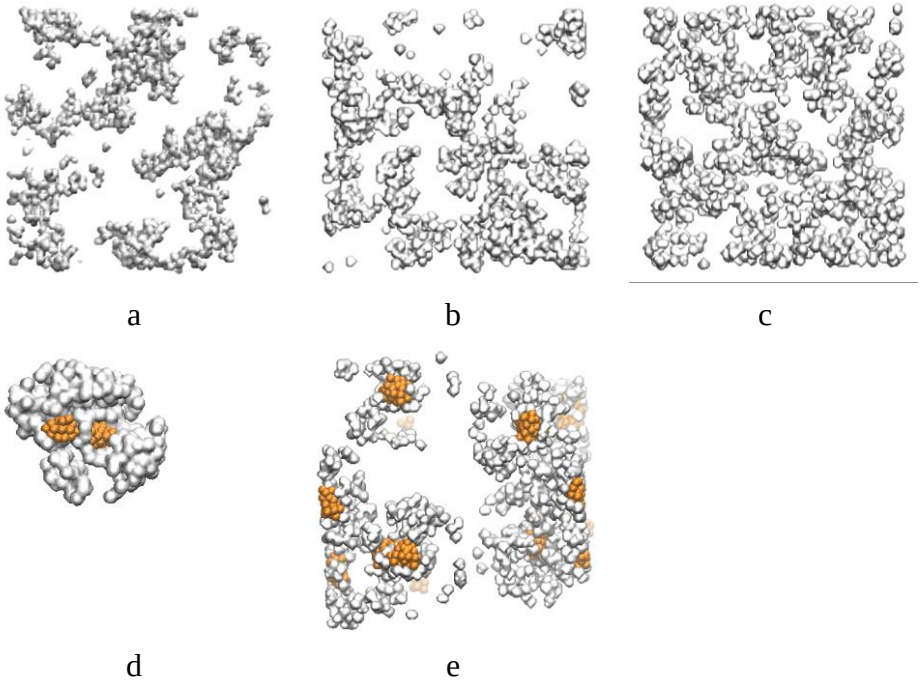

Figure 3.15 Water morphology from simulations of various HPW loadings, (a) undoped, (b) 1% HPW, and (c) 5% HPW doped 825EW 3M ionomer; and waters around HPW nanoparticles up to 20 Å from particle center, (d) 1% HPW and (e) 5% HPW doped 825EW 3M ionomer. Isosurface images at 40% are generated using a volmap plug-in in Visual Molecular Dynamics visualization software.[22]

3.4.5 Effect of Morphology on Proton Transport

From both simulation (Figure 3.15) and experiment,[62] we observed the effect of HPA addition to the morphology of films in terms of water/hydronium distributions (This work is presented in Appendix A). The addition of HPA tends to redistribute the hydrophilic domains to a more interconnected morphology, with the water molecules forming a shell around the HPAs. As we increased the HPA loadings, the hydrophilic domains become more interconnected as

shown in Figure 3.15, provided that HPAs are distributed evenly. Thus, as a result of HPA addition, while the diffusion coefficient of water is not necessarily increased, the proton conductivity of films is greatly improved especially under drier conditions, as a result of shorter transport pathways and less overall resistance.

3.5 Conclusions

HPA doping generally makes the ionomer component of the films less hydrated by hindering the water uptake to the sulfonic acid groups in favor of solvating the HPA particle. HPAs have strong interaction with the ionomer and H_2O, revealed by shifts in the IR bands to lower energy upon HPA addition and hydration. The PFSA films show tortuous proton diffusion behavior at both minimum and maximum hydration levels, and the hydrophilic domain of the films becomes more homogeneous upon HPA addition and hydration. The self-diffusion coefficient of water was found to decrease upon addition of HPA at the maximum hydration level in excellent agreement with computation. The model at low HPA loadings reveals the decreased diffusion coefficient was due to a higher probability of water residing near the HPA as opposed to the sulfonic acid groups, which reduced the mobility of the water. The conductivity of HPA doped film generally improved at both wet and dry conditions, due to the formation of water clusters round HPA particles that have an increased probability of forming solvent bridges resulting in a more interconnected hydrogen-bonding network. At high RH, it was observed that the proton conductivity increased while the water diffusion coefficient decreased upon HPA doping. This unexpected behavior implies the addition of HPA particles enhances the Grotthuss hoping mechanism, and that this mechanism is believed to dominate over the vehicular transport at this hydration level. This is further confirmed by the mismatch between conductivity values

and those calculated from the Nernst−Einstein equation using the self-diffusion coefficient of water in the system. The discrepancy generally increases as more HPA is added to the system, again indicating an acceleration of proton conduction through the Grotthuss mechanism.

3.6 Acknowledgements

This research was funded by the DOE, EERE Cooperative Agreement No. DE-FG36-07G017006, and in part by the NSF through the Renewable energy MRSEC under grant DMR-0820518. We want to thank 3M for supplying ionomer samples and technical support in addition to the Colorado School of Mines Campus Computing, Communications, and Information Technologies for the computational resources.

3.7 References

(1) Herring, A. M. *Polymer Reviews* **2006**, *46*, 245.

(2) Haugen, G. M.; Meng, F. Q.; Aieta, N. V.; Horan, J. L.; Kuo, M. C.; Frey, M. H.; Hamrock, S. J.; Herring, A. M. *Electrochemical and Solid State Letters* **2007**, *10*, B51.

(3) Wu, D. S.; Paddison, S. J.; Elliott, J. A. *Energy & Environmental Science* **2008**, *1*, 284.

(4) Tant, M. R.; Darst, K. P.; Lee, K. D.; Martin, C. W. *Acs Symposium Series* **1989**, *395*, 370.

(5) Whiteley, L. D.; Martin, C. R. *Journal of Physical Chemistry* **1989**, *93*, 4650.

(6) Liu, Y.; Horan, J. L.; Schlichting, G. J.; Caire, B. R.; Liberatore, M. W.; Hamrock, S. J.; Haugen, G. M.; Yandrasits, M. A.; Seifert, S.; Herring, A. M. *Macromolecules* **2012**, *45*, 7495.

(7) Mauritz, K. A.; Moore, R. B. *Chemical Reviews* **2004**, *104*, 4535.

(8) Kreuer, K. D. *Journal of Membrane Science* **2001**, *185*, 29.

(9) Kreuer, K. D.; Rabenau, A.; Weppner, W. *Angewandte Chemie-International Edition in English* **1982**, *21*, 208.

(10) Kreuer, K. D. *Chemistry of Materials* **1996**, *8*, 610.

(11) Glasstone, S.; Laidler, K. J.; Eyring, H.; McGraw-Hill: New York, **1941**, p 550

(12) Sagnella, D. E.; Laasonen, K.; Klein, M. L. *Biophys J* **1996**, *71*, 1172.

(13) Zhang, J. L.; Xie, Z.; Zhang, J. J.; Tanga, Y. H.; Song, C. J.; Navessin, T.; Shi, Z. Q.; Song, D. T.; Wang, H. J.; Wilkinson, D. P.; Liu, Z. S.; Holdcroft, S. *J Power Sources* **2006**, *160*, 872.

(14) Yang, C.; Costamagna, P.; Srinivasan, S.; Benziger, J.; Bocarsly, A. B. *Journal of Power Sources* **2001**, *103*, 1.

(15) Ramani, V.; Kunz, H. R.; Fenton, J. M. *Journal of Membrane Science* **2004**, *232*, 31.

(16) Kim, Y. S.; Wang, F.; Hickner, M.; Zawodzinski, T. A.; McGrath, J. E. *J Membrane Sci* **2003**, *212*, 263.

(17) Meng, F. Q.; Aieta, N. V.; Dec, S. F.; Horan, J. L.; Williamson, D.; Frey, M. H.; Pham, P.; Turner, J. A.; Yandrasits, M. A.; Hamrock, S. J.; Herring, A. M. *Electrochim Acta* **2007**, *53*, 1372.

(18) Vernon, D. R.; Meng, F. Q.; Dec, S. F.; Williamson, D. L.; Turner, J. A.; Herring, A. M. *Journal of Power Sources* **2005**, *139*, 141.

(19) Kozhevnikov, I. V.; Sinnema, A.; Vanbekkum, H. *Catal Lett* **1995**, *34*, 213.

(20) Chikin, A. I.; Chernyak, A. V.; Jin, Z.; Naumova, Y. S.; Ukshe, A. E.; Smirnova, N. V.; Volkov, V. I.; Dobrovolsky, Y. A. *J Solid State Electr* **2012**, *16*, 2767.

(21) Malers, J. L.; Sweikart, M. A.; Horan, J. L.; Turner, J. A.; Herring, A. M. *Journal of Power Sources* **2007**, *172*, 83.

(22) Humphrey, W.; Dalke, A.; Schulten, K. *J Mol Graph Model* **1996**, *14*, 33.

(23) Tazi, B.; Savadogo, O. *J New Mat Electr Sys* **2001**, *4*, 187.

(24) Malhotra, S.; Datta, R. *Journal of the Electrochemical Society* **1997**, *144*, L23.

(25) Ramani, V.; Kunz, H. R.; Fenton, J. M. *Electrochim Acta* **2005**, *50*, 1181.

(26) Ramani, V.; Kunz, H. R.; Fenton, J. M. *Journal of Membrane Science* **2005**, *266*, 110.

(27) Urata, S.; Irisawa, J.; Takada, A.; Shinoda, W.; Tsuzuki, S.; Mikami, M. *Journal of Physical Chemistry B* **2005**, *109*, 4269.

(28) Spohr, E.; Commer, P.; Kornyshev, A. A. *Journal of Physical Chemistry B* **2002**, *106*, 10560.

(29) Petersen, M. K.; Voth, G. A. *Journal of Physical Chemistry B* **2006**, *110*, 18594.

(30) Jang, S. S.; Molinero, V.; Cagin, T.; Goddard, W. A. *Journal of Physical Chemistry B* **2004**, *108*, 3149.

(31) Paddison, S. J.; Elliott, J. A. *Journal of Physical Chemistry A* **2005**, *109*, 7583.

(32) Devanathan, R.; Dupuis, M. *Phys Chem Chem Phys* **2012**, *14*, 11281.

(33) Venkatnathan, A.; Devanathan, R.; Dupuis, M. *Journal of Physical Chemistry B* **2007**, *111*, 7234.

(34) Kreuer, K. D.; Paddison, S. J.; Spohr, E.; Schuster, M. *Chemical Reviews* **2004**, *104*, 4637.

(35) Tse, Y. L. S.; Herring, A. M.; Kim, K.; Voth, G. A. *J Phys Chem C* **2013**, *117*, 8079.

(36) Weber, A. Z.; Newman, J. *J Electrochem Soc* **2003**, *150*, A1008.

(37) Barbir, F.; Gorgun, H.; Wang, X. *Journal of Power Sources* **2005**, *141*, 96.

(38) Dai, W.; Wang, H. J.; Yuan, X. Z.; Martin, J. J.; Yang, D. J.; Qiao, J. L.; Ma, J. X. *Int J Hydrogen Energ* **2009**, *34*, 9461.

(39) Janarthanan, R.; Horan, J. L.; Caire, B. R.; Ziegler, Z. C.; Yang, Y.; Zuo, X.; Liberatore, M. W.; Hibbs, M. R.; Herring, A. M. *Journal of Polymer Science Part B: Polymer Physics* **2012**.

(40) Price, W. S. *NMR studies of translational motion: principles and applications*; Cambridge University Press, 2009.

(41) Mayo, S. L.; Olafson, B. D.; Goddard, W. A. *Journal of Physical Chemistry* **1990**, *94*, 8897.

(42) Brodbeck, R.; Tonsing, T.; Andrae, D.; Volkmer, D. *Journal of Physical Chemistry B* **2008**, *112*, 5153.

(43) Levitt, M.; Hirshberg, M.; Sharon, R.; Laidig, K. E.; Daggett, V. *Journal of Physical Chemistry B* **1997**, *101*, 5051.

(44) Knox, C. K.; Voth, G. A. *Journal of Physical Chemistry B* **2010**, *114*, 3205.

(45) Plimpton, S. *J Comput Phys* **1995**, *117*, 1.

(46) Maalouf, M.; Pyle, B.; Sun, C.-N.; Wu, D.; Paddison, S. J.; Schaberg, M.; Emery, M.; Lochhaas, K. H.; Hamrock, S. J.; Ghassemi, H. *ECS Transactions* **2009**, *25*, 1473.

(47) Rocchicciolideltcheff, C.; Thouvenot, R.; Fouassier, M. *Inorg Chem* **1982**, *21*, 30.

(48) Paze, C.; Bordiga, S.; Zecchina, A. *Langmuir* **2000**, *16*, 8139.

(49) Korzeniewski, C.; Snow, D. E.; Basnayake, R. *Applied Spectroscopy* **2006**, *60*, 599.

(50) Maes, A. M.; Pandey, T. P.; Vandiver, M. A.; Lundquist, L. K.; Yang, Y.; Horan, J. L.; Krosovsky, A.; Liberatore, M. W.; Seifert, S.; Herring, A. M. *Electrochim Acta* **2013**.

(51) Park, J. K.; Li, J.; Divoux, G. M.; Madsen, L. A.; Moore, R. B. *Macromolecules* **2011**, *44*, 5701.

(52) Roy, A.; Hickner, M. A.; Yu, X.; Li, Y. X.; Glass, T. E.; McGrath, J. E. *Journal of Polymer Science Part B-Polymer Physics* **2006**, *44*, 2226.

(53) Mitra, P. P.; Sen, P. N.; Schwartz, L. M.; Ledoussal, P. *Phys Rev Lett* **1992**, *68*, 3555.

(54) Latour, L. L.; Mitra, P. P.; Kleinberg, R. L.; Sotak, C. H. *J Magn Reson Ser A* **1993**, *101*, 342.

(55) Sen, P. N. *Concept Magn Reson A* **2004**, *23A*, 1.

(56) Rollet, A. L.; Simonin, J. P.; Turq, P.; Gebel, G.; Kahn, R.; Vandais, A.; Noel, J. P.; Malveau, C.; Canet, D. *Journal of Physical Chemistry B* **2001**, *105*, 4503.

(57) Choi, J. K.; Lee, D. K.; Kim, Y. W.; Min, B. R.; Kim, J. H. *Journal of Polymer Science Part B-Polymer Physics* **2008**, *46*, 691.

(58) Wang, Z.; Ni, H. Z.; Zhao, C. J.; Li, X. F.; Fu, T. Z.; Na, H. *Journal of Polymer Science Part B-Polymer Physics* **2006**, *44*, 1967.

(59) Ochi, S.; Kamishima, O.; Mizusaki, J.; Kawamura, J. *Solid State Ionics* **2009**, *180*, 580.

(60) Choi, P.; Jalani, N. H.; Datta, R. *Journal of the Electrochemical Society* **2005**, *152*, E123.

(61) Zawodzinski, T. A.; Gottesfeld, S.; Shoichet, S.; Mccarthy, T. J. *J Appl Electrochem* **1993**, *23*, 86.

(62) Sambasivarao, S. V. L., Y.; Horan, J.L.; Yang, Y.; Hamrock, S.J.; Haugen, G.M.; Maupin, C.M.; Herring, A.M. .

CHAPTER 4 A SMALL ANGLE X-RAY SCATTERING STUDY OF THE MORPHOLOGY OF A PERFLUORINATED PROTON EXCHANGE MEMBRANE WITH VARIOUS SIDE-CHAIN CHEMISTRIES

Yuan Liu,[†] James L. Horan,[†] Gregory J. Schlichting,[†] Benjamin R. Caire,[†] Steven J. Hamrock,[§] Michael A. Yandrasits,[§] Gregory M. Haugen,[§] Soenke Seifert[‡] and Andrew M. Herring[*, †]

4.1 Abstract

Perfluorinated proton exchange membranes (PEMs) with different side-chain chemistries were studied with respect to their morphological change upon water uptake. Information about the size and shape of the phase-separated nano-structures are obtained from a numerical modeling of the SAXS data. The radius of gyration of these structures are found to range from 5.8 to 16.5Å for the ionic clusters and from 24.8 to 65.7Å for crystalline structures formed by the backbone, depending on the chemical structure of the side chain and the hydration level. The functional group chemistry of the side-chain has a large effect on chain mobility and hydrophilicity, and consequently affects the kinetics of water sorption, crystallization of the perfluorinated backbone and the formation of the ionic clusters. The two structural levels

[†]Department of Chemical and Biological Engineering, Colorado School of Mines, Golden, Colorado 80401, United States

[§]3M Fuel Cell Components Program, 3M Company, St. Paul, Minnesota 55144, United States

[‡]X-ray Science Division, Argonne National Laboratory, Argonne, Illinois 60439, United States

[*]Corresponding Author

identified here, show significant differences in the reversibility of swelling behavior, with the ionic clusters showing reversible swelling, while that of the crystalline region is irreversible.

4.2 Introduction

Perfluorinated proton exchange membranes (PEMs) show great potential in meeting the targets of high proton conductivity, adequate oxidative stability, and low cost for an operating PEM fuel cell.[1-3] Several such materials have been developed, such as Nafion™ by Dupont, the 3M ionomer by 3M Corp., [4,5] and a short side-chain ionomer, Aquivion™, currently by Solvay Solexis. [6,7] These perfluorinated sulfonic acid polymer (PFSA) films all contain a hydrophobic polytetrafluoroethylene (PTFE) backbone and a hydrophilic side-chain, with a sulfonic acid group attached at the end. Upon hydration, protons dissociate from the sulfonic group and could be transported through the PEM via a combination of the vehicular[8,9] and Grotthus mechanisms.[10,11] The structure of PFSA, *i.e.,* the equivalent weight (EW)[12] and the chemistry of the side chain has a large effect on the transport and mechanical properties of PFSA. Since the side-chain provides ion exchange sites, more side chains, *i.e.,* lower equivalent (EW) is required to achieve practical levels of proton conductivity. However, because of the dependence on the PTFE backbone to provide mechanical strength to the membrane,[13,14] low EW films tend to swell and dissolve in the presence of excessive water due to the absence of regions with crystalline structure. To make films mechanically stable and at the same time have an acceptable ion conductivity, films will have to be fabricated with sufficiently high crystallinity, and also capable of providing sufficient ion exchange sites for proton transfer. One important way to achieve this objective is through attaching more than one protogenic group to the side chain of a PEM with a mechanically robust backbone.

It is possible that ionomers with different chemical structures will result in different morphology, which will determine the physical and chemical properties of the films. Although a hydrophilic/hydrophobic phase separated morphology is widely accepted, detailed morphological description of the shape, size and arrangement of both domains under different hydration levels is highly desired for the purpose of understanding the membrane performance. Gebel suggests that the morphology of a PFSA ionomer changes with different water contents.[15] The system undergoes a transformation from polymer in solvent to solvent in polymer or *vice versa*, and that the shape of different structural levels will also vary accordingly.[15] Several simulation works conducted by Paddison *et al*. also show the effect of side chain length, inter side-chain distances and side chain chemistry on the resulting membrane's morphology, water uptake, and ion transport characteristics.[5,16,17]

Small angle X-ray scattering (SAXS) using synchrotron radiation is one of the most useful characterization techniques to obtain in-depth morphological information of PFSA membranes under different thermal and hydration conditions. A typical SAXS image [18] and a SAXS pattern of the 3M PFSA ioniomer[19] is available from our previous works. Due to the inhomogeneous electron density between structures at different levels and their backgrounds,[20,21] the SAXS pattern typically possess 3 structural levels. The peak in the high q region is ionomer peak, which originates from the constructive scattering of the ionic clusters. The upturn in low q region is matrix knee, and arises from the scattering by the crystalline domain.[22] The ultra-small angle upturn, which resides in the very low q region, is attributed to the long-range inhomogeneity of the ionic domains.[21-24]

In this paper, extensive SAXS investigation were performed on perfluorinated PEMs with various side-chain structures, which were provided by 3M Company. We investigated the

morphological changes at different hydration levels from 25%RH to 95%RH and various morphological and water uptake behavior of films arising from differences in the EW, side-chain length, functional group, symmetry and substitution group.

4.3 Experimental Section

Experimental methods and data processing are presented in this section. Experimental materials are also described below.

4.3.1 Materials

Perfluorinated proton exchange membranes with different chemical structures were supplied by 3M and coded as SC1 to SC6 (see table 4.1). Their chemical structures, side chains and EW backbone that they are shown in scheme 4.1 and table 4.1.[25]

4.3.2 SAXS Measurement

SAXS data were obtained at beamline 12ID C-D at the Advanced Photon Source (APS) at Argonne National Laboratory, Argonne, IL using X-rays of 18keV. The diagram and detailed description of the experimental setup were presented in our previous work.[19] Steady state SAXS measurement of the humidification experiment at 80 °C, evaluated a cycle of RH's consisting of 75%, 50%, 25%, 15%, 25%, 50%, 75% and 95% were was performed on the 3M films: the oven was first set to 75%RH and 3 SAXS patterns recorded on the films and 1 pattern recorded for the Kapton™ background, then the oven was set to 50%RH, 3 patterns were recorded on the films and on the Kapton™ blank. The same steps were performed according to the step described

Table 4.1 Code of 3M Side-Chain Series Ionomer Films

	SC1	SC2	SC3	SC4	SC5	SC6
Backbone EW	1000	812	812	644	733	583
Polymer name	Ortho bis	PFIA	Ortho bis	Phenyl imide	Meta bis	Penta Flouride

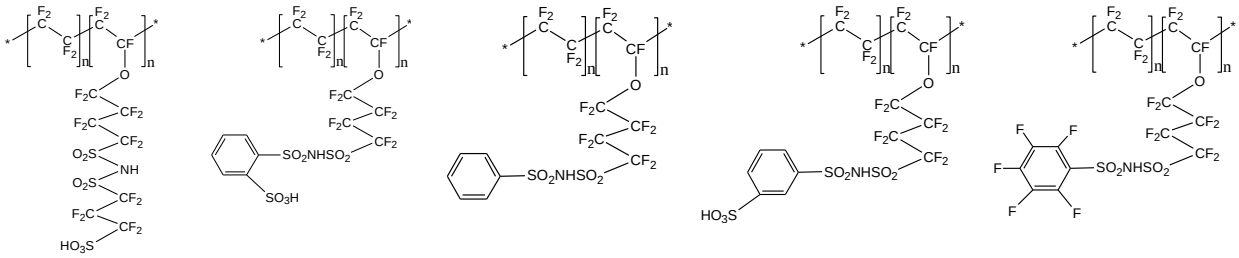

a b c d e

Scheme 4.1 Side-Chain Structures of 3M Side-Chain Series Ionomer Films: a. PFIA; b. Ortho bis; c. Phenyl imide; d. Meta bis; e. Penta fluoride.

above. During the SAXS measurements, the q range was adjusted according to different samples by adjusting the camera length.

4.3.3 DVS Measurement

Dynamic vapor sorption measurements were performed on the 3M side chain series (SC2, SC4 and SC6) membranes with a DVS instrument (DVS Advantage, SMS Inc.). These experiments were carried out with a corresponding environmental control to the SAXS experiments Water sorption isotherms were obtained for 3M ionomer films with various side-chain structures. Values of water uptake (Water Uptake (%) $= \frac{W_{wet}-W_{dry}}{W_{dry}} \times 100\%$) for the different RHs were determined gravimetrically.

4.4 Data Processing

In this work, we use the Irena macros package for Igor Pro for the unified fit model[26] to analyze the SAXS data. A representative fit is shown in our previous work.[18,19] Full details of the mathematics involved in the unified fit are also given in the supplemental information of our previous work.[19] Through these fits, quantitative information such as radius of gyration (R_g), and power law slope [27,28] were obtained for the different structural levels observed.

4.5 Results and Discussion

The high energy (18kev) of the APS X-rays has the potential to allow us to collect SAXS images in a very short time. This enables the study of morphological changes in polymer structures in-situ not accessible via conventional laboratory x-ray sources.

4.5.1 Effect of Hydration

From the SAXS curves on Figure 4.1, we can see that for all of these films, the SAXS pattern exhibits two structural levels, i.e., one ionomer peak and one crystalline knee/peak within the q range here. Upon water uptake, the curves move to higher intensity and both of these peaks/knees shift to a lower q region, indicating the increase of D-spacing d which defined as $d=2\pi/q$, as a result of swelling of the clusters and the filling out of water conductive channels by water,[29,30] as shown in table 4.2. From a unified fit model, we obtained quantitative information of size variation at different RHs for films with different chemical structures. From figure 4.2, we observed that the sizes of the first structural level, i.e., the ionic cluster domain, increase for all films with different chemical structures, ranging from 5.8 to 16.5Å for ionic clusters and 24.8 to 65.7Å for crystalline structures. This is well expected since it is widely accepted that the ionic

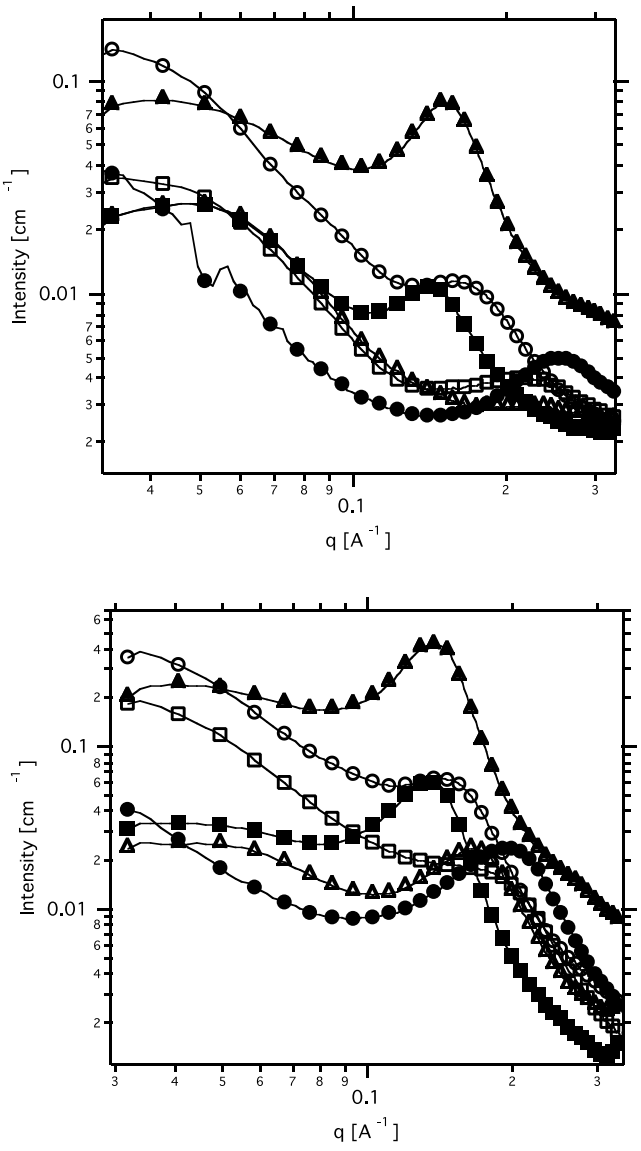

Figure 4.1 SAXS patterns of 3M side-chain series: at 25%RH (top), and at 95%RH (bottom). ○ SC1 1000EW Ortho bis; ▲ SC2 812EW PFIA; □ SC3 812EW Ortho bis; ● SC4 644EW Phenyl imide; ■ SC5 733EW Meta bis; ∆ SC6 583EW Penta Flouride

domain will swell and form aggregates with an increase of water content.[31,32] Interestingly, the size of the second structural level, which is the crystal domain, also increases in the humidification process, except for the phenyl imide, SC4. This is probably due to the plasticizing effect of water to the amorphous region of the ionomer, and makes the polymer chains mobile enough to crystallize.[33-35] This effect is the most obvious in the case of SC5 and SC3, which all have SO_3 groups attached to phenyl rings. This structure may be attributable to the easier recrystallization upon hydration, due to their higher hydrophilicity compared to SC4 but lack of flexibility compared to the PFIA, SC2. In the case of SC4, where the size of the crystalline structure shows no significant change, one reason for this should be due to its well phase separated morphology from a hydrophobic crystalline region. Taking its chemical structure into consideration, we can see that there is only one imide group on its side-chain, making it more hydrophobic compared to other ionomers, which have more than one water sorption functional group. The symmetrical phenyl group may also contribute to its relatively more hydrophobic nature of its crystalline domains.

Table 4.2 Ionic level D-spacing of different samples at low (25%) RH and high (95%) RH

Sample	25%RH Q ($Å^{-1}$)	95%RH Q ($Å^{-1}$)	25%RH D-spacing (Å)	95%RH D-spacing (Å)
SC1	0.16	0.14	39.3	44.9
SC2	0.15	0.14	41.9	44.9
SC3	0.22	0.17	28.6	36.9
SC4	0.26	N/A	24.2	N/A
SC5	0.14	0.13	44.9	48.3
SC6	0.23	0.17	27.3	37.0
3M825EW	0.20	0.16	32.1	38.7

*Values of 3M PFSA (3M825EW) are extracted from our previous work.[19]

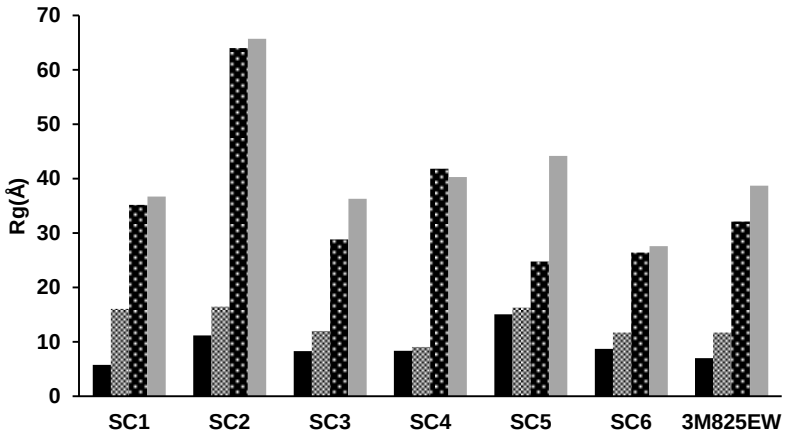

Figure 4.2 Unified fit results: sizes of ionic domain L1 and crystalline domain L2 for 3M SC series at different RHs: ■ L1 25%RH; ▩ L1 95%RH; ◘ L2 25%RH; ■ L2 95%RH. Values for 3M PFSA (3M825EW) are extracted from our previous work.[19]

4.5.2 Reversibility of Swelling

Figure 4.3 is the comparison of the domain size of both crystalline and ionic structures with the drying process (A) and the humidification (B) at the same RH. We can see from the figures that for the ionic domain, the swelling is quite reversible, especially for SC2, SC3 and SC5. Some of our water sorption isotherms of PFSA films (not shown) also reveal the reversibility of water uptake, which are in agreement with our SAXS fit results. For the second structural level, i.e., the hydrophobic crystalline domain, for films under 25%RH, the size variation is not significant, probably due to the relatively dry condition that will not cause much changes for the crystal structure. However, if we compare the sizes of crystalline structures at 75%RH under drying process and humidification, respectively, we will find that the sizes of crystalline structures under humidification process are perceivably larger. This shows on the one side, the established crystalline structure may not be disrupted by the drying process, and the crystallization process will resume as the humidification process starts, hence the general

increase of size at the end of the ramp; on the other hand, this is also possibly due to that the films do not achieve their equilibrium structure while at the 75%RH of the drying process.[36 37]

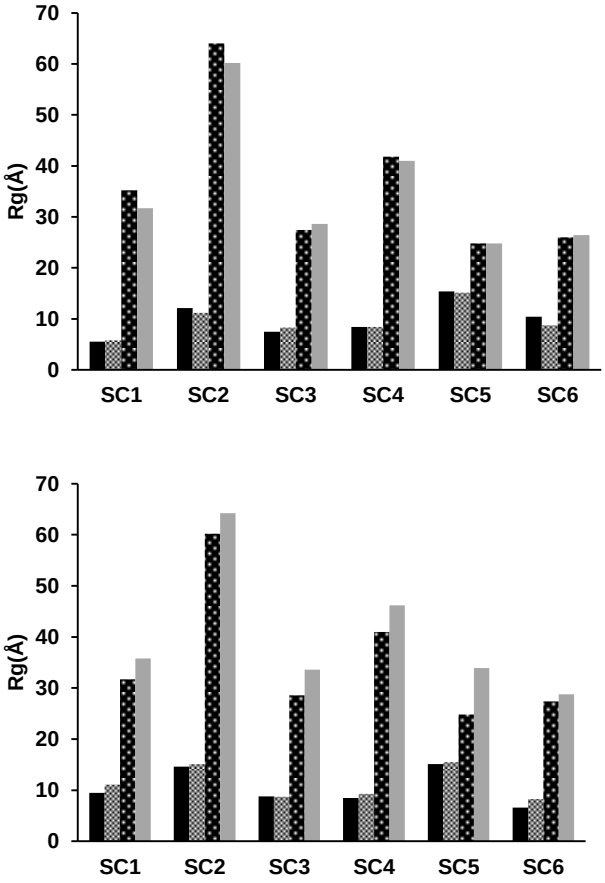

Figure 4.3 Numerical fit results: comparison of sizes at drying process A and humidification process B for different films at 25%RH (top) and 75%RH (bottom): ■ L1 Drying; ▩ L1 Humidification; ◙ L2 Drying; ■ L2 Humidification.

4.5.3 Particle Shape

From table 4.3, we observed that for the crystal structure (L2) of SC1, SC3, SC4, and SC6, the inverse power low slope decreases upon hydration at 95%RH, indicating the formation of low dimensional particles e.g. elongated rod (with inverse power low slope of 1), as suggested

by Beaucage.[38] This agrees with our previous results on PFSAs.[19] At 95%RH, when the films absorb more water, the structures become more mobile and has more freedom to form aggregates of energetically favorable shapes corresponding to different hydration levels, as shown by the research done by Gebel, et al.[15]

Table 4.3 Inverse power law slope for 3M side chain series at different RHs

	SC1	SC2	SC3	SC4	SC5	SC6	3M825EW
25%RH P L2 (Å)	2.1	1.1	1.8	2.0	1.4	1.8	2.4
95%RH P L2 (Å)	1.6	N/A	1.6	1.7	N/A	1.3	1.1

* Values of 3M PFSA (3M825EW) are extracted from our previous work.[19]

4.5.4 Effect of Chemical Structures

A comparison of morphology for films with different structures is shown in Figure 4.4. From Figure 4.4a, we can see that SC2 (PFIA) forms much larger structures for both levels (11.2 and 64 for level1 and level2 respectively at 25% RH and 16.5 and 65.7 for level 1 and level2 respectively at 95%RH) as compared to that of SC3 (Ortho bis) (8.3 and 28.8 Å for level1 and level2, respectively at 25% RH and 12 and 36.3 Å for level 1 and level2, respectively at 95%RH). Although both ionomers have the same EW and same number of sorption functional groups on the side chain, i.e., they have similar IEC, however, due to the presence of phenyl group on the side-chain of SC3, the mobility of its side-chain is greatly reduced by the steric hindrance of this group. As a result, they form much smaller ionic clusters as well as the crystalline domains than the SC2 ionomer, which has very hydrophilic and mobile side-chains. As compared to 3M 825EW PFSA, SC2 also was larger ionic and crystal domains. For the ionic

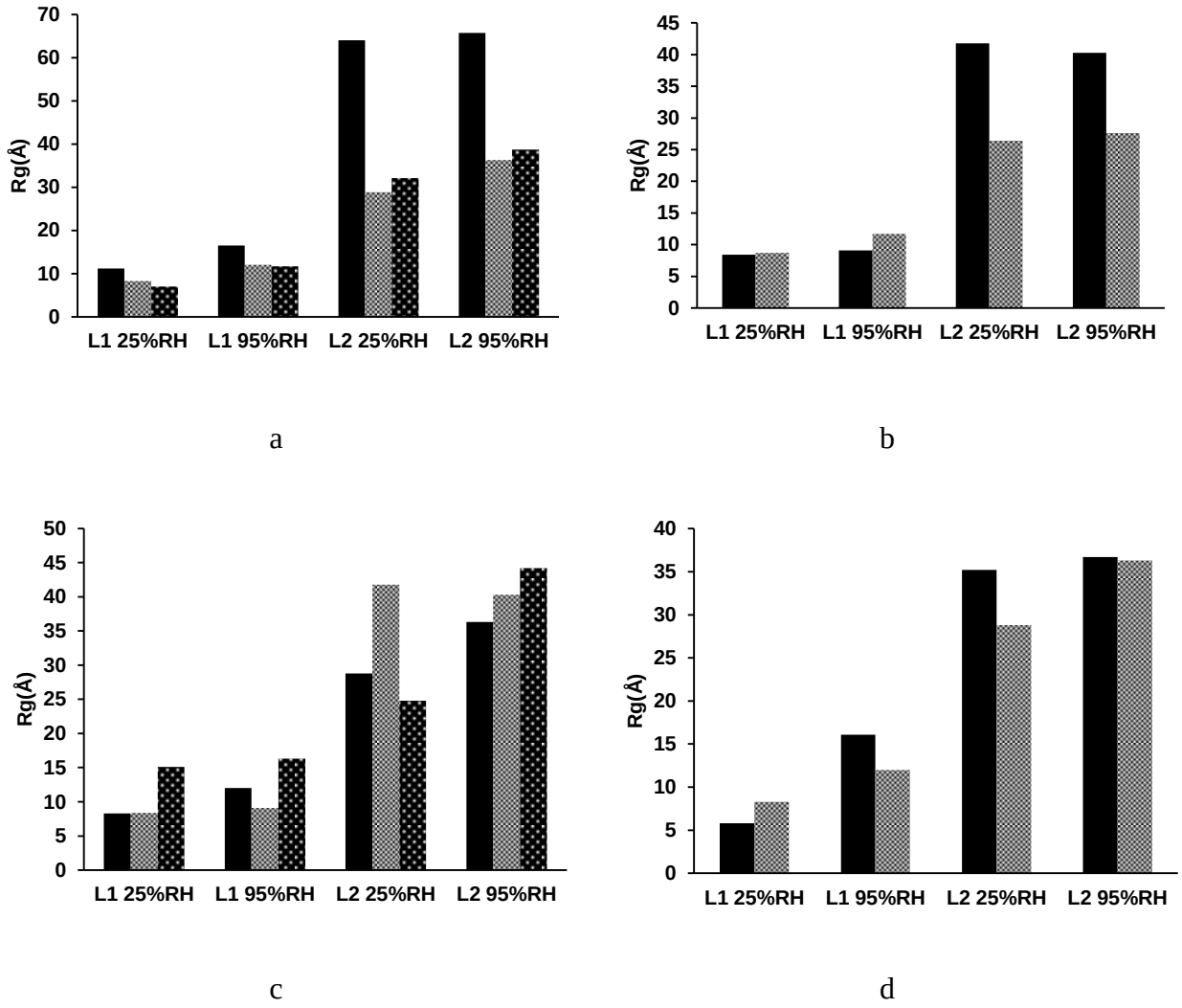

Figure 4.4 Size comparison of films with different side chain structures or EWs: a: ■ SC2, ▩ SC3; b: ■ SC4, ▩ SC6; c: ■ SC3, ▩ SC4, ▩ SC5; d: ■ SC1, ▩ SC3.

domain, since SC2 has two acid sites on the side chain, making it more hydrophilic. It has a larger hydrophilic region. For the second structure level, i.e., the crystal domain, SC2 possesses much larger structure size of SC2 than 3M 825EW PFSA. We hypothesize that the plasticizing effect of water on the extremely hydrophilic side chains of SC2 could make it very flexible and capable of being incorperated to the crystal domain. For SC4 (Phenyl imide) and SC6 (Penta Flouride) (Figure 4.4b), the sizes of the ionic domains are about the same at 25%RH (8.4 Å for SC4 and 8.7 Å for SC6), while at 95%RH, that of SC6 (11.7 Å) is larger than SC4 (9.1 Å). This is in good agreement with our dynamic vapor sorption (DVS) measurement result (Figure 4.5), where the water uptake are 2.8% and 4.6% for SC4 and SC6, respectively at 25%RH; while the large scale water uptake really takes place at higher 95%RH for SC6, where the water uptake values become 13% and 50.3% for SC4 and SC6, respectively. This shows that the penta fluoridated phenyl group makes the water sorption site more hydrophilic, possibly due to the change of charge distribution in the side chain groups caused by this substitution. To the contrary, the crystalline structural levels of SC6 (24.6 and 27.6 Å at 25%RH and 95%RH, respectively) are much smaller than that of SC4 (41.8 and 40.3 Å at 25% and 95% RH, respectively). The exact reason for this is unknown at this moment; however, the slightly smaller EW of SC6 could contribute to a smaller crystal domain. As for SC3 (Ortho bis), SC4 (Phenyl imide), and SC5 (Meta bis) (Figure 4.4c), despite a much smaller EW (644EW), compared to the other two ionomers, we notice that SC4 forms the smallest ionic clusters among the three ionomers, while SC5 forms the largest ones (8.3, 8.4, and 15.1 Å at 25%RH; 12, 9.1 and 16.3 Å at 95%RH for SC3, SC4 and SC5). The following factors can cause these differences: firstly, the additional sulfonic group attached to the phenyl group makes the film more hydrophilic, as compared to ionomers with only one acid group on the side chain, i.e., the effective EW should

be much lower due to the presence of additional acid sites; secondly, as for the difference between SC3 and SC4, we should consider the steric effect again, in this case, the sulfonic acid group at Ortho-bis position (SC3) will receive more steric hindrance than at Meta-bis position (SC5) in the water sorption process. For the crystalline structures, SC4 has the largest domain size, due to its hydrophobicity and more symmetrical side-chain groups. However, we observed a huge increase in crystal size at SC5 at high RH. One possible reason is again the plasticizing effect of water on this ionomer. Last, we compare the SC1 and SC3 (Figure 4.6d), which are the same ionomer with different EWs (1000EW for SC1 and 812 EW for SC3). At low RH, we observe that SC1 has larger crystalline domain size (35.2 Å) but smaller ionic domain size (5.8 Å) than SC3 (28.8 and 8.3 Å), which is well expected according to the definition of EW, i.e., the higher EW ionomer has larger portion of backbone region and smaller portion of side chain region. However, at high RH, the ionic domain size of SC1 (16.1 Å) exceeds that of SC3 (12 Å), while the sizes of crystalline domain become about the same (36.7 Å for SC1 and 36.3 Å for SC3). The cause of this is not clear for now, but we can see the huge effect of water presence to the morphology of perfluorated PEMs.

From the water sorption isotherm (Figure 4.5), we noticed that SC4 has the smallest water uptake, due to its hydrophobic side chain structure. SC6 exhibited the highest water uptake at 95%RH, possibly caused by its very low backbone EW. SC2 (PFIA) has more water uptake than 3M825EW (PFSA), due to its extra acid sites on the side chain. We also noticed that SC2 has a larger rate of size increase (from 11.2 Å at 25%RH to 16.5 Å at 95%RH) upon hydration for the ionic clusters compared to SC6, with relatively lower water uptake (from 9.8% at 25%RH to 35% at 95%RH), probably due to more combination effect of ionic clusters with water uptake,

i.e. smaller numbers of larger clusters are formed in SC2, while ionic clusters mainly existed as smaller isolated domains in SC6.

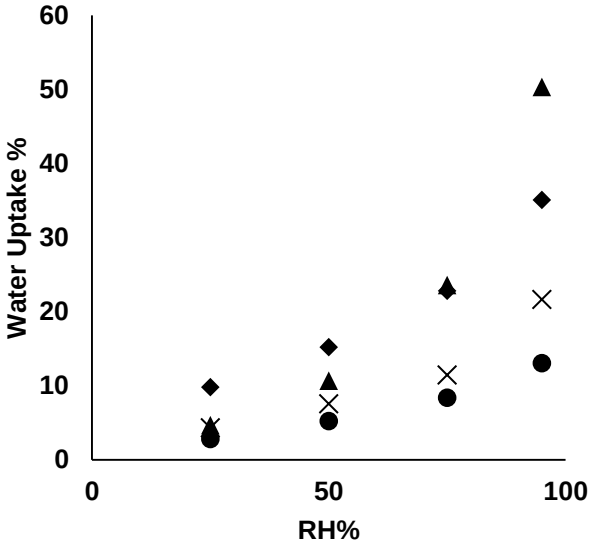

Figure 4.5 DVS water sorption isotherm for: (◆) SC2, (●) SC4, (▲) SC6, and (×) 3M825EW PFSA.

4.6 Conclusion

For perfluorinated PEMs with different chemical structures studies, sizes of both hydrophilic ionic domain and hydrophobic crystalline domains increase with water content. The size variation of hydrophilic ionic domains is found to be reversible, and the crystallization process on the other hand irreversible. The shapes of crystalline structures are found to change with variation in water content. Chemical structures especially side-chain structures are found to have significant effect on the morphology of perfluorinated PEMs: PFIA forms larger ionic domains than Ortho bis ionomer due to its flexible and bulky side chain with less steric

hindrance; and contrary to the low EW PFSA (EW<700), for which no crystallinity is observed, the nano crystal structures present in all PEMs investigated in this study.

4.7 Acknowledgement

This work was funded by the U.S. Department of Energy under EERE Cooperative Agreement No. DE-FG36-07G017006, and partially by the National Science Foundation (NSF) through the Renewable energy MRSEC under grant DMR-0820518. Use of the Advanced Photon Source was supported by the U.S. DOE (Contract No. DE-AC02-06CH11357). The authors also want to thank 3M for supplying ionomer samples and technical support.

4.8 References

(1) Aoki, M.; Asano, N.; Miyatake, K.; Uchida, H.; Watanabe, M. *Journal of the Electrochemical Society* **2006**, *153*, A1154.

(2) Yoshitake, M.; Watakabe, A. *Fuel Cells I* **2008**, *215*, 127.

(3) Xing, D. M.; Zhang, H. M.; Wang, L.; Zhai, Y. F.; Yi, B. L. *Journal of Membrane Science* **2007**, *296*, 9.

(4) Haugen, G. M.; Meng, F. Q.; Aieta, N. V.; Horan, J. L.; Kuo, M. C.; Frey, M. H.; Hamrock, S. J.; Herring, A. M. *Electrochemical and Solid State Letters* **2007**, *10*, B51.

(5) Wu, D. S.; Paddison, S. J.; Elliott, J. A. *Energy & Environmental Science* **2008**, *1*, 284.

(6) Tant, M. R.; Darst, K. P.; Lee, K. D.; Martin, C. W. *Acs Symposium Series* **1989**, *395*, 370.

(7) Whiteley, L. D.; Martin, C. R. *Journal of Physical Chemistry* **1989**, *93*, 4650.

(8) Kreuer, K. D.; Rabenau, A.; Weppner, W. *Angewandte Chemie-International Edition in English* **1982**, *21*, 208.

(9) Kreuer, K. D. *Chemistry of Materials* **1996**, *8*, 610.

(10) Glasstone, S.; Laidler, K. J.; Eyring, H.; McGraw-Hill: New York, **1941**, p 550

(11) Sagnella, D. E.; Laasonen, K.; Klein, M. L. *Biophys J* **1996**, *71*, 1172.

(12) Gierke, T. D.; Munn, G. E.; Wilson, F. C. *Journal of Polymer Science Part B-Polymer Physics* **1981**, *19*, 1687.

(13) Mehta, V.; Cooper, J. S. *Journal of Power Sources* **2003**, *114*, 32.

(14) Li, Q. F.; He, R. H.; Berg, R. W.; Hjuler, H. A.; Bjerrum, N. J. *Solid State Ionics* **2004**, *168*, 177.

(15) Gebel, G. *Polymer* **2000**, *41*, 5829.

(16) Clark, J. K.; Paddison, S. J. *Electrochim Acta* **2013**, *101*, 279.

(17) Paddison, S. J.; Elliott, J. A. *Phys Chem Chem Phys* **2006**, *8*, 2193.

(18) Aieta, N. V.; Stanis, R. J.; Horan, J. L.; Yandrasits, M. A.; Cookson, D. J.; Ingham, B.; Toney, M. F.; Hamrock, S. J.; Herring, A. M. *Macromolecules* **2009**, *42*, 5774.

(19) Liu, Y.; Horan, J. L.; Schlichting, G. J.; Caire, B. R.; Liberatore, M. W.; Hamrock, S. J.; Haugen, G. M.; Yandrasits, M. A.; Seifert, S.; Herring, A. M. *Macromolecules* **2012**, *45*, 7495.

(20) Elliott, J. A.; Hanna, S.; Elliott, A. M. S.; Cooley, G. E. *Macromolecules* **2000**, *33*, 4161.

(21) Rubatat, L.; Gebel, G.; Diat, O. *Macromolecules* **2004**, *37*, 7772.

(22) Rubatat, L.; Rollet, A. L.; Gebel, G.; Diat, O. *Macromolecules* **2002**, *35*, 4050.

(23) Eikerling, M.; Kornyshev, A. A.; Spohr, E. *Fuel Cells I* **2008**, *215*, 15.

(24) Li, Y. J.; Peiffer, D. G.; Chu, B. *Macromolecules* **1993**, *26*, 4006.

(25) Hamrock, S. J. *DOE Hydrogen Program FY 2010 Annual Progress Report* **2010**, 748.

(26) Beaucage, G. *Journal of Applied Crystallography* **1995**, *28*, 717.

(27) Porod, G.; *Kolloid, Z.* **1951**, ***124***, 83.

(28) Gebel, G.; Lambard, J. *Macromolecules* **1997**, *30*, 7914.

(29) Elliott, J. A.; Hanna, S.; Elliott, A. M. S.; Cooley, G. E. *Polymer* **2001**, *42*, 2251.

(30) Mauritz, K. A.; Moore, R. B. *Chemical Reviews* **2004**, *104*, 4535.

(31) Hsu, W. Y.; Gierke, T. D. *Macromolecules* **1982**, *15*, 101.

(32) Gierke, T. D.; Hsu, W. Y. *Acs Symposium Series* **1982**, *180*, 283.

(33) de Almeida, S. H.; Kawano, Y. *J Therm Anal Calorim* **1999**, *58*, 569.

(34) Satterfield, M. B.; Majsztrik, P. W.; Ota, H.; Benziger, J. B.; Bocarsly, A. B. *Journal of Polymer Science Part B-Polymer Physics* **2006**, *44*, 2327.

(35) Kim, Y. S.; Dong, L. M.; Hickner, M. A.; Glass, T. E.; Webb, V.; McGrath, J. E. *Macromolecules* **2003**, *36*, 6281.

(36) Satterfield, M. B.; Benziger, J. B. *Journal of Physical Chemistry B* **2008**, *112*, 3693.

(37) Bass, M.; Freger, V. *Polymer* **2008**, *49*, 497.

(38) Beaucage, G.; Schaefer, D. W. *Journal of Non-Crystalline Solids* **1994**, *172*, 797.

CHAPTER 5 MORPHOLOGY STUDY OF RANDOM AND BLOCK COPOLYAMIDE PEMS SYNTHESIZED THROUGH COPOLYMERIZATION OF M-PHYLENE DIAMINE (MPDA), 5-SULFOISOPHTHALIC ACID (SIPA) AND ISOPHTHALIC ACID (IPA): IMPLICATION OF MORPHOLOGY TO THEIR WATER UPTAKE AND PROTON CONDUCTIVE PROPERTIES

Yuan Liu,[†,§] Feilong Liu,[‡, §] Daniel M. Knauss,[*, ‡] and Andrew M. Herring[*,†]

5.1 Abstract

Both random and block copolyamide proton exchange membranes (PEMs) were synthesized through copolymerization of m-phenylene diamine (MPDA), 5-sulfoisophthalic acid (SIPA) and isophthalic acid (IPA), and then characterized. The water uptake is found to increase with IEC. The block copolymer shows less water uptake than the random one, indicating a higher dimensional stability. Both random and block copolymers show higher conductivity than Nafion™ at higher temperatures, with the random and block copolymer achieving 163 mS/cm at80 °C and 156 mS/cm at 90 °C, respectively. SAXS patterns show the ionomer peak at ca. q=0.1 $Å^{-1}$ for the dry block copolymer, and its intensity increases upon the initial humidification at 25%RH, then decreases with the following humidification at 50%, 75%, and 95%RH. No

[†]Department of Chemical and Biological Engineering, Colorado School of Mines, Golden, Colorado 80401, United States

[‡] Department of Chemistry and Geochemistry, Colorado School of Mines, Golden, Colorado 80401, United States

[*]Corresponding Authors

[§]These authors contributed equally.

peak is observed for the random copolymer.

5.2 Introduction

Fuel cells are promising energy conversion devices, which are receiving considerable attention due to their high efficiency and low pollution at the point of use.[1,2] Proton exchange membrane fuel cells (PEMFCs) in particular possess favorable properties such as high power density, system versatility, quick startup, and are suitable for portable applications.[3] Several perfluorosulfonic acid (PFSA) polymers have been developed such as Nafion™ by Du Pont Co. primarily as a permselective separator in chlor-alkali electrolyzers,[4] an intermediate side-chain ionomer by 3M company,[5] and a short side-chain ionomer, originally developed by Dow and currently produced by Solvay Solexis as Aquivion™.[6,7] These PFSAs generally have excellent chemical stability and high proton conductivity, and are capable of maintaining mechanical integrity under harsh operating conditions,[8,9] and so serve as benchmark materials in a lot of fuel cell studies. However, the application of fluorinated PEMs in fuel cells are always hindered by their potential high-cost and environmental concerns of their manufacture.[9,10] The loss of water at elevated temperatures (above 100 °C) for PFSAs also leads to a dramatic decrease in conductivity.[11-13] Operating fuel cells at higher temperatures will be beneficial in that CO tolerance can be improved and the heat exchange system can also be simplified.[14-18] Therefore, the development of less expensive and more environmentally friendly alternative PEMs, which are capable of operation at higher temperatures, becomes a major effort in fuel cell research. Sulfonated aromatic hydrocarbon PEMs such as sulfonated polyetheretherketone (SPEEK) are potential materials to meet these requirements that have been studied extensively.[19-23]

A morphological study of PEMs is essential to understand their transport and mechanical properties. A tremendous amount of such studies have been carried out through the last 3 decades.[24-32] These studies have been greatly facilitated by the adaption of small angle X-ray and neutron scattering techniques. A phase-separated morphology has been generally accepted for PFSA;[33] however, the exact morphology regarding the shape, size and distribution of these nanostructures is still the subject of some debate. Gierke *et al.* proposed a cluster network model,[7] which served as a base for morphology study of PFSA, and adequately explained the high-q maxima or so-called ionomer peak observed in small angle scattering studies. Several such inter-particle models which attribute the ionomer peak to the inter-particular origin have been proposed such as a lamella model by Litt et al.,[34] and a parallel cylindrical model by Schmitt et al.[35] An intra-particle model, which associates the ionomer peak with the intra-particle core-shell structure: the core-shell model was also proposed by Fujimura et al.[36] Gebel et al. studied the evolution of structure at different hydration levels and found the shape of nano domains changes upon hydration.[37] Like PFSA, sulfonated aromatic hydrocarbon PEMs such as SPEEK also contain sulfonic side groups serving as charge sites for proton transport. Therefore, they also form hydrophilic-hydrophobic phase separated morphology, but to a lower degree as compared to PFSAs, indicated by narrower ion conductive channels.[16] To improve the ion conductivity and mechanical properties, several block copolymers with better phase separated morphology were studied.[38,39]

In our previous work, we found that the connectivity of hydrophilic domains will have a large effect on PEM's transport properties.[40] In this work, we investigated the morphology evolution of newly developed MPDA-SIPA copolymers upon hydration, in an effort to relate

their morphology to the proton conductivity, water uptake behavior, chemical and mechanical stability. Properties of random and block copolymers have also been compared.

5.3 Experimental

Detailed descriptions of water uptake, conductivity, and SAXS measurements are presented in this section.

5.3.1 Materials

Both random MPDA-SIPA$_x$ (H) and block (MPDA-SIPA$_x$)-b-(MPDA-IPA)(H) copolyamides with various IECs were prepared (details about synthesis, NMR characterization, and IEC determination are provided in Appendix B).

5.3.2 Characterization and Measurements

The water uptake of films at different RH were determined gravimetrically using a dynamic vapor sorption instrument (DVS Advantage, SMS Inc.) The weight of film was measured with respect to time and RH. The λ values defined as the number of water molecules per charge were calculated for 25%, 50%, 75% and 95%RH, based on the obtained water sorption isotherms.

In-plane conductivity was measured by electrochemical impedance spectroscopy (EIS) using a 4-probe Teflon cell with Pt electrodes connected to a BioLogic VMP3 Potentiostat in a frequency range from 1 Hz to 100 kHz. A TestEquity® (Solatron 1007H Model) environmental chamber was used to control the temperature and RH. The ionic conductivity was obtained from

the following equation:

$$\sigma = \frac{d}{L_s W_s R}$$

where σ is the ionic conductivity of the membrane (S cm^{-1}), d is the distance between reference electrodes (mm), L_s and W_s are the thickness (mm) and width (mm) of the membrane, R is the ohmic resistance of the membrane (Ω).

SAXS experiments were performed using X-rays of 18keV from synchrotron radiation source at beamline (12ID C-D) of Advanced Photon Source (APS), Argonne National Laboratory, (Argonne, IL). The detailed experimental setup is shown in our previous work.[32] SAXS measurements were performed under 0%, 25%, 50%, 75% and 95%RH at 60 °C. A one-hour equilibrating time was set for each humidification step up to 95%RH, with X-ray shots taken for 3 samples and 1 Kapton background at the end of each equilibrating step. During the equilibration, multiple dynamic shots were performed at one chosen sample. Kapton background was subtracted using Argonne SAXS software package for Igor Pro.

5.4 Results and Discussion

In this work, both random (with a measured IEC of 1.44) and block copolyamides with a degree of sulfonation (DS) of 40 mol% are studied, hereafter referred as random copolymer and block copolymer, respectively.

5.4.1 Water Uptake

The water sorption isotherms for the random and block copolymers are shown in figure 5.1. The water number λ (defined as number of water molecules per charge) at equilibrium under different RH is calculated from water sorption profiles and shown in figure 5.2. The block copolymer has less water uptake than the random copolymer, indicating less swelling and better dimensional stability. This is expected because compared to the structure of random copolymer, there are longer hydrophobic and hydrophilic chains in block copolymer. These structures could form much stronger hydrogen bonds between the unsulfonated chains and keep fewer water molecules around the polymer chain, and so provide higher dimensional stability and lower water uptake than in the random copolymer. This is further elucidated by the cluster network morphology and higher degree of phase separation in the block copolymer, and we will discuss this with more detail in the following section. We also observed a threshold of massive water uptake at around 75%RH, which is in agreement with our previous observation.[40] This is because at lower RHs, the water uptake is hindered by the hydrophobic nature of the polymer;[41] at high RHs under which H_2O vapor has sufficient chemical potential to overcome the resistance, the polymer swells, so large amounts of water uptake begin.

5.4.2 Stability in Water

From table 5.1, we can see that the block copolymer has longer sustainability than the random one: the block copolymer is insoluble in water at temperatures ≤70 °C, while the random one starts to lose its mechanical integrity at 70 °C. Such difference in water solubility is attributed to their different morphologies, i.e., ordered nano-structures exist in the block

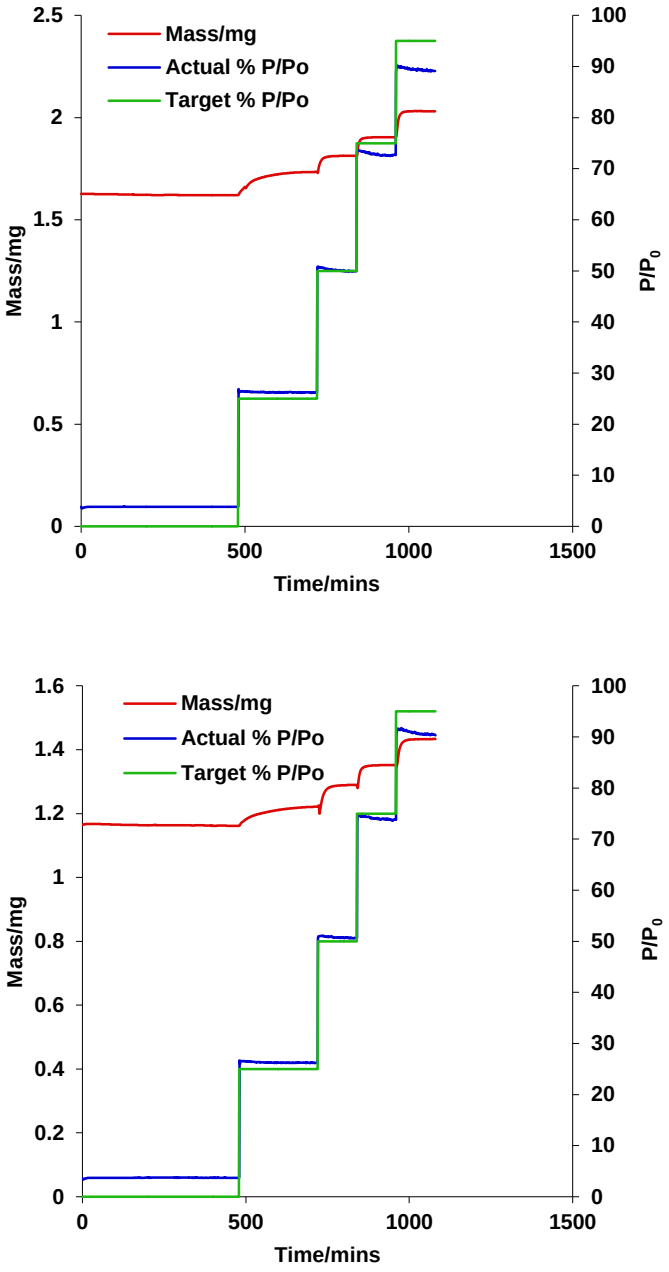

Figure 5.1 Water sorption isotherm at 60 °C: random copolymer (top) and block copolymer (bottom).

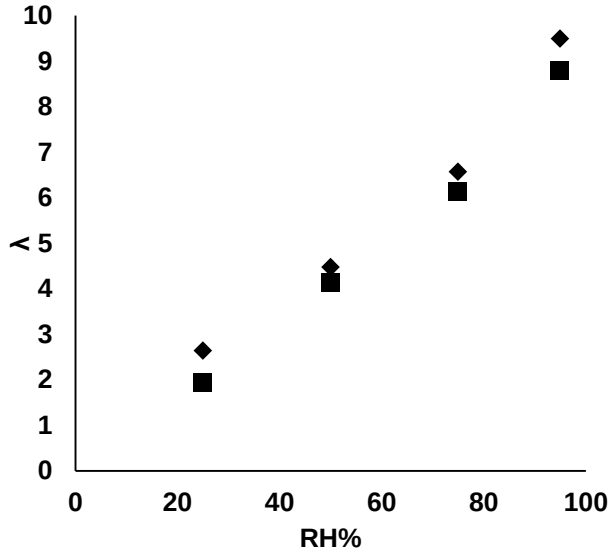

Figure 5.2 Water number at different temperature: random copolymer (◆) and block copolymer (■).

Table 5.1 Film's Stability in Water at Various Temperatures

Membrane	25°C	40°C	50°C	60°C	70°C	80°C	90°C	100°C
Block copolymer	-	-	-	-	-	180min	171min	28min
Random copolymer	-	-	-	-	62min	32min	21min	9min

* "-" represents insoluble

copolymer, while the random ones are amorphous. This difference will be further discussed in the following section.

5.4.3 Proton Conductivity

From figure 5.3, we notice both random and block copolymers have higher proton conductivity than Nafion™ at 80 °C (163, 124, and 114 mS/cm for random copolymer, block copolymer, and Nafion™ 117, respectively.), resulting from a better water retention capability

for these aromatic hydrocarbon PEMs. The conductivity of random copolymer is not measureable at temperatures above 80 °C, due to the loss of mechanical integrity.

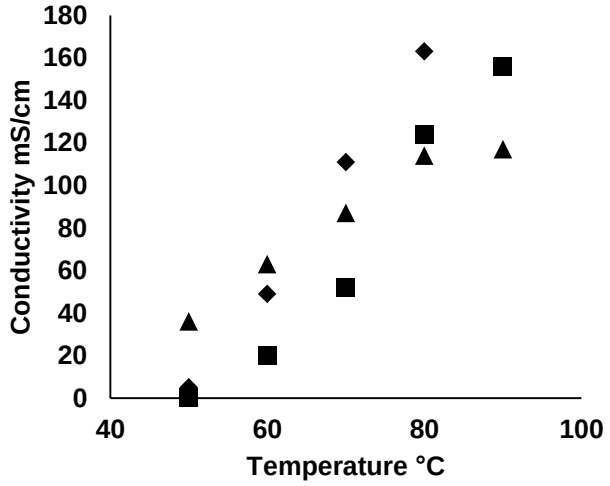

Figure 5.3 Conductivity of the random copolymer (◆), block copolymer (■), and Nafion^{TM}-117 (▲) at 95%RH and different temperature.

5.4.4 Morphology

From the SAXS results of the block copolymer (Figure 5.4) we notice a maxima at around q=0.09 Å^{-1} for each curve at different hydrations. The SAXS patterns of films exchanged with different cations were also obtained as shown in figure 5.5, we observed the maxima at similar q and it increases as the electron density of cations increases, i.e. Na<K<Cs. This confirms that this maximum is arising from ionic domains--the so-called ionomer peak, which is in good agreement with the results obtained by Gebel et al. for SPEEK.[23] The dynamic change of the ionomer peaks, therefore, provides insights into the film's morphology at different humidities. At the initial 25%RH after drying (figure 5.4 top), we observed that the intensity of the ionomer peak increased with equilibration time, showing that water gets into the hydrophilic ionic

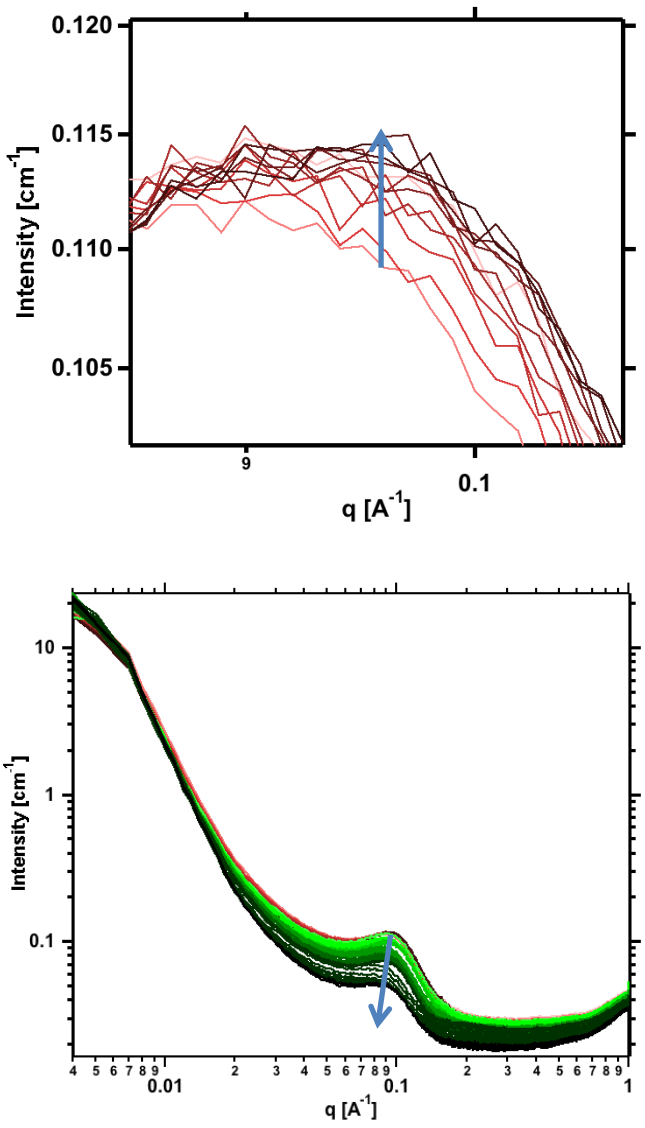

Figure 5.4 Dynamic SAXS curves of block copolymer: (top) light to dark brown: equilibrating at 25%RH after drying; (bottom) light to dark green: equilibrating at 50%, 75% and 95%RH.

domains. The following humidification steps at 50%, 75% and 95%RH (Figure 5.4 bottom) show the opposite trend: the intensity of ionomer peak decreased monotonically. This trend is also observed by Ohira et al. for poly(phenylene sulfide),[42] but normally not observed in PFSAs, as shown by our previous results.[32] To confirm that the decrease of ionomer peak intensity is not caused by the degradation of the polymer backbone, we performed a reversibility test (Figure 5.6)

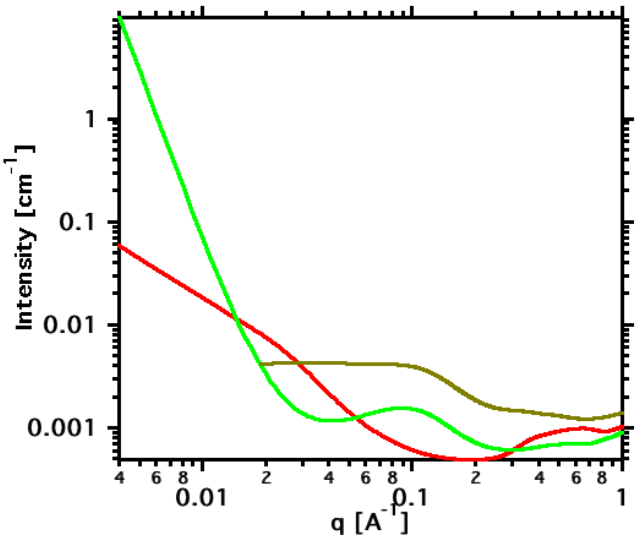

Figure 5.5 SAXS patterns of block copolymer exchanged with different ions: Na^+ (red), K^+ (green), and Cs^+ (brown).

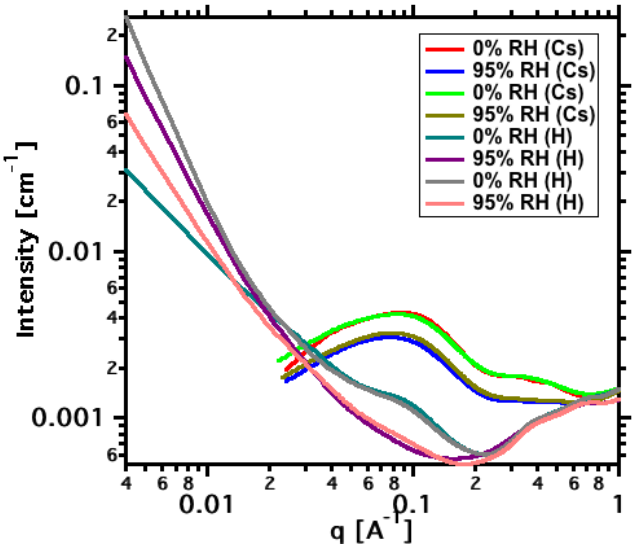

Figure 5.6 Reversibility tests of ionomer peaks for block copolymer.

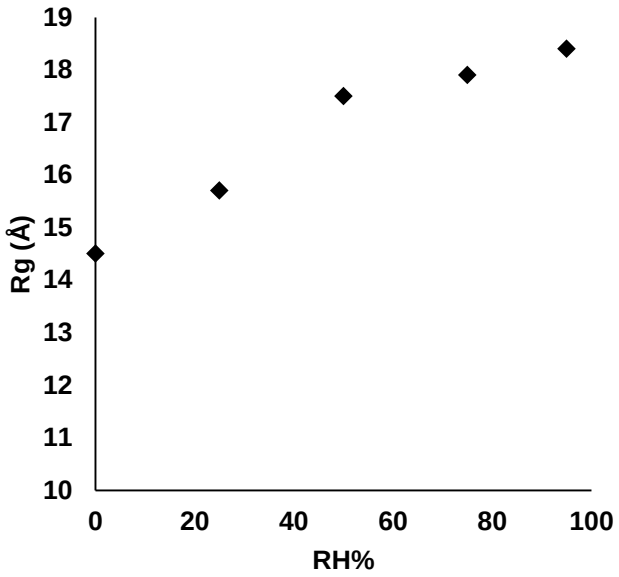

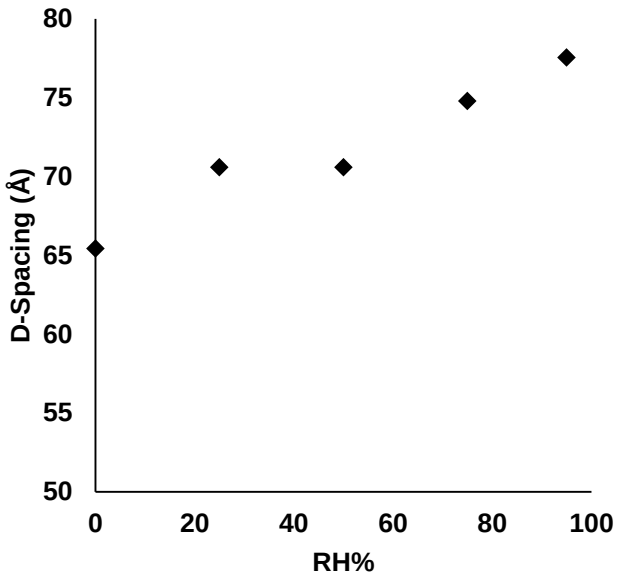

Figure 5.7 Calculated SAXS results at different RH for block copolymer: radius of gyration (top) and D-spacing (bottom).

where films went through a dry-wet-dry-wet cycle for both Cs^+ and H^+ form films, which shows excellent reversibility of the ionomer peak. This precludes the possibility of degradation of the polymer even under acidic conditions. Based on these observations, we propose a morphological evolution process: after the initial water uptake and swelling, when the ionic clusters reach a certain size, due to the rigidity of aromatic polymer chains, water starts getting into the polymer matrix, such that the ionic domains will become less prominent, as indicated by the ionomer peak. To further investigate this observation, we calculated the R_g of the ionic cluster using the unified fit model (Figure 5.7 top), and as we noticed, although R_g increases with RH, this increase is not as prominent as for the PFSA we observed in our previous study.[32] This could be due to some water diffusing into the polymer matrix instead of contributing to the swelling of the cluster, unlike PFSA, which has a very sharp hydrophobic/hydrophilic separation. The D-spacing calculated from the ionomer peak positions (Figure 5.7 bottom) also increases as film gets hydrated, showing the swelling of the film. Since the overall intensity of the high q region decreases, it is also possible that some large structures were formed which could show on the lower q range.[43] Indeed, we observed an iso-scattering point around 0.008 A^{-1}. This indicates a phase transition between two structures. The ultra small angle upturn is commonly attributed tothe long-range homogeneity of hydrophilic domains; therefore, the hydrophilic domains at such size-scale generally become more homogeneous as more water reaches the film, which is in agreement with our previous PGSE-NMR study of the tortuous diffusion of HPA doped PFSA.[40]

The SAXS pattern of random copolymer (Figure 5.8) shows no ionomer peak under all RHs. There is a shoulder appearing at 75%RH, which is usually attributed to the so-called "crystal knee",[33] originated from the scattering of nano-crystal structures. It is a well-known fact that water can serve as a plasticizer and greatly lower the glass transition temperature of

polymers, and allow polymer chains to gain enough mobility to crystallize.[32] We also observed a peak at around q=0.4 $Å^{-1}$, with a D-spacing of about 15.7Å. This feature is caused by scattering from sulfonic acid groups. The sudden increase in intensity at 95%RH indicates the excessive uptake of water, possibly caused by the loss of integrity of the film.

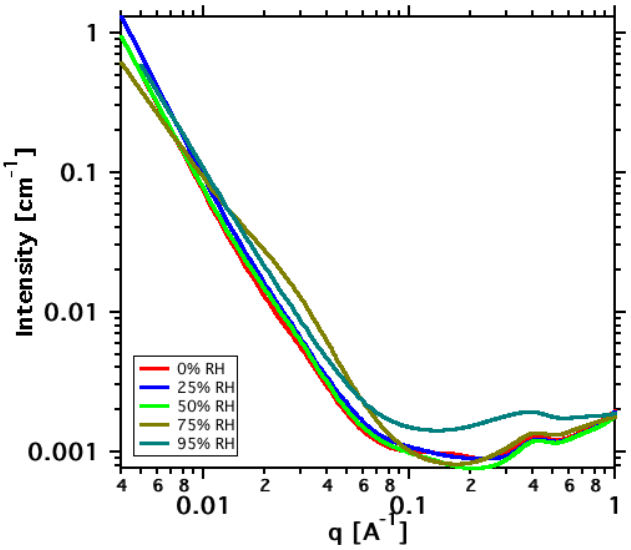

Figure 5.8 SAXS curves of random copolymer at different RHs.

The striking differences of the scattering pattern of block and random copolymers revealed a great difference in morphology, i.e. an ordered structure with a network of ionic clusters vs. a random morphology formed by entanglements of polymer chains. This difference has further implication for their mechanical and transport behaviors. For block copolymer, the existence of ordered nano-structures provides more mechanical and thermal stability than the random copolymer, where the ion-conductive channels randomly cross through the films. On the other hand, the water in the ionic domains of the block copolymer could get into the polymer matrix, which results in a less degree of phase separation. This observation can partially explain

the block copolymer's lower proton conductivity than the random one, and provide guideline to further improve its proton transport properties, i.e., by inducing a larger degree of hydrophilic/hydrophobic phase separation, which is favorable to proton transport.

5.5 Conclusion

The water uptake of films was found to increase with IEC. The block copolymer shows less water uptake than the random one, indicating a higher dimensional stability. Both random and block copolymers show higher conductivity than Nafion™ at higher temperatures, resulting from the better water retention capability of aromatic hydrocarbon PEMs. For the block copolymer, we observes the ionomer peak at around q=0.1 $Å^{-1}$, indicating the existence of an ordered ionic cluster network, and such a morphological feature can maintain better mechanical stability. A unique morphology evolution of block copolymer was observed from the dynamic change of the ionomer peak: its intensity increased at the initial humidification of 25%RH, then decreased at the following humidification of 50%, 75%, and 95%RH. This indicates that water reached out into the polymer matrix from the clusters, resulting in lower degree of phase separation. No ionomer peak was observed for the random copolymer, indicating a random arrangement of the polymer matrix, which accounts for a lower dimensional stability caused by excessive water uptake at high RHs.

5.6 Acknowledgements

We thank the NSF for funding this research through Renewable energy MRSEC under grant DMR-0820518. We also thank the Advanced Photon Source, Argonne National Laboratory, for providing beam time for the SAXS experiment.

5.7 References

(1) Kordesch, K. V.; Simader, G. R. *Chemical Reviews* **1995**, *95*, 191.

(2) Carrette, L.; Friedrich, K. A.; Stimming, U. *Chemphyschem* **2000**, *1*, 162.

(3) Kirubakaran, A.; Jain, S.; Nema, R. K. *Renew Sust Energ Rev* **2009**, *13*, 2430.

(4) Hickner, M. A.; Ghassemi, H.; Kim, Y. S.; Einsla, B. R.; McGrath, J. E. *Chemical Reviews* **2004**, *104*, 4587.

(5) Haugen, G. M.; Meng, F. Q.; Aieta, N. V.; Horan, J. L.; Kuo, M. C.; Frey, M. H.; Hamrock, S. J.; Herring, A. M. *Electrochemical and Solid State Letters* **2007**, *10*, B51.

(6) Stassi, A.; Gatto, I.; Passalacqua, E.; Antonucci, V.; Arico, A. S.; Merlo, L.; Oldani, C.; Pagano, E. *Journal of Power Sources* **2011**, *196*, 8925.

(7) Hsu, W. Y.; Gierke, T. D. *Journal of Membrane Science* **1983**, *13*, 307.

(8) Hamrock, S. J.; Yandrasits, M. A. *Polymer Reviews* **2006**, *46*, 219.

(9) Rikukawa, M.; Sanui, K. *Prog Polym Sci* **2000**, *25*, 1463.

(10) Steele, B. C. H.; Heinzel, A. *Nature* **2001**, *414*, 345.

(11) Bose, S.; Kuila, T.; Thi, X. L. N.; Kim, N. H.; Lau, K. T.; Lee, J. H. *Prog Polym Sci* **2011**, *36*, 813.

(12) Li, Q. F.; Jensen, J. O.; Savinell, R. F.; Bjerrum, N. J. *Prog Polym Sci* **2009**, *34*, 449.

(13) Jannasch, P. *Curr Opin Colloid In* **2003**, *8*, 96.

(14) Zhang, J. L.; Xie, Z.; Zhang, J. J.; Tanga, Y. H.; Song, C. J.; Navessin, T.; Shi, Z. Q.; Song, D. T.; Wang, H. J.; Wilkinson, D. P.; Liu, Z. S.; Holdcroft, S. *Journal of Power Sources* **2006**, *160*, 872.

(15) Yang, C.; Costamagna, P.; Srinivasan, S.; Benziger, J.; Bocarsly, A. B. *Journal of Power Sources* **2001**, *103*, 1.

(16) Kreuer, K. D. *Journal of Membrane Science* **2001**, *185*, 29.

(17) Meng, F. Q.; Aieta, N. V.; Dec, S. F.; Horan, J. L.; Williamson, D.; Frey, M. H.; Pham, P.; Turner, J. A.; Yandrasits, M. A.; Hamrock, S. J.; Herring, A. M. *Electrochim Acta* **2007**, *53*, 1372.

(18) Herring, A. M. *Polymer Reviews* **2006**, *46*, 245.

(19) Xing, P. X.; Robertson, G. P.; Guiver, M. D.; Mikhailenko, S. D.; Wang, K. P.; Kaliaguine, S. *Journal of Membrane Science* **2004**, *229*, 95.

(20) Robertson, G. P.; Mikhailenko, S. D.; Wang, K. P.; Xing, P. X.; Guiver, M. D.; Kaliaguine, S. *Journal of Membrane Science* **2003**, *219*, 113.

(21) Kaliaguine, S.; Mikhailenko, S. D.; Wang, K. P.; Xing, P.; Robertson, G.; Guiver, M. *Catal Today* **2003**, *82*, 213.

(22) Yang, B.; Manthiram, A. *Journal of Power Sources* **2006**, *153*, 29.

(23) Gebel, G. *Macromolecules* **2013**, *46*, 6057.

(24) Rollet, A. L.; Gebel, G.; Simonin, J. P.; Turq, P. *Journal of Polymer Science Part B-Polymer Physics* **2001**, *39*, 548.

(25) Loppinet, B.; Gebel, G. *Langmuir* **1998**, *14*, 1977.

(26) Essafi, W.; Gebel, G.; Mercier, R. *Macromolecules* **2004**, *37*, 1431.

(27) Gebel, G.; Moore, R. B. *Macromolecules* **2000**, *33*, 4850.

(28) Rubatat, L.; Rollet, A. L.; Gebel, G.; Diat, O. *Macromolecules* **2002**, *35*, 4050.

(29) Page, K. A.; Landis, F. A.; Phillips, A. K.; Moore, R. B. *Macromolecules* **2006**, *39*, 3939.

(30) Elliott, J. A.; Wu, D. S.; Paddison, S. J.; Moore, R. B. *Soft Matter* **2011**, *7*, 6820.

(31) James, P. J.; Elliott, J. A.; McMaster, T. J.; Newton, J. M.; Elliott, A. M. S.; Hanna, S.; Miles, M. J. *Journal of Materials Science* **2000**, *35*, 5111.

(32) Liu, Y.; Horan, J. L.; Schlichting, G. J.; Caire, B. R.; Liberatore, M. W.; Hamrock, S. J.; Haugen, G. M.; Yandrasits, M. A.; Seifert, S.; Herring, A. M. *Macromolecules* **2012**, *45*, 7495.

(33) Mauritz, K. A.; Moore, R. B. *Chemical Reviews* **2004**, *104*, 4535.

(34) Litt, M. H.; *Polym. Prepr.*: **1997**; Vol. 38, p 80.

(35) Schmidt-Rohr, K.; Chen, Q. *Nature Materials* **2008**, *7*, 75.

(36) Fujimura, M.; Hashimoto, T.; Kawai, H. *Macromolecules* **1981**, *14*, 1309.

(37) Gebel, G. *Polymer* **2000**, *41*, 5829.

(38) Roy, A.; Hickner, M. A.; Yu, X.; Li, Y.; Glass, T. E.; McGrath, J. E. *Journal of Polymer Science Part B: Polymer Physics* **2006**, *44*, 2226.

(39) Elabd, Y. A.; Hickner, M. A. *Macromolecules* **2011**, *44*, 1.

(40) Liu, Y.; Sambasivarao, S. V.; Horan, J. L.; Yang, Y.; Maupin, C. M.; Herring, A. M. *The Journal of Physical Chemistry C* **2013**.

(41) Zawodzinski, T. A.; Derouin, C.; Radzinski, S.; Sherman, R. J.; Smith, V. T.; Springer, T. E.; Gottesfeld, S. *Journal of the Electrochemical Society* **1993**, *140*, 1041.

(42) Barique, M. A.; Seesukphronrarak, S.; Wu, L. B.; Ohira, A. *Journal of Physical Chemistry B* **2011**, *115*, 27.

(43) Maes, A. M.; Pandey, T. P.; Vandiver, M. A.; Lundquist, L. K.; Yang, Y.; Horan, J. L.; Krosovsky, A.; Liberatore, M. W.; Seifert, S.; Herring, A. M. *Electrochim Acta* **2013**, *110*, 260.

CHAPTER 6 CONCLUSIONS

In this thesis we tested the influence of annealing, HPA doping, and side chain chemistry on the morphology and transport behavior of a PFSA ionomer membrane. The effect of block structure compared to random structure on a copolyamide material's morphology, dimensional stability, and proton conductivity was also investigated.

6.1 Annealing

For the first time we revealed the structural evolution process of as-cast PFSA membranes during heating, cooling, and hydration through dynamic SAXS measurement. This study shows the ionic domains grow upon heating. It also revealed that crystallization take place during cooling. Larger ionic domains are achieved upon hydration compared to the as-cast film. We demonstrated that the radius of gyration (R_g) of the ionic domains increase as annealing temperature increases (11.9, 15.5, and 17.1 Å for films annealed at 180, 190, and 200 °C, respectively), leading to higher conductivity (0.20, 0.25, and 0.36 S/cm for films annealed at 180, 190, and 200 °C, respectively). These results are attributed to the decreased tortuosity of the wider protonic conductive channels. This is in accordance with our hypothesis that higher temperature will lead to the formation of larger ionic clusters and improvement in conductivity. The increased thermal energy at higher temperatures enables the previous restricted ionic group to aggregates together with electrostatic force, and the existing cluster to rearrange, resulting in larger ionic clusters after annealing. The increase of ionic domain size is not so obvious as annealing temperature increased from 190 to 200 °C (from 15.5 to 17.1 Å), while the conductivity still increase substantially (from 0.25 to 0.36 S/cm). From a fit of the power law slope in the low q range of the SAXS pattern, we found out that the inverse power law slope

shows no significant change (from 1.5 to 1.4), when annealing temperature increased from 180 to 190 °C. However, the inverse power law slope decreased to 1.1 as annealing temperature reached 200 °C, indicating the formation of lower dimension and more elongated crystal structures. Such morphology is believed to improve proton conductivity. Therefore, we conclude that the increase of conductivity from 190 to 200 °C annealing temperatures is primary due to a geometrical change of polymer domains, which only occurs at very high annealing temperature (200 °C).

6.2 HPA Doping

A comparison of the measured conductivity by EIS and the calculated conductivity using Nernst-Einstein equation based on the water diffusion coefficient obtained from the PGSE-NMR study, we found out that the contribution of proton transport through the Grotthuss mechanism increased from 0.1 S/cm for undoped ionomer to 0.15 S/cm as the HPA doping level increases to 5%. This proves that the addition of HPA facilitates the Grotthuss hopping. HPAs are highly charged particles which will attract water and hydroniums to form hydration shells around the exterior oxygen atoms of the Keggin structure. This allows the HPA molecules to serve as hydration centers bridging the hydrophilic domains resulting in an interconnected hydrogen bonding network. The addition of HPA causes the hydrophilic domains to become more homogeneous, as revealed by the tortuous diffusion measurement: the tortuosity decreases 1.4 to 1.1, upon addition of 5% HPA. The decrease in tortuosity can be attributed to HPA's bridging effect. Although studies usually attribute the conductivity improvement to the facilitation of Grotthuss hopping by HPA addition, the proton transport through vehicle mechanism also affects the overall conductivity. The relative contribution of the Grotthuss mechanism compared to the

vehicle mechanism is heavily dependent on HPA doping level. At a 1% HPA doping level, the diffusion coefficient decreases from $4.1*10^{-6}$ to $2.2*10^{-6}$ cm^2/s. 5%HPA doping then increases the diffusion coefficient to $2.7*10^{-6}$ cm^2/s. This confirmed our hypothesis that non-monotonic behavior of water diffusion due to the dual effects of HPA doping on the water diffusion. The overall conductivity shows the similar trend. Upon 1%HPA doping, the system is disturbed by the reformation of hydrophilic domains around HPAs. Although domains become more interconnected, the water trapped by hydrogen bonding will greatly decrease the diffusion coefficient. Hence the conductivity decreases from 0.14 to 0.13 S/cm. Upon 5%HPA doping, the water domains reach a threshold of connectivity that the morphological factor will dominate to improve the diffusion coefficient, as compare to the 1%HPW doped system. The conductivity increases to 0.19 S/cm as a result. From above observations, we conclude that 5% HPA loading are desirable to achieve high conductivity.

6.3 Side Chain Chemistries

We found that the 3M PFIA forms larger ionic domains (R_g=17 Å) than the 3M PFSA (R_g=12 Å), due to its highly flexible and hydrophilic side chains. As expected, the water uptake at 95%RH is 35% for 3M PFIA, which is higher than 22% for 3M PFSA, showing the higher hydrophilicity of PFIA side chain. The meta bis forms larger ionic domains (R_g=16 Å) than the orth bis (R_g=12 Å), resulting from a larger separation distance between the sulfonic group and the imide group, as indicated by their chemical structures. A highly flexible side chain will have higher mobility to reach out and form ionic clusters; while more hydrophilic groups on the side chain will create larger hydration shells through electrostatic attraction with water and hydronium ions. The proximity of protogenic groups will hinder the water uptake because of

direct hydrogen bonding between the groups. A flexible, and hydrophilic side chain, with sufficient separation distance between protogenic groups therefore is desirable to obtain larger ionic channels favoring rapid proton transport. We also noticed that the crystalline peaks (q= ca. 0.05 $Å^{-1}$) are present in the SAXS patterns of 3M PFIA, while they are absent from those of the low EW PFSA. This result confirms that nano-crystals are preserved in the 3M PFIA, while lost in the 3M PFSA with similar effective EW. Since crystalline structures are known to provide films with mechanical strength, this difference in morphology can account for their different mechanical behaviors: the low EW PFSA (< 700 EW) completely lost their mechanical integrity in water resulting from excessive swelling. This precludes the PFSA membranes with <700 EW from serving as a viable PEM for fuel cell applications. The PFIA with similar EW forms crystalline structures which provide it with the mechanical integrity to survive harsh fuel cell operating condition (typically ≥80 °C with maximum humidity for PEMFC).

6.4 Hydrocarbon Copolyamide Material

The block copolyamide possesses ordered ionic domains, as shown by the presence of an ionomer peak in the SAXS patterns. Such ordered structures lead to higher dimensional stability of the block copolyamide compared to the random copolyamide, as indicated by their longer sustainability in water (3 hours at 80 °C and insoluble at temperature ≤70 °C), compared to random copolyamide (1 hour at 70 °C and 1/2 hour at 80 °C). The conductivity of the block copolyamide, although not as high as the random copolyamides, is higher than that of Nafion™ at temperatures ≥80 °C. This is attributed to the increased hydrophilicity of the backbone structure of the block copolyamide as compared to the tetrafluoroethylene (TFE) backbone of Nafion™. Based on these evaluations, we decided that block copolyamide is a material worth

pursuing. Its conductivity and dimensional stability can be potentially further improved. From the observations made in our present study, we identified the following factors that can be attributed to the lower conductivity of the block copolyamide: 1) the relative narrow hydrophilic domains, as calculated from the ionomer peak position of the SAXS patterns, and 2) a lower degree of phase separation between the hydrophobic and the hydrophilic domains which is evident in the SAXS patterns of the block copolyimide. The ionomer peak becomes less prominent upon hydration, indicating water becomes dispersed in the polymer matrix. We will address these issues in our proposed future work.

6.5 Suggested Future Work

The desired outcome of this study is to optimize the synthetic variables and pretreatment conditions that will produce PEMs with very high conductivity and dimensional stability capable of operating at drier (ambient humidity) and hotter (above 100 °C) conditions. Based on the knowledge we obtained through the present research, we suggest the following two approaches to achieve this objective: one based on modification of PFIA, and one based on the development of hydrocarbon materials. Performance enhancements through annealing and incorporation of HPA to the backbone will be adopted.

6.5.1 Approach A: Modification of PFIA

Based on the current study of the structure-morphology relationship of PEMs (Figure 6.1), the membrane structure containing PFIA side chains[1] is a preferred choice compared to the 3M membrane containing PFSA side chains to achieve wide ionic conductive channels favorable to the proton conduction, and at the same time maintain the crystalline structures, therefore

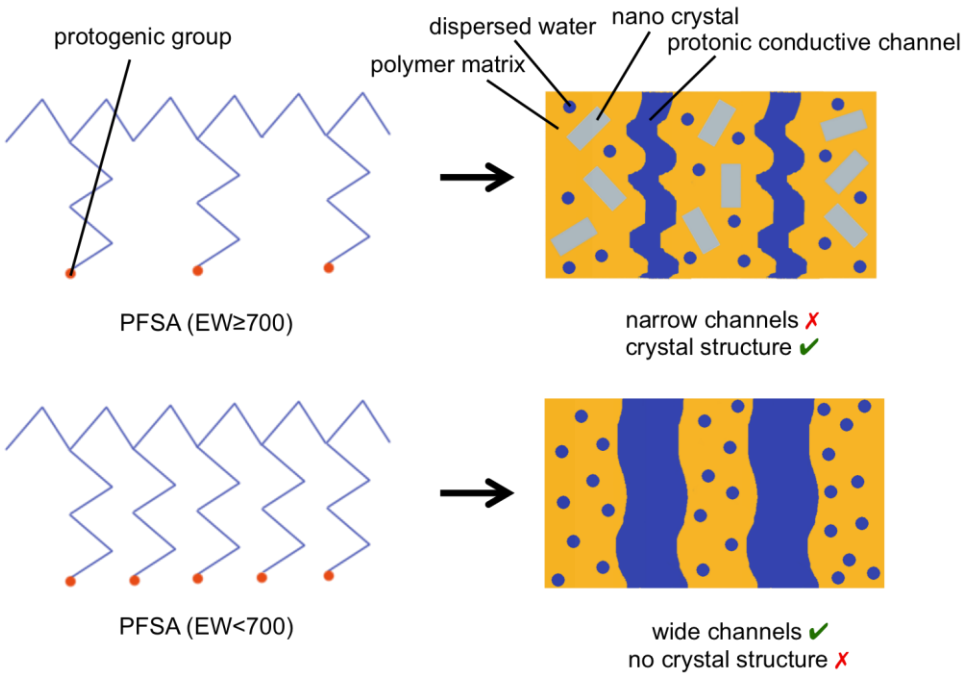

a

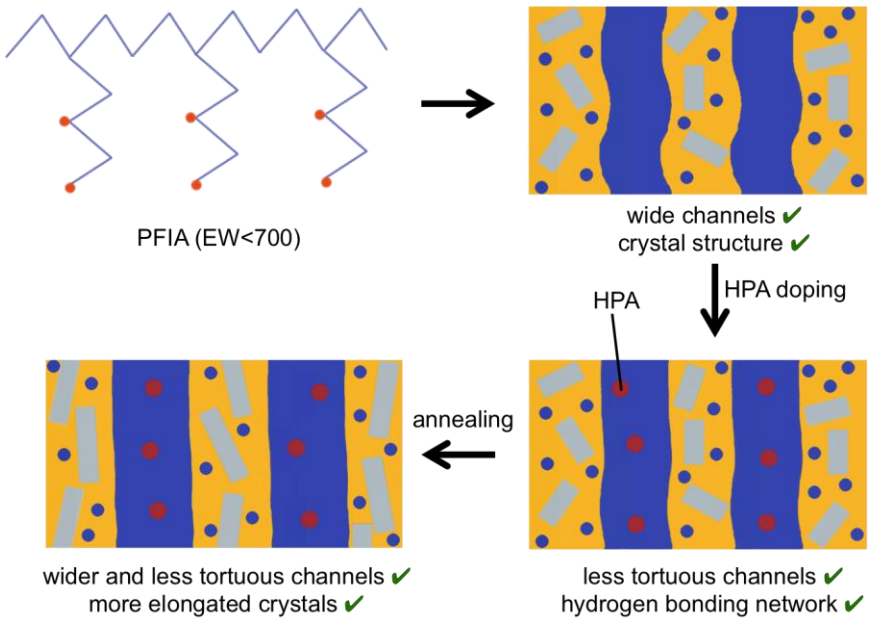

b

Figure 6.1 Structure-morphology relationship of PEMs based on 3M PFSA (a) and 3M PFIA (b), and the effect of HPA addition and annealing to 3M PFIA's morphology (b).

provide sufficient mechanical strength. This selected PEM then will be treated with HPA addition and annealing, to tune its morphology and improve its performance (figure 6.1b). When HPAs functionalized with vinyl groups are incorporated into the PFIA ionomer system, the water soluble HPA moieties are immobilized[2] which further improves the conductivity and water retention capability of the membrane under hotter conditions. An interconnected hydrogen bonding network within the ionic conductive channels can be obtained through this HPA addition. These channels can also be made more homogeneous and less tortuous with an optimal HPA loading (5% for HPW from our current study on 3M PFSA). The last step to further improve the membrane performance is thermal treatment. We already demonstrated in the present work that annealing of PFSA at elevated temperatures is able to improve conductivity through inducing morphological change and making wider ionic domains. The ideal annealing temperature based on our present study of 3M PFSA films is 200 °C.

6.5.2 Approach B: Hydrocarbon-Based Material

This approach is schematically shown in Figure 6.2. A PFIA side chain[1] can be incorporated to hydrocarbon backbone to make hydrophilic blocks. A multiblock copolymer with blocks of hydrophobic component copolymerized with hydrophilic blocks creates the desired effect of a higher degree of phase separation.[3] Such a phase separated morphology is desirable for protonic conduction and dimensional stability. HPAs can also be incorporated and immobilized[2] in this system to create an interconnected hydrogen bonding network within the ionic conductive channels, and hence to facilitate proton transported through Grotthuss hopping mechanism. Besides the improvement of conductivity and water retention capability, HPA can also improve the oxidative stability of the polymer.[4] Thermal annealing of these multi-block

hydrocarbon ionomers is not practical due to their high glass transition temperature and lower desulfonation temperature compared to PFSA.

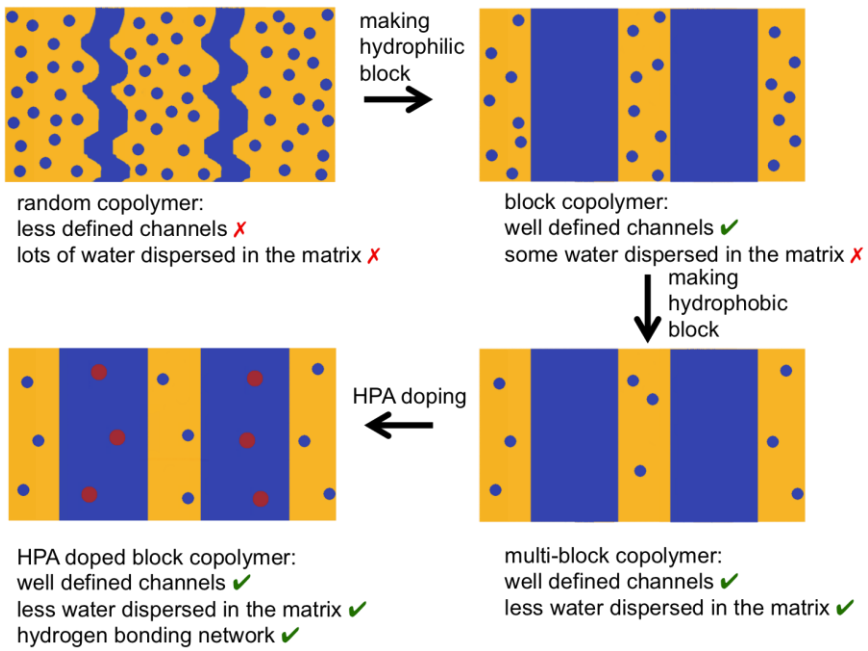

Figure 6.2 Structure-morphology relationship of new PEM based on hydrocarbon materials, and the effect of HPA addition.

6.6 References

(1) Schaberg, M. S.; Abulu, J. E.; Haugen, G. M.; Emery, M. A.; O'Conner, S. J.; Xiong, P. N.; Hamrock, S. J. *Polymer Electrolyte Fuel Cells 10, Pts 1 and 2* **2010**, *33*, 627.

(2) Herring, A. M.; Horan, J. L.; Kuo, M. C.; Dec, S. F.; Frey, M. H.; Genupur, A.; Ren, L.; Yandrasits, M. A.; Hamrock, S. J. *Proton Exchange Membrane Fuel Cells 8, Pts 1 and 2* **2008**, *16*, 699.

(3) Peckham, T. J.; Holdcroft, S. *Adv Mater* **2010**, *22*, 4667.

(4) Haugen, G. M.; Meng, F. Q.; Aieta, N. V.; Horan, J. L.; Kuo, M. C.; Frey, M. H.; Hamrock, S. J.; Herring, A. M. *Electrochemical and Solid State Letters* **2007**, *10*, B51.

APPENDIX A A COMBINED COMPUTATIONAL AND EXPERIMENTAL EVALUATION OF THE STRUCTURE AND MORPHOLOGY OF A $H_3PW_{12}O_{40}$ DOPED PERFLUORO SULFONIC ACID PROTON EXCHANGE MEMBRANE

Reproduced from a paper submitted to *J. Phys. Chem. C. Unpublished work copyright ACS 2014.*

Somisetti V Sambasivarao,[†, §] Yuan Liu,[†, §] James L Horan,[†] Andrew M Herring,[†,*] C Mark Maupin[†,*]

A1 Abstract

The impact of heteropoly acid (HPW) loading on a perflurosulfonic acid (PFSA) polymer exchange membrane's morphology was evaluated by means of molecular dynamics (MD) simulations and small angle X-ray scattering (SAXS) experiments. It is found that the addition of HPW significantly modifies the solvent structure and dynamics in the PFSA membrane. It is hypothesized that the HPW induced solvent modifications account for the enhanced proton conducting characteristics of these doped membranes by enhancing the formation of interconnected proton conducting water network. Radial distribution functions and water cluster analysis indicate that HPW organizes the solvent water while attracting excess protons thereby creating nodes to which water wires/channels connect resulting in a more efficient proton conducting network. This redistribution of solvent and hydronium ions upon addition of HPW creates a shift in the pore size distribution and the overall membrane morphology. Pore size analysis indicates that a high percentage of small pores (d < 15 Å) exist in low HPW doped

[†]Department of Chemical and Biological Engineering, Colorado School of Mines, Golden, Colorado 80401, United States

[*]Corresponding Authors

[§]These authors contributed equally.

systems (*i.e.* 1%), while larger pores (d > 15 Å) exist for the high HPW doped systems (*i.e.* 5%). At low hydration levels the water domains are found to be spheroidal inverted micelles embedded in an ionomer matrix, while at high hydration levels the solvent morphology shifts to a parallel spheroidal elongated cylinder. It is also observed that for the high HPW doping levels the SAXS pattern changes intensity at the low q region and Bragg peaks become present, indicating the presence of crystalline HPW. These morphological changes create a more interconnected pathway through which the hydrated excess protons may transverse thereby enhancing the PFSA membrane's conductivity.

A2 Introduction

Polymer electrolyte membrane fuel cells (PEMFCs) have been studied since 1960,[1] due to their promising characteristics as a power conversion device. For durability reasons, the Perflurosulfonic acid (PFSA) polymers are a populer proton exchange membranes (PEM) used in the electrode assembly of PEM fuel cells, where they serve as the protonic conductor.[2,3] PEMFCs electrochemical devices have attracted significant attention due to their high power densities, high efficiency, and non-polluting exhaust, which makes them suitable for portable, transportation, and stationary uses.[4] Extensive studies have been performed on benchmark PFSA PEMs such as Nafion^{TM}, Aquivion^{TM}, and the 3M ionomer for fuel cell applications. [5,6, 7,8] However, there is still an insufficient fundamental understanding, at the molecular-level, of the water structure and the impact of dopants on these critically important membranes.

Although PFSA polymers can achieve high conductivity when hydrated, their performance is hindered by their poor water retention characteristics, which is exacerbated at higher temperature and drier operation conditions.[9] The loss of water from the polymer at high

temperatures results in a dramatic decrease in the conductivity of the fuel cell. Unfortunately, it is favorable for fuel cells to operate at high temperature in order to enhance heat transfer and decrease the poisoning of the Pt catalyst by CO adsorption and lower RH to eliminate unit operations associated with water management. Therefore, the development of ionomeric membranes capable of operating at higher temperature and lower RH is greatly needed. Several strategies have been adopted to achieve this objective, such as the addition of inorganic super-acids (*e.g.* Heteropoly acids (HPA), and zirconiumphosphonates) that have been shown to enable films to achieve high conductivity at elevated temperature.[9-17] HPAs have become one of the most promising additives to improve the conductivity of PEMs under drier and hotter conditions, due to their high ionic conductivity in the solid state, favorable interactions with the ionomer, ability to increase the local proton concentration, and their favorable impact on forming hydrogen bonding networks.[17]

In order to fully understand the performance and properties of PFSAs and hybrid materials made from them, it is imperative that there is a molecular-level understanding of the PEM's morphology at various hydration levels. Although the hydrophobic/hydrophilic phase separated structure is generally accepted, the exact morphology of PFSAs is a subject of debate, due to the variation in materials synthesis techniques, and experimental conditions. Small angle X-ray scattering (SAXS) techniques have been used to study numerous PFSA films,[18-28] resulting in a number of proposed morphological models, such as the cluster network model, the core−shell model, the lamella model, and the parallel cylindrical channel model.[19-22] It is commonly accepted that the morphology of PFSAs vary depending on the hydration levels. Gebel *et al.* suggested that at moderate to low hydration levels the PFSA membranes possess an inverted micellar structure embedded in the ionomer, while at hydration levels greater than 50%

the membranes are hypothesized to become more ordered structures consisting of rod-like polymer crystallites.[25] Other notable studies including that of Elliott *et al.* obtained the 2D reconstruction of the ionic domain network of Nafion^{TM} using a maximum entropy method,[26] while Aeita *et al.* used both a unified fit and a clipped random wave (CRW) methods to analyze SAXS data of 3M ionomer films thereby obtaining size information of the ionic clusters and the crystal domains.[23] In our previous study, we investigated the dynamic morphological changes of the 3M ionomer upon hydration and annealing using in-situ dynamic SAXS measurement, and found the phase transition behaviour between the amorphous and crystal domains.[24] In addition to experimental investigations, there have been several simulation studies on PFSA films,[29-35] including Wu *et al.* who used dissipative particle dynamics simulations to examine the morphology of the 3M membrane, which are in good agreement with SAXS findings by Aeita *et al.*[29, 23] In order to study the role of connectivity of adjacent pendant groups of the 3M ionomer, Paddison *et al.* used first principle calculations on fragments of the short side chain (SSC) PFSA ionomer and they concluded that water binding to the sulfonate functional group is favored only after the proton dissociated from the pendant, and increasing the side chain separation requires more waters to form hydrogen bonded networks between $–CF_2$ units.[30] In an MD study carried out by Sunda *et al.* on Dow's Aciflex and Nafion, it was found that side chain size directly impacts the nanostructure and properties of the polymer. Shortening the side chain length was found to have minimal impact on the structure or morphology of the water domains[31], while adding multiple $–CF_2$ units was found to induce additional phase segregation and resulted in a more rigid polymer.[32, 33]

Despite the extensive morphological studies that have been performed on PFSA films, there has no been a detailed MD study conducted on the HPA doped PFSA 3M films. In our

recent work,[36] we studied the transport properties of HPA doped 3M ionomer films, through experiment and simulation. In this work, we utilize experiment and simulation to investigate the detailed morphology of the water structures in an effort to better understanding the impact of doping PFSA's with HPA has on the morphology and the proton transport properties. In this study we used long time all atomistic molecular dynamics (MD) simulations and small angle x-ray scattering (SAXS) experiments to elucidate the detailed structural and dynamic properties in the 3M polymeric system at various water contents (λ=5, 9, and 14) and HPA loadings (0, 1, and 5%). This work represents the first all atomistic molecular dynamics simulations and SAXS experiments, which probe the morphological impact of adding 12-phosphotungstic acid, $H_3PW_{12}O_{40}$ (HPW), to the PFSA functionalized 3M polymer

A3 Methods

Details about experimental materials, SAXS measurement and molecular dynamics simulations are provided in this section.

A3.1 Materials

3M 825EW PFSA ionomer was doped with 1 wt% and 5 wt% HPW, and annealed at 180 °C for 10 min. The detailed procedure to prepare the study material is described in our previous work.[36]

A3.2 Molecular Dynamics Simulations

The 825 equivalent weight (EW) of 3M ionomer was described using the DRIEDING,[37] and recent study[33, 34] force field potential as it has successfully been utilized to study similar types of PFSA polymers. The force field parameters for HPW were taken from Brodbeck *et al.*[38] while the flexible 3-centered (F3C)[34, 39] force field was used to represent the waters and the classical hydronium ions. The 3M polymeric systems were generated using a dynamic structure creation code[40] resulting in an entangled polymer system at the experimentally determined density. The resulting systems consisted of 64 polymers with each polymer containing 10 monomers. Equivalent numbers of hydronium ions to sulfonate groups were added to ensure system neutrality. The resulting systems were then doped with 0, 1, or 5% (w/w) HPW nanoparticles. Three hydration levels corresponding to λ= 5, 9, and 14 were then created for the pure and doped 3M ionomer systems for a total of 9 systems. All molecular dynamics simulations were conducted using the LAMMPS software code.[41]

The 9 systems were initially heated to 400 K and simulated for 5 ns in the iso-thermal iso-baric ensemble (NPT) at 1 atm to achieve mixing of the entangled polymer strands, water, hydroniums, and HPW nanoparticles when present. The initial high temperature NPT simulations were then followed by a set of 5 ns NPT ensemble simulations at 300 K and 1 atm to cool down the systems. The density of the system was then evaluated using the box dimensions at the end of the 5 ns cool down simulation. The heat-cool cycle outlined above was repeated until the measured density of the system was within 5% of the experimentally determined density. The resulting systems were then subjected to 20 ns of equilibration in the canonical ensemble (NVT) at 300 K followed by a 20 ns production simulation conducted in the micro-canonical ensemble (NVE).

To evaluate the morphology of the ionomer system the ImageJ software, which is widely used for medical and engineering purposes, was used to analyze various snapshots of the simulations.[42-44] The images were generated for slices through the simulation box that were spaced 6 Å apart along one of the primary (*e.g.* x, y, or z) axis of the simulation box using the Visual Molecular Dynamics (VMD) software.[45] The diameter of the water oxygen atom (*i.e.* the effective water sphere) in the images was set to 2.8 Å as determined by Murata *et al*.[46], which enabled the calculation of the hydrophilic domain size. The images generated by VMD were then imported and analyzed by the ImageJ software. The error bars, when appropriate, were calculated using images generated at every 100 ps intervals over the last 2 ns of the trajectory. The errors in the distributions of pore size for all system types were estimated to be less than 1% of the reported values.

A3.3 SAXS Measurement

SAXS experiments were performed using the synchrotron radiation source at the Argonne National Laboratory's, (Argonne, IL) beamline (12ID C-D of the Advanced Photon Source (APS) using X-rays of 18 keV). Details of the experimental setup can be found in our previous work, therefore only a brief explanation will be given here.[24] SAXS measurements with humidification levels of 25%, 50%, 75% and 95% relative humidity (RH) were performed on films with different HPA loadings. For each experiment, the oven was first set to 25%RH and 3 SAXS patterns were taken for the films and 1 pattern for the Kapton™ background. The humidity was then increased to 50%RH, and the SAXS patterns were recoded after 20 minutes equilibration time. This procedure was repeated for each hydration level from 25%RH to 95%RH. In order to make it comparable to data obtained from simulations, which is in terms of

λ, we convert our experimental data from RH to λ based on the water sorption isotherm measured by DVS.

A4 Results and Discussions

Important results obtained through both simulation and SAXS measurements pertaining to film morphology at various hydration levels are discussed in great detail below.

A4.1 Density

The densities of the hydrated 3M composites at 300 K for the three λ's simulated are shown in Table1, and are in good agreement with recently published work.[33] It is observed from simulations that the density of the pure and HPW doped 3M systems gradually decrease as λ increases closely matching the experimentally measured density (within 5% error). Upon loading

Table A1 Densities for pure and HPW doped 3M ionomer systems

3M Systems hydration level (λ)-% HPW	$Density_{Simulation}$ (g/cm^3) 300 K	$Density_{Exptl.}$ (g/cm^3) 300 K	$Density_{Simulation}$ (g/cm^3) 353 K
0%HPW-5WAT	1.77	1.8	1.72
0%HPW-9WAT	1.69	1.64	1.64
0%HPW-14WAT	1.54	1.47	1.54
1%HPW-5WAT	1.70	1.65	1.64
1%HPW-9WAT	1.64	1.53	1.57
1%HPW-14WAT	1.55	1.39	1.54
5%HPW-5WAT	1.84	2	1.79
5%HPW-9WAT	1.74	1.84	1.63
5%HPW-14WAT	1.65	1.64	1.59

of HPW from 0% to 1% (w/w) the density decreases slightly while additional HPW loading from 1% to 5% (w/w) resulted in an increase in the density of the simulations in good agreement with experimental measurements. We hypothesized that the change in density is due to morphological changes induced by the addition of HPW as discussed in section 3.2.

A4.2 Structure of the undoped and HPW doped 3M ionomer systems

The morphology of the undoped and HPW doped 3M ionomer systems with various HPW loading and hydration levels were analyzed through simulation and SAXS experiment. In the following sections a detailed discussion of the radial distribution functions, nanophase segregated hydrophilic domains, and SAXS data is presented.

A4.2.1 Structural Properties of Sulfonic Acid Side Chain Pendants

For all doping levels it is found that as λ levels increase the distance between neighboring sulfonic acid groups increases, as seen in Figure A1. The increase in the hydration level enables more waters to solvate the sulfonic acid groups resulting in an increased separation distance between sulfonic acid groups, which is a result also seen in Nafion (*i.e.* swelling). For the undoped 3M systems, as λ increases, the peak height decreases, and become broader resulting in a decrease in the number of neighboring sulfonic acid groups. The increased solvation results in the elimination of the side-chain structure seen at the lowest hydration level (*i.e.* structure between S-S distance of 4 and 8 Å). Upon doping of 1%HPW, the S-S RDF shows a similar trend as seen in the undoped 3M systems with the peak broadening at higher λ values although, the decrease in amplitude between 5λ and 9λ is not as pronounced as in the pure 3M system. The difference between pure 3M and doped systems is attributed to the presence of the highly

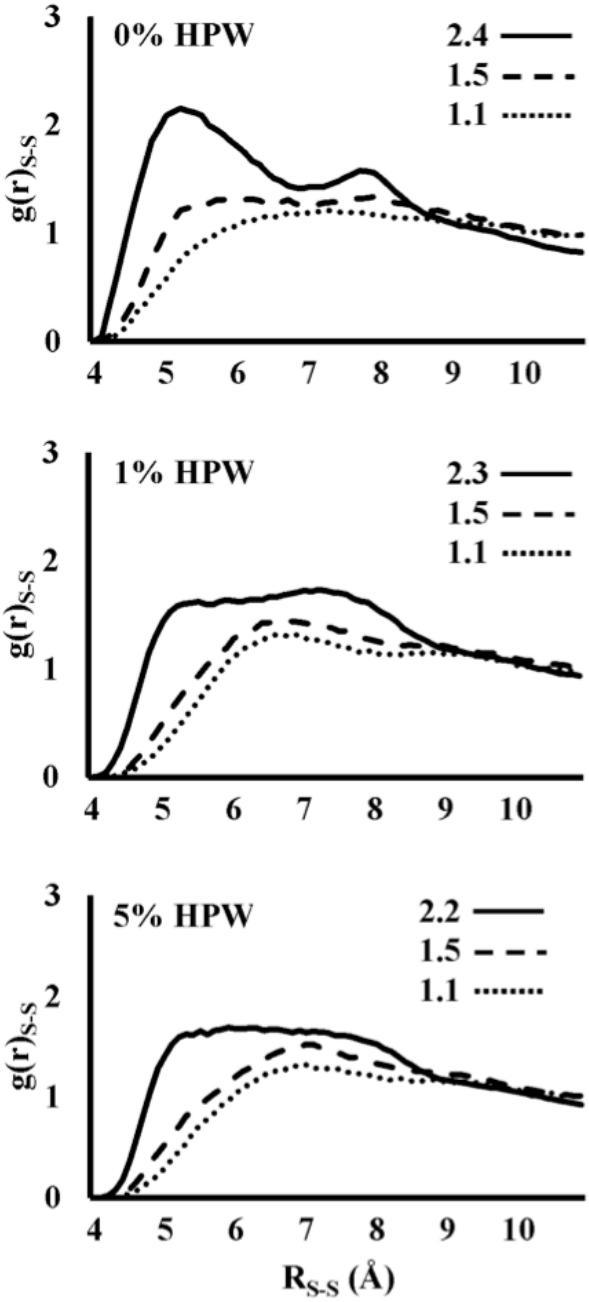

Figure A1 Radial distribution functions between the sulfonate sulfurs a function of the hydration level, 5λ (—), 9λ (---) and 14λ (¨). The coordination numbers for the first peak (*i.e.* 0 to 7.0 Å) are shown in the top right of each graph.

charged HPW particles, which is found to disrupt the sulfonate group structure at low λ. For HPW loadings increasing from 1% to 5%, there is no noticeable difference in S-S peak height or the separation distances. It is observed that at high λ all systems appear to loose S-S structure although the addition of HPW does seem to slightly shift the first peak to larger S-S separation distances. This observation is most likely due to the unfavorable repulsion between the HPW and the sulfonic acid groups. The observed structural changes including the movement of sulfonate side chain pendants when λ levels are increased and/or upon addition of HPW loadings suggesting that there is a significant shift in the hydrophilic domain morphology. In addition to the morphological changes we also observed a change in the dynamical movement of sulfonate pendant chains upon modifying λ and HPW loadings (unpublished data) as previously reported in the literature.[47]

A4.2.2 Proton Solvation Environment for Sulfonic Acid Side Chain Pendants

The interactions between sulfonate side chain pendants and the hydronium ions (Figure A2) reveals information about the solvating structure of the hydronium ions around the sulfonic acid side chain pendants in the 3M ionomer. Figure A2 indicates that as the hydration level increases the amplitude of the first peak decreases along with the observed occupancy number for the first solvation shell. As was seen in Figure A1, increasing λ levels leads to more waters solvating the sulfonate groups. The solvated sulfonate groups are then pushed away from each other, while at the same time the hydroniums ions move farther away from the sulfonate groups in favor of increasing their solvation by water. It is noted that while the first solvation shell amplitude decreases there is relatively little impact on the structure of the second solvation shell,

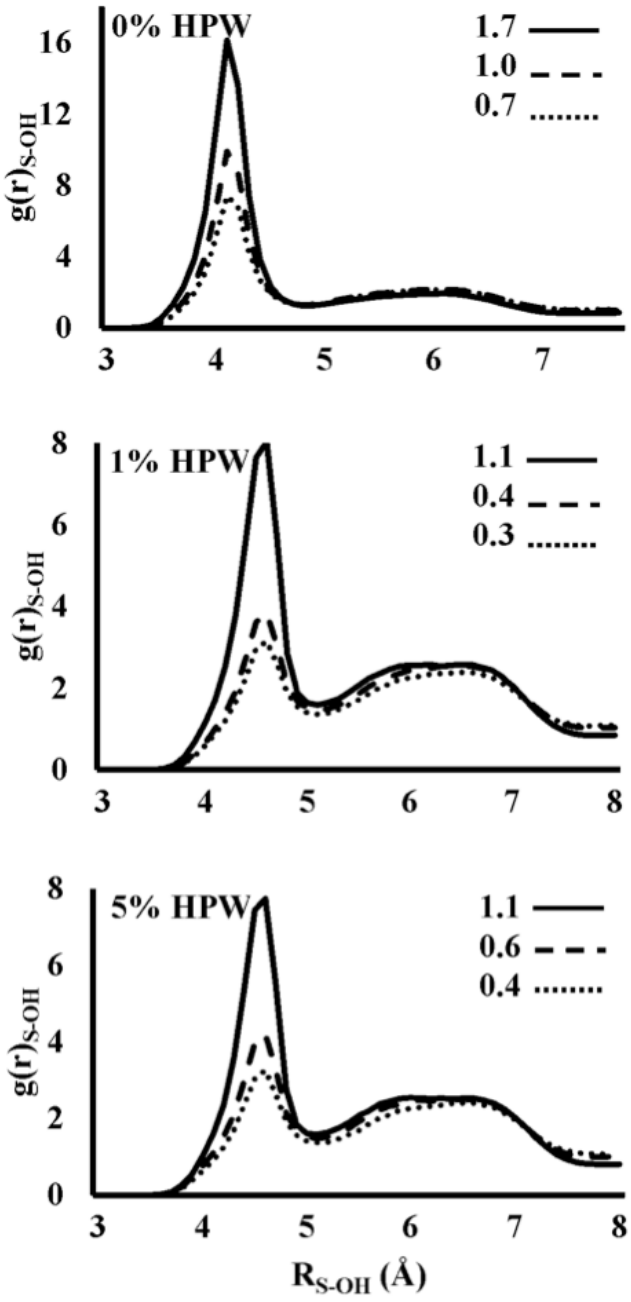

Figure A2 Radial distribution functions between the sulfonate sulfur atoms and the hydronium oxygens (*i.e.* Eigen cation) as a function of the hydration level, 5λ (—), 9λ (---) and 14λ (¨). The coordination numbers for the first peak (*i.e.* 0 to 4.7 Å) are shown in the top right of each graph.

which has a broad distribution between 5 to 7 Å away from the sulfonic acids sulfur atoms. Although the structure does not significantly change the small increase in amplitude and occupation number indicate that the hydroniums that moved out of the first solvation shell now resides in the second solvation shell. On addition of HPW to the 3M ionomer systems, the peak height is found to be significantly lower as compared to the undoped systems. The decrease in the peak height upon addition of HPW indicates that the hydronium ions are displaced from the water domains around the sulfonic acid groups and now reside in a more favorable environment near the HPW nanoparticle. The displacement of hydronium ions occurred due to the stronger electrostatic interaction between the hydronium ions and the highly charged HPW particles. Upon additional loadings of HPW it is found that the overall solvation structure is not significantly perturbed.

A4.2.3 Water Solvation Environment for Sulfonic Acid Side Chain Pendants

The RDFs between the sulfonate pendants and the solvating waters (Figure A3) reveals that while the amplitude of the first peak decreases with increasing λ the number of waters in the first solvation shell increases (*i.e.* due to the increase in total system water density). The absence of a second peak or other features at larger separation distances indicates that there is no long range structural order to the solvating waters. Together, Figure A2 and Figure A3 indicate that at high λ the waters displace the hydronium ions in the first solvation shell around the sulfonate pendant groups resulting in a more solvated sulfonate group. The displaced hydroniums, which are observed to move to greater distances, can now maximize their solvation energy. Upon addition of HPW, it is observed that the first solvation shells amplitude at low λ significantly increases. This increase in amplitude at low λ and the moderate increase at 9λ indicate that

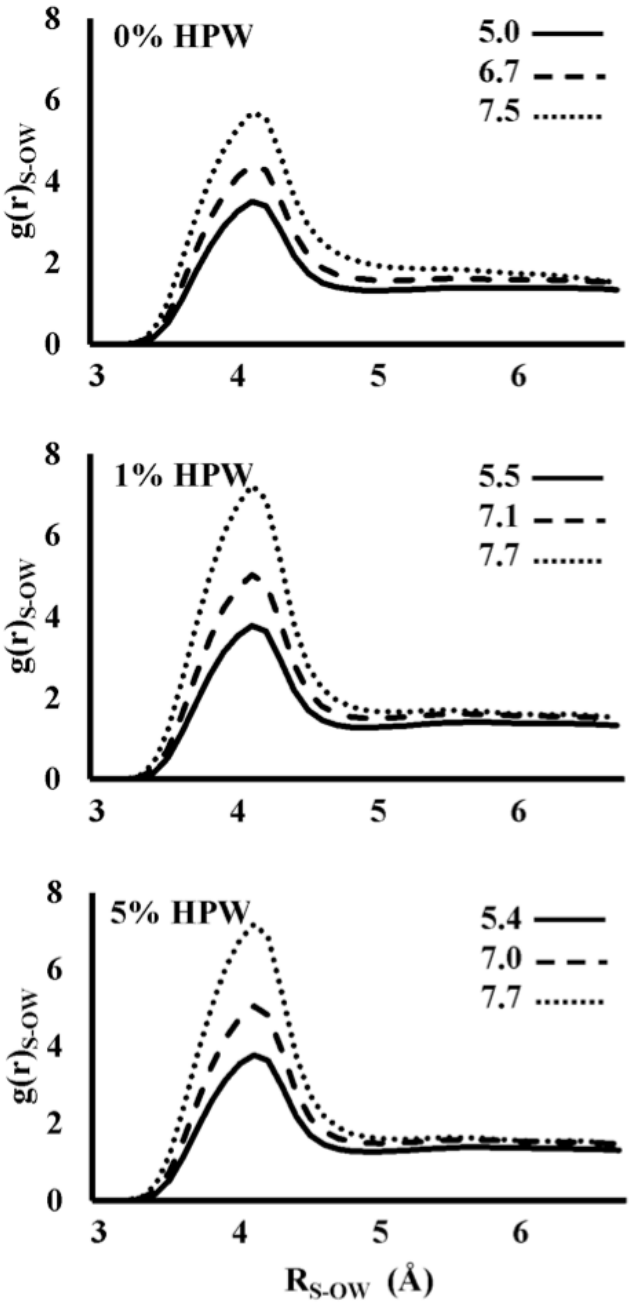

Figure A3 Radial distribution functions between the sulfonate sulfur atoms and the solvating water oxygens as a function of the hydration level, 5λ (—), 9λ (---) and 14λ (¨). The coordination numbers for the first peak (*i.e.* 0 to 4.7 Å) are shown in the top right of each graph.

addition of HPW enhances the solvation of the sulfonate groups as the hydroniums are preferentially attracted to the HPW nanoparticle. Additional loading from 1% to 5% HPW (w/w) does not change the shape or the coordination number of the first peak. As was the case with the undoped 3M ionomer, increasing hydration levels result in an increase in the number of waters in the first solvation shell around the sulfonate groups and a decrease in the amplitude of the first peak.

A4.2.4 Solvation Characteristics of the Protons and Waters around HPW

The RDFs depicting the interactions between the HPW nanoparticles, the hydronium ions, and the solvating waters are presented in the Figure A4. The RDFs confirm our hypothesis that the hydronium ions are attracted to the highly charged HPW nanoparitcles. The distribution functions reveal that upon adding HPW from 1% to 5% (w/w) to the 3M ionomer system there is a significant increase in the peak height for the HPW to hydronium RDF (*i.e.* terminal oxygen of HPW and oxygen of the hydronium ion). This result indicates an increased number of hydronium ions coordinated in the first solvation shell of the HPW. A complete picture for the redistribution of hydronium and solvating waters upon addition of HPW is now possible when taking into account the previous RDF results. It is observed that a significant decrease in the hydronium ion coordination number (Figure A2) and an increase in water coordination number (Figure A3) for the sulfonate groups upon addition of HPW, with the hydroniums migrating to the HPW nanoparticles. At 5λ, it is observed that as the doping level of HPW increases from 1% to 5% (w/w) the hydronium ions found in the first solvation shell increases while the numbers for water in the first solvation shell decreases. These results indicate that there is a competition between the hydronium ions and solvation waters surrounding the HPW nanoparticle. Inspection of the

HPW solvation structure reveals the presence several repeating peaks (Figure A4). These peaks are due primarily to the structure of the nanoparticle, with the repeating peaks originating from the waters located in the first solvation shell at various sites/locations on the nanoparticle. Due to the overall fixed structure with a ~10 Å diameter, ~2.7 Å between terminal oxygen's and connecting oxygen's (*i.e. via* metal atoms), and the repeating terminal oxygen's at ~ 5, 9, and 10.5 Å, the peaks around 5, 9, and 10 Å in the HPW-OW RDF are primarily due the solvating waters at these distant oxygen centers (*e.g.* the other side of the particle).

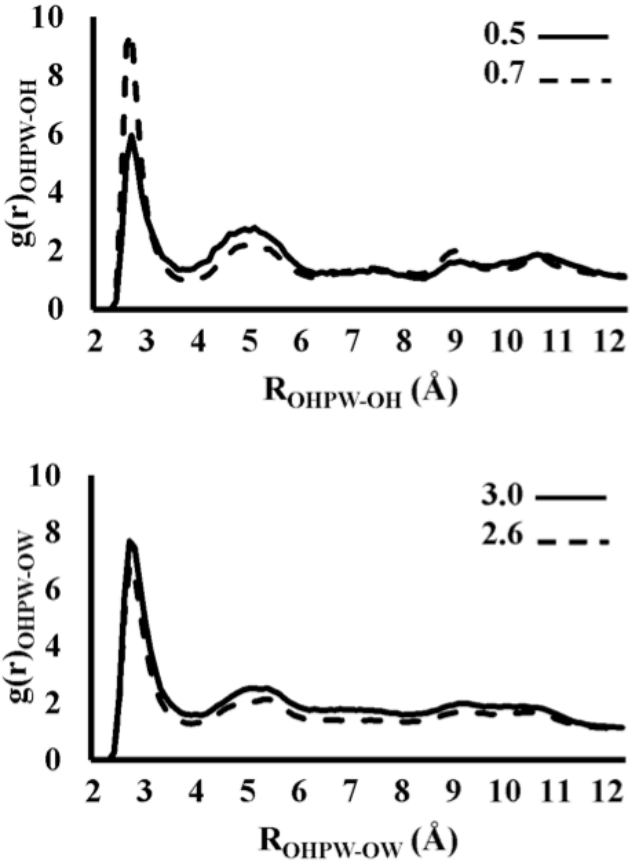

Figure A4 Radial distribution functions between the HPW's exterior oxygens and the solvating water or hydronium oxygens at the 5λ hydration level. 1% HPW(—) and 5% HPW(---) are depicted for the surrounding hydroniums (Top) and solvating waters (Bottom). Coordination numbers for the first peak (*i.e.* 0 to 4.0 Å) are shown in the top right of each graph.

A4.2.5 Structure of 3M Ionomers from SAXS

In our previous studies,[23,24] we have investigated the phase separated morphology of the 3M ionomer with general morphological information such as size and shape for different hydration levels. In this work we will further discuss the morphology of both pure 3M ionomer films and the hybrid films doped with HPW as observed from SAXS. For the 3M control, we can see 3 distinct features, *i.e.*, the so-called ionomer peak at high q (q=0.1 to 0.4 $Å^{-1}$), which is formed by the ionic clusters, the crystalline knee in the intermediate q range (q=0.01 to 0.15 $Å^{-1}$), which is formed by the polymer backbones, and an ultra-small angle upturn (q<=0.01 $Å^{-1}$). Figure A5 shows the impact of water uptake on the morphology of 3M and doped films. It is observed that as relative humidity increases, the ionomer peaks shift to lower q, with an increase in intensity. Regardless of the different morphological model proposed, this change in the SAXS pattern is an indication of the increase in abundance and size of the hydrophilic region as a result of water uptake and swelling. The polymer swelling results in the increase of inter- connectivity of water conductive channels and the reduction of 'dead-pockets'. The D-spacing of the ionic clusters at different RHs was calculated from the ionomer peak positions and reported in Figure A6. At λ=5 it is found that there is little effect on the D-spacing when HPW is added. However, as the water content increases, the impact of HPW becomes more pronounced with the 5% HPW dramatically increases the D-spacing at both λ=9 and λ=14. This indicates that when a sufficient amount of HPW is present, they can bridge the hydrophilic domains and increase the center-center distance between these domains (*i.e.* the D-spacing). We noticed that 1% HPW loading decreased the D-spacing especially at λ=14, we hypothesize that at this loading level, HPW particles are not capable of bridging separated domains. Instead, they created more isolated domains with the water molecules forming a hydration shells around the nanoparticles, which

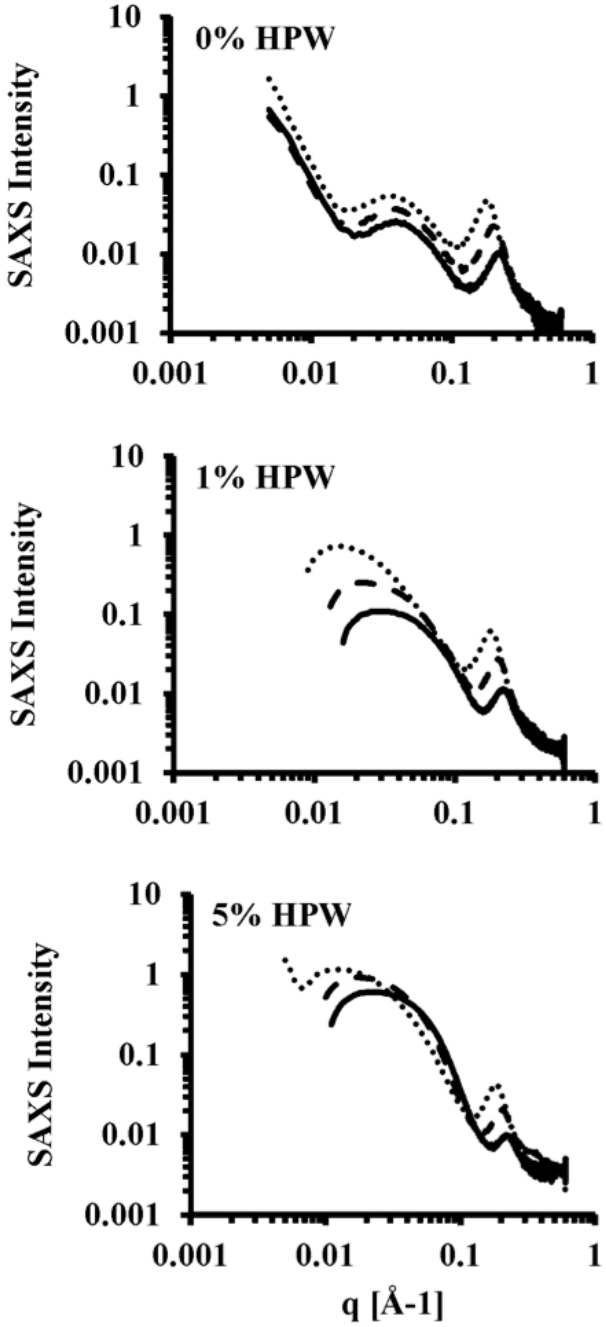

Figure A5 SAXS patterns for pure 3M and films doped with HPW as a function of thevhydration level. 25% RH (—),75% RH (---), 95% RH (¨) for the 0% HPW control (Top), 1% HPW (Middle), and 5% HPW (Bottom).

results in a decrease in the D-spacing. This morphological information has provided insights into the phenomena of proton diffusion and conduction as discussed in our recent report on the diffusion characteristics of the HPW doped 3M polymer.[36] Additional inspection of the SAXS data reveals a Bragg peak in the very large q region (q=0.4 to 0.6 $Å^{-1}$), which corresponds to a D-spacing of ~10 Å in the HPW doped systems and the presence of HPW crystals in the film. It is observed that as the films become wetter, the Bragg peak becomes broader, which indicates that the crystal structure of HPW is disturbed by water uptake and becomes less ordered.

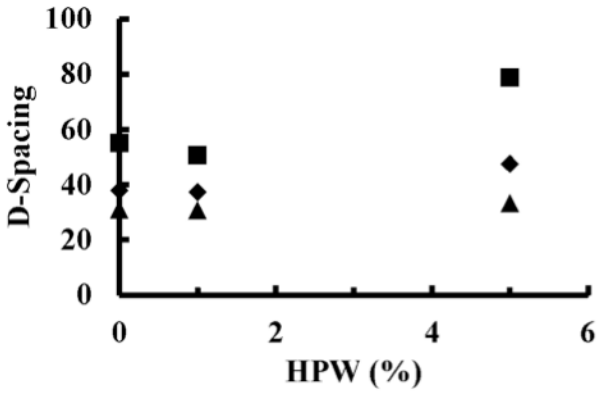

Figure A6 D-spacing calculated from ionomer peak. (▲) λ=5, (◆) λ=9, and (■) λ=14.

A4.3 Morphology of Pure and HPW Doped 3M Ionomer Systems

Snapshots of the hydrophilic domains and HPW in the simulated 3M ionomer systems are shown in the Figure A7 and the average number of hydrophilic domains as a function of the λ value for all systems is reported in Figure A8.

A4.3.1 Nanophase Segregation

It is evident from Figure A7 that at low λ the hydrophilic domains consist of isolated clusters, while at the high λ values there is a continuous water domain. In the 3M ionomer the proton conduction occurs through the hydrophilic domains that connect the sulfonate groups present in the polymer. The addition of HPW to these ionomer systems induces changes to the structure of the hydrophilic domains, which become more pronounced with higher loadings of nanoparticles.

A4.3.2 Structure of the Hydrophilic Domains

Inspection of Figure A8 reveals that the number of hydrophilic domains decreases as λ increases with no statistical difference between pure and doped systems. The decrease in the number of hydrophilic domains is due to the merging of water clusters, which results in larger water clusters at higher λ values, as determined by an increase in the Feret's diameter for the clusters. The calculated average Feret's diameter for the hydrophilic domains ranged from 13 Å to 26 Å in good agreement with previously published results.[18, 22, 47-48] Moreover these water domains were found to be "inverted micelles" embedded in the 3M ionomer matrix. As the hydration level increases, the water channels become continuous, a more indicative of a bulk environment. The length of the inverted micelle at high λ was observed to increases from a range of 10 to 30 Å (5λ), to 20 to 60 Å (9λ), and finally to a range of 60 to 90 Å (14λ). Throughout the range of hydration levels the morphology of the hydrophilic domains (*i.e* water channels) was found to change from small isolated inverted micelle at a low λ level to aggregates of water channels and finally to lengthy elongated water channels at higher λ levels. However, the

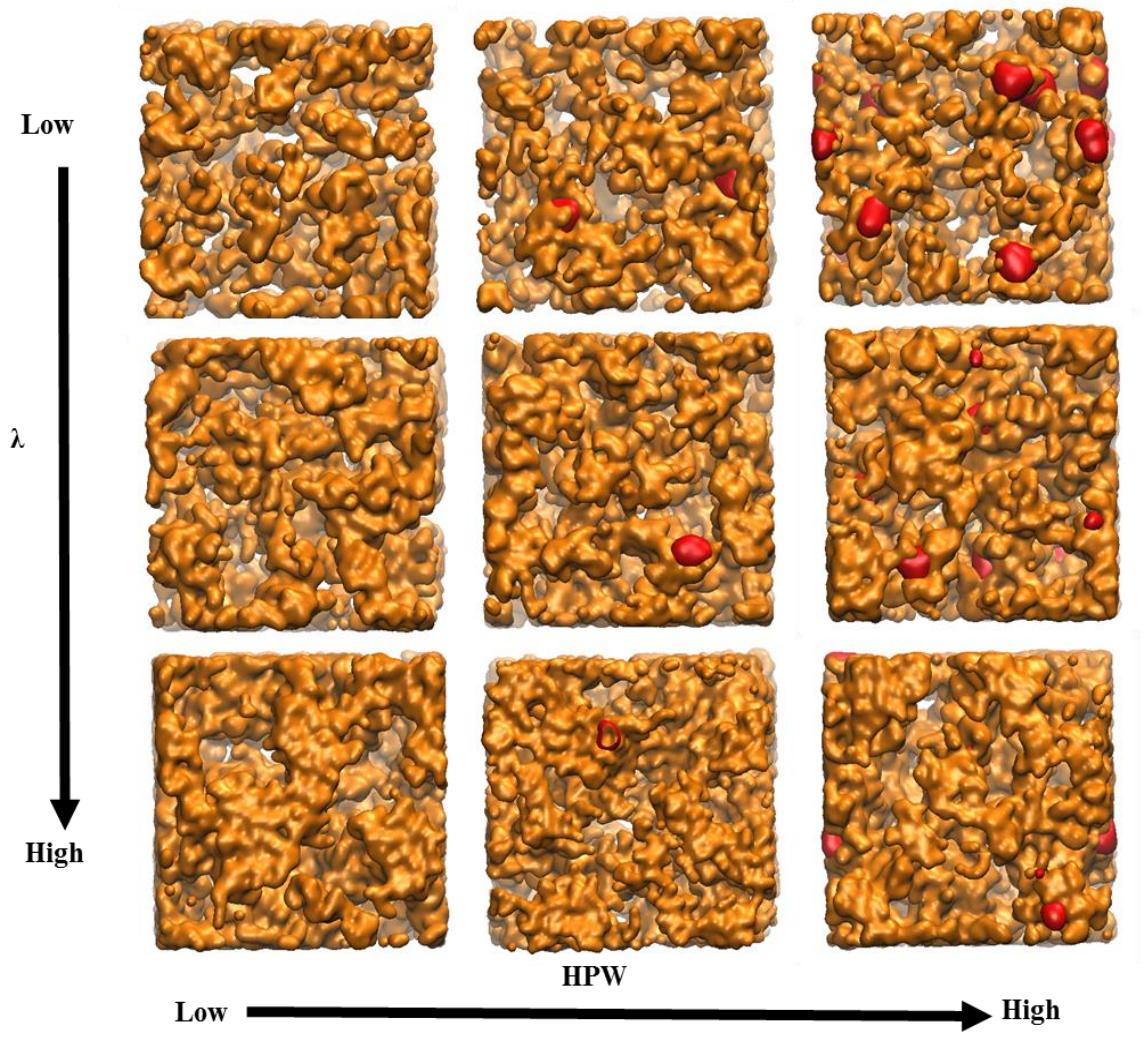

Figure A7 Snapshot of pure and HPW doped 3M ionomer systems at various λ levels. Hydophilic domains are represented by orange surface while the HPW nanoparticle is represented by the red surface. The ionomer systems not shown for clarity purposes.

addition of HPW to perturbed this trend by producing a large number small domains < 15 Å at low HPW doping, and large domains > 15 Å at high HPW doping. Evaluation of the distance between the center of mass for the identified water clusters indicates an average separation distance of between 20 to 40 Å at low hydration levels (data not shown), which is in good agreement with the values measured using SAXS (Figure A5). In addition to the number of clusters and their average separation distance, the shape of the hydrophilic domains was also evaluated by using the circularity algorithm in the ImageJ software. The circularity for the low λ systems was found to be in the range of 0.6 to 0.7 (*i.e.* perfect circle is 1). This analysis indicates that the water domains at high λ levels are parallel to each other creating efficient pathways for the transport of hydronium ions. The general shape of the hydrophilic channels is best described as an inverted micelle at low λ that changes to parallel spheroidal cylindrical channels at high λ levels. Our observation and analysis from this study is consistent with the results presented by Schmidt-Rohr *et al.*,[22] Brandell *et al.*,[47] Gierke *et al.*,[48] and Gebel *et al.*[25].

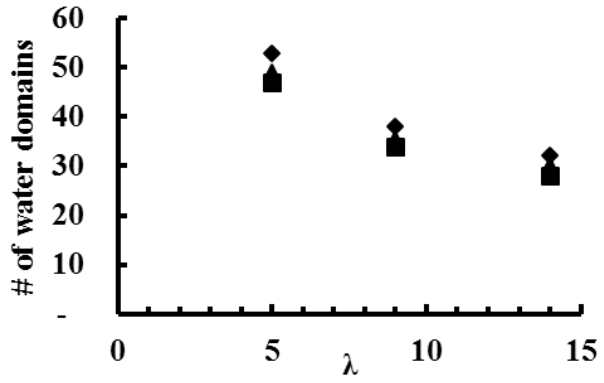

Figure A8 Number of hydrophilic domains as a function of the hydration level for (▲) 0%, (◆) 1%, and (■) 5% HPW doped systems (Error bars: ±6).

A5 Conclusions

MD simulations and SAXS were performed on the 3M membrane to elucidate the solvation structure and system morphology for pure 3M and HPW doped ionomer systems. The RDFs and coordination numbers revealed that the hydronium ions strongly interact with the HPW nanoparticles, disrupting the native hydrophilic domains seen in the pure 3M ionomer. These changes in the hydrophilic domains resulted in changes in the system morphology. All systems were found to have larger more contiguous water networks at higher hydration levels. The addition of HPW perturbed this trend by producing a large number small sized domains < 15 Å at low HPW doping, and large sized domains > 15 Å at high HPW doping. SAXS experiments on the 3M ionomer also indicate that there is a shift in the ionomer peaks to lower q as λ increases, due to water uptake and swelling of the ionomer. SAXS also revealed that the addition of HPW induces significant changes in the shape features at low and large q regions (*i.e.* morphological changes). The water analysis and SAXS show that the small water domains coalesce together and form large domains with more interconnectivity between them as λ increases. Overall the shape of the water domains is best described by the inverted micelle model at low λ, and large parallel spheroidal water channels at high λ levels.

A6 Acknowledgements

This work was supported by the DOE, EERE Cooperative Agreement No. DE-FG36-07G017006 and in part by the NSF through Renewable energy MRSEC (grant DMR-0820518). We want to thank 3M for providing study material and technical support. We also want to thank the Colorado School of Mines Campus Computing, Communications, and Information

Technologies for the computational resources and the Advanced Photon Source, Argonne National Laboratory, IL. for providing beam time for the SAXS experiments.

A7 References

(1) Litster, S.; McLean, G. *Journal of Power Sources* **2004**, *130*, 61.

(2) Eikerling, M.; Kornyshev, A. A.; Spohr, E. *Adv Polym Sci* **2008**, *215*, 15.

(3) Hickner, M. A.; Ghassemi, H.; Kim, Y. S.; Einsla, B. R.; McGrath, J. E. *Chem Rev* **2004**, *104*, 4587.

(4) Song, C. S. *Catal Today* **2002**, *77*, 17.

(5) Haugen, G. M.; Meng, F. Q.; Aieta, N. V.; Horan, J. L.; Kuo, M. C.; Frey, M. H.; Hamrock, S. J.; Herring, A. M. *Electrochemical and Solid State Letters* **2007**, *10*, B51.

(6) Wu, D. S.; Paddison, S. J.; Elliott, J. A. *Energ Environ Sci* **2008**, *1*, 284.

(7) Tant, M. R.; Darst, K. P.; Lee, K. D.; Martin, C. W. *Acs Symposium Series* **1989**, *395*, 370.

(8) Whiteley, L. D.; Martin, C. R. *Journal of Physical Chemistry* **1989**, *93*, 4650.

(9) Meng, F. Q.; Aieta, N. V.; Dec, S. F.; Horan, J. L.; Williamson, D.; Frey, M. H.; Pham, P.; Turner, J. A.; Yandrasits, M. A.; Hamrock, S. J.; Herring, A. M. *Electrochim Acta* **2007**, *53*, 1372.

(10) Herring, A. M. *Polym Rev* **2006**, *46*, 245.

(11) Tazi, B.; Savadogo, O. *J New Mat Electr Sys* **2001**, *4*, 187.

(12) Malers, J. L.; Sweikart, M. A.; Horan, J. L.; Turner, J. A.; Herring, A. M. *J Power Sources* **2007**, *172*, 83.

(13) Vernon, D. R.; Meng, F. Q.; Dec, S. F.; Williamson, D. L.; Turner, J. A.; Herring, A. M. *J Power Sources* **2005**, *139*, 141.

(14) Malhotra, S.; Datta, R. *J Electrochem Soc* **1997**, *144*, L23.

(15) Ramani, V.; Kunz, H. R.; Fenton, J. M. *Electrochim Acta* **2005**, *50*, 1181.

(16) Ramani, V.; Kunz, H. R.; Fenton, J. M. *J Membrane Sci* **2005**, *266*, 110.

(17) Ramani, V.; Kunz, H. R.; Fenton, J. M. *Journal of Membrane Science* **2004**, *232*, 31.

(18) Moore, R. B.; Martin, C. R. *Macromolecules* **1988**, *21*, 1334.

(19) Hsu, W. Y.; Gierke, T. D. *Journal of Membrane Science* **1983**, *13*, 307.

(20) Fujimura, M.; Hashimoto, T.; Kawai, H. *Macromolecules* **1981**, *14*, 1309.

(21) Litt, M. H.; *Polym. Prepr.*: **1997**; Vol. 38, p 80.

(22) Schmidt-Rohr, K.; Chen, Q. *Nature Materials* **2008**, *7*, 75.

(23) Aieta, N. V.; Stanis, R. J.; Horan, J. L.; Yandrasits, M. A.; Cookson, D. J.; Ingham, B.; Toney, M. F.; Hamrock, S. J.; Herring, A. M. *Macromolecules* **2009**, *42*, 5774.

(24) Liu, Y.; Horan, J. L.; Schlichting, G. J.; Caire, B. R.; Liberatore, M. W.; Hamrock, S. J.; Haugen, G. M.; Yandrasits, M. A.; Seifert, S.; Herring, A. M. *Macromolecules* **2012**, *45*, 7495.

(25) Gebel, G. *Polymer* **2000**, *41*, 5829.

(26) Elliott, J. A.; Wu, D. S.; Paddison, S. J.; Moore, R. B. *Soft Matter* **2011**, *7*, 6820.

(27) Gebel, G.; Lambard, J. *Macromolecules* **1997**, *30*, 7914.

(28) Moore, R. B.; Martin, C. R. *Macromolecules* **1989**, *22*, 3594.

(29) Wu, D. S.; Paddison, S. J.; Elliott, J. A.; Hamrock, S. J. *Langmuir* **2010**, *26*, 14308.

(30) Paddison, S. J.; Elliott, J. A. *Journal of Physical Chemistry A* **2005**, *109*, 7583.

(31) Sunda, A. P.; Venkatnathan, A. *J Mater Chem A* **2013**, *1*, 557.

(32) Devanathan, R.; Dupuis, M. *Phys Chem Chem Phys* **2012**, *14*, 11281.

(33) Tse, Y. L. S.; Herring, A. M.; Kim, K.; Voth, G. A. *J Phys Chem C* **2013**, *117*, 8079.

(34) Jang, S. S.; Molinero, V.; Cagin, T.; Goddard, W. A. *Journal of Physical Chemistry B* **2004**, *108*, 3149.

(35) Komarov, P. V.; Veselov, I. N.; Chu, P. P.; Khalatur, P. G.; Khokhlov, A. R. *Chem Phys Lett* **2010**, *487*, 291.

(36) Liu, Y.; Sambasivarao, S. V.; Horan, J. L.; Yang, Y.; Maupin, C. M.; Herring, A. M. *The Journal of Physical Chemistry C* **2013**.

(37) Mayo, S. L.; Olafson, B. D.; Goddard, W. A. *Journal of Physical Chemistry* **1990**, *94*, 8897.

(38) Brodbeck, R.; Tonsing, T.; Andrae, D.; Volkmer, D. *Journal of Physical Chemistry B* **2008**, *112*, 5153.

(39) Levitt, M.; Hirshberg, M.; Sharon, R.; Laidig, K. E.; Daggett, V. *J Phys Chem B* **1997**, *101*, 5051.

(40) Knox, C. K.; Voth, G. A. *Journal of Physical Chemistry B* **2010**, *114*, 3205.

(41) Plimpton, S. *J Comput Phys* **1995**, *117*, 1.

(42) Schneider, C. A.; Rasband, W. S.; Eliceiri, K. W. *Nat Methods* **2012**, *9*, 671.

(43) Abràmoff, M. D.; Magalhães, P. J.; Ram, S. J. *Biophotonics international* **2004**, *11*, 36.

(44) Rasband, W. S.

(45) Humphrey, W.; Dalke, A.; Shulten, K. *J. Molec. Graphics* **1996**, *14*, 33.

(46) Murata, K.; Mitsuoka, K.; Hirai, T.; Walz, T.; Agre, P.; Heymann, J. B.; Engel, A.; Fujiyoshi, Y. *Nature* **2000**, *407*, 599.

(47) Brandell, D.; Karo, J.; Liivat, A.; Thomas, J. O. *J Mol Model* **2007**, *13*, 1039.

(48) Gierke, T. *J. Electrochem. Soc* **1977**, *124*, 319c.

APPENDIX B SYNTHESIS AND CHARACTERIZATION OF RANDOM AND BLOCK COPOLYAMIDES

B1 Synthesis

Both block and random copolyamides with vaious IECs were synthesized. The synthesis routes and procedures are provided below.

B1.1 Materials and Purification

M-phenylene diamine (MPDA), 5-sulfoisophthalic acid sodium salt (SIPA), isophthalic acid (IPA), N-methyl-2-pyrrolidone (NMP), dimethyl sulfoxide (DMSO) and triphenylphosphite (TPP) were purchased from Aldrich. Lithium chloride was purchased from Fisher, and pyridine (Py) was purchased from Mallinckrodt. MPDA was purified by distillation under a vacuum system followed by recrystallization from diethyl ether. SIPA and IPA were purified by recrystallization from methanol and ethanol. NMP and Py were distilled from calcium hydride before use. TPP was first dissolved in diethyl ether to form a mixture solution, and then the solution was washed by 5% NaOH solution and saturated NaCl solution twice each; $MgCl_2$ was used to remove the extra water from solution; and the pure TPP was obtained by distilling off the diethyl ether.

B1.2 Synthesis of Random Copolymer Sulfonated Poly (m-Phenylene Isophthalamide) [MPDA-SIPA$_x$ (Na)]

10.00 mmol MPDA, different ratios of SIPA and IPA (10.00 mmol in total) with 31.45 mmol lithium chloride were put into a 125 ml single neck round-bottom flask, which was then

sealed by a septum before purging with nitrogen gas for 30 minutes. 22 mmol TPP, 36.6 ml NMP and 13.4 ml Py were then added to the flask through a syringe. The flask was then put into a 105°C oil bath and stirred for 24 hours. After the reaction, the residue was precipitated in 600 ml methanol. The precipitate was then collected through filtration and vacuum dried, followed by re-dissolving it in DMSO and re-precipitating it in methanol. The precipitate was collected through filtration and dried under vacuum at 80°C overnight. The yield is above 99%. The synthetic route for the random copolyamide is shown in Scheme B1.

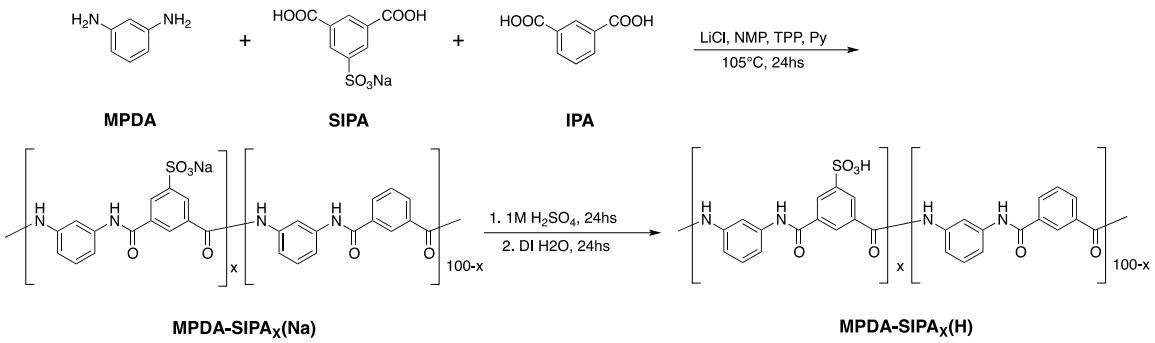

Scheme B1 Synthetic route of random sulfonated aromatic polyamides MPDA-SIPAx.

B1.3 Synthesis of Block Copolymer [(MPDA-SIPA$_x$)-b-(MPDA-IPA)(Na)]

6.76 mmol MPDA, 5.38 mmol SIPA and 19.09 mmol LiCl were put into a 125 ml single neck round-bottom flask, sealed with a septum and purged with nitrogen gas for 30 minutes. 13.36 mmol TPP, 22.3 ml NMP and 8.1 ml Py were added to the flask through a syringe. The flask was stirred at 105 °C for 24 hours. 6.69 mmol MPDA, 8.07 mmol IPA, and 23.23 mmol LiCl were put into another single neck round-bottom flask sealed by septum, and purged with nitrogen gas for 30 minutes. 16.41 mmol TPP, 27.0 mL NMP and 9.9 ml Py were added to this flask through a syringe. After making sure the solids were all dissolved, the solution was

transferred to another flask with a cannula. The mixture was stirred at 105°C for 24 hours, after which the flask was cooled down to room temperature, and the polymer was precipitated by pouring it into 750 ml methanol. The precipitate was collected through filtration and then dried followed by re-dissolving it in DMSO and re-precipitating it in methanol. The precipitate was filtered and dried under vacuum at 80°C overnight. The yield is above 96%. The synthetic route of block copolyamide is shown in scheme B2.

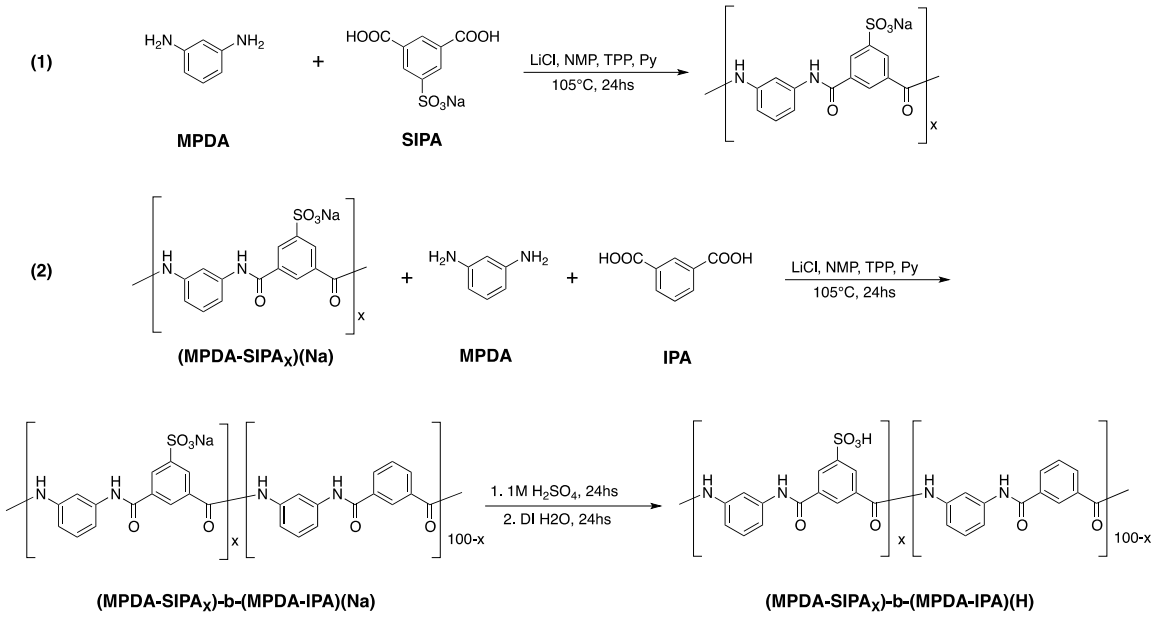

Scheme B2 Synthetic route of block sulfonated aromatic polyamides (MPDA-SIPAx)-b-(MPDA-IPA).

B1.4 Membrane Preparation of Sulfonated Aromatic Polyamides [MPDA-SIPA$_x$(H)]

0.1 g sodium-sulfonated polyamide was dissolved in 2 ml DMSO, and the solution was directly casted onto a clean glass substrate. The membrane was formed by removing DMSO using a hot plate at 80°C for 24 hours. The membrane was converted to its sulfonic acid form by

immersing it in 0.01M H_2SO_4 for 24 hours. The membrane was soaked in deionized water for 8 hours to remove excess H_2SO_4, with the water changed every 2 hours.

B2 IEC Measurement

The IEC was experimentally determined by back titration of the remaining NaOH solution after ion exchanged with the film using HCl solution and calculated based on the following equation:

$$\text{IEC} = \frac{V_{NaOH} * c_{NaOH} - V_{HCl} * c_{HCl}}{W_{dry}}$$

Where V_{HCl} and c_{HCl} are the volume and concentration of the standardized HCl solution; V_{NaOH} and c_{NaOH} are the volume and concentration of standardized NaOH solution; W_{dry} represents the weight of the dry membrane. The measured IECs for random copolyamides are shown in table B1.

Table B1 IEC of random copolyamides MPDA-SIPA$_x$.

DS of MPDA-SIPA$_X$	IEC (mequiv/g)
MPDA-SIPA$_{40}$ (H)	1.44
MPDA-SIPA$_{45}$ (H)	1.60
MPDA-SIPA$_{50}$ (H)	1.75
MPDA-SIPA$_{70}$ (H)	2.35
MPDA-SIPA$_{80}$ (H)	2.61

B3 ^{1}H NMR Study

The ^{1}H NMR spectra of sodium sulfonate form of random and block copolymers were

measured by using a JEOL ECA-500 FT-NMR at room temperature. Dimethyl sulfoxide-d6 was used as the solvent and chemical shifts (δ) are reported in ppm.

Figure B3 shows the ^{1}H NMR spectra of random and block copolymer at DS of 40 mol%; these two polymers have the same shift for all peaks, and the integration of the amide peaks matches the feed ratio of monomers, which proves the feasibility of a controllable synthesis of the block copolymer.

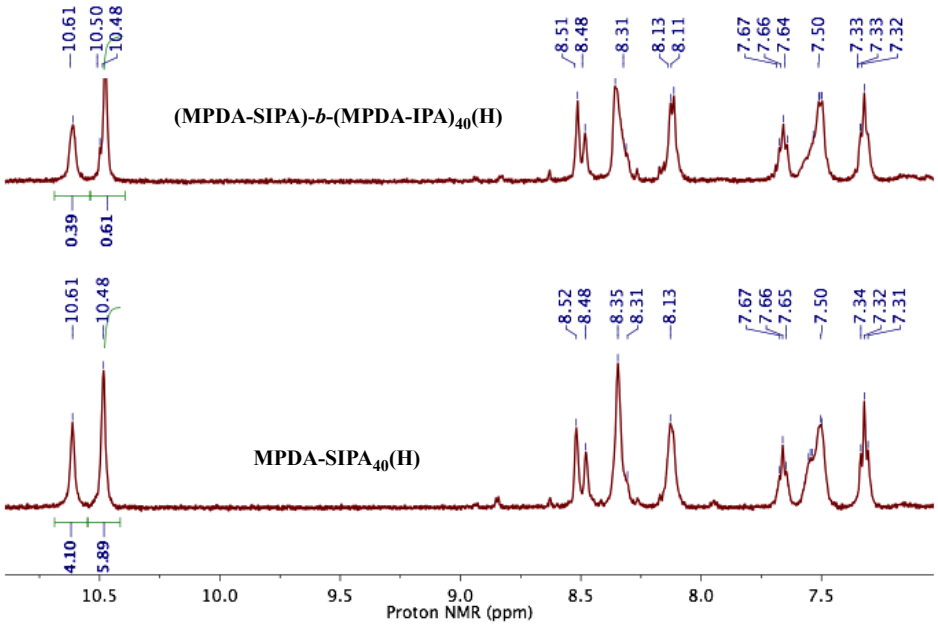

Figure B1 ^{1}H NMR Spectra of Random and Block Copolymers at DS=40mol%.